**Title**

Development of Micron-Scale Hydrogel Materials for the Treatment and Management of Heart Failure

**Permalink**

https://escholarship.org/uc/item/7011w73j

**Author**

Le, Long Van

**Publication Date**

2018

Peer reviewed|Thesis/dissertation

Development of Micron-Scale Hydrogel Materials for the
Treatment and Management of Heart Failure

by

Long Van Le

DISSERTATION

Submitted in partial satisfaction of the requirements for the degree of

DOCTOR OF PHILOSOPHY

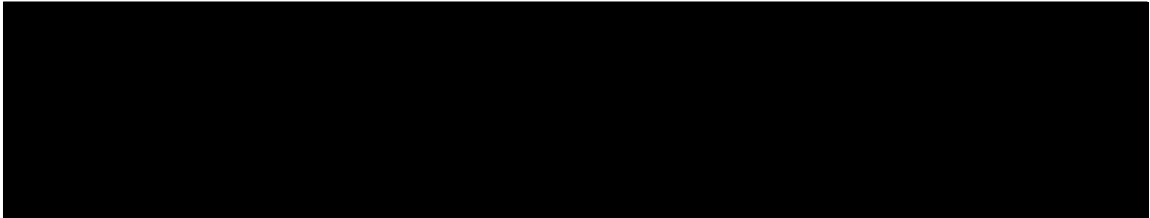in

Bioengineering

in the

GRADUATE DIVISION

of the

UNIVERSITY OF CALIFORNIA, SAN FRANCISCO

AND

UNIVERSITY OF CALIFORNIA, BERKELEY

Approved:

███████████████████████████████████████████

......................................................................................................................

......................................................................................................................

Committee in Charge

**Dedication and Acknowledgments**

Elements of this dissertation have been published elsewhere or are in submission or preparation for publication in a peer-reviewed journal. Chapters 2 and 3 include portions of work published by Le LV, Mohindra P, et al. in Biomaterials 169:11-21 (2018) under the title "Injectable hyaluronic acid based microrods provide local micromechanical and biochemical cues to attenuate cardiac fibrosis after myocardial infarction." Chapters 4 and 5 include portions of work that are in preparation for submission to a peer-reviewed journal for publication. In particular, the magnetic micromagnet work in Chapter 4 is currently in submission for publication in a peer-reviewed journal. The HepIII microrod work was accepted to the 2018 Biomedical Engineering Society Conference in the form of an abstract and research talk.

I would first like to acknowledge my research advisor, Dr. Tejal Desai, for her continued support and guidance throughout my graduate education. She gave me the freedom to explore, no matter how ambitious the idea or experiment, and was always there to help me find the silver lining in my data when I thought I had failed. I am very blessed to have had the opportunity to work in her lab and to grow as a researcher under her mentorship. I would also like to thank my qualifying exam committee, including Drs. Tamara Alliston, Zev Gartner, Matt Springer and Phil Messersmith for their support and expertise as I was preparing my research proposal. Additionally, I would like to thank my dissertation committee, Drs. Sanjay Kumar, Matt Springer, and my research advisor Tejal Desai for their continued guidance on my thesis work.

Throughout graduate school, I have had the opportunity to work on a number of collaborative projects that were instrumental in shaping my graduate thesis work. These works would not have been possible without the critical contributions from my brilliant collaborators. I would like to thank the members of Dr. Randall Lee's lab, including Dr. Qizhi Fang and Richard

reassuring me that I would survive and that I would succeed. Their confidence and trust in me during these past 6 years drove me to strive for excellence in research and this dissertation in its entirety would not have been possible without them.

# Development of Micron-Scale Hydrogel Materials for the Treatment and Management of Heart Failure

*Long Van Le*

## Abstract

Ischemic heart disease is the leading cause of death worldwide, accounting for over 16% of deaths each year. While we have succeeded in lowering mortality rates through improved care in the acute setting, treating the chronic morbidities that affect the surviving patient population remains a significant challenge. This has led to rising healthcare costs and increased mortality due to chronic heart failure. In this work, we describe novel micro- and nano-fabricated technologies to manage and treat heart failure. First, we describe the development and application of hyaluronic acid-based polymeric microstructures, termed "microrods", to attenuate the development of scar tissue following a myocardial infarction and prevent pathological myocardial remodeling. *In vitro* studies demonstrate the influence of these HA microrods on fibroblasts and cardiomyocyte phenotype, down-regulating key fibrotic indicators. When injected into the infarct zone of adult Sprague-Dawley rats after induction of a myocardial infarction, HA microrods improved cardiac function and preserved the structure of the myocardium as shown by echocardiography and histology, respectively. We then explore novel functionalization of these microrod materials through surface conjugation, drug loading or nanoparticle loading to confer additional therapeutic mechanisms. Lastly, we demonstrate the synthesis and optimization of optical nanoparticle sensors to detect oxygen, glucose and lactate. These sensors are incorporated into tissue-integrating hydrogel scaffolds and can be implanted

subcutaneously for continuous sensing to track the progression of heart disease. In summary, we

developed several innovative therapeutic strategies utilizing micro- and nanoengineered

materials that can be used for comprehensive management and treatment of heart failure.

**Table of Contents**

## List of Figures

**List of Tables**

## Chapter 1 – Introduction

### 1.1 Myocardial infarction and the progression of cardiac fibrosis

Within the past few decades, advancements in biomedical research and improvements in emergency response systems have reduced mortality rates in the acute setting of myocardial infarction (MI)[1]. By comparison, the resulting chronic complications of heart failure that develop in the wake of tissue trauma remain a substantial challenge[2–5]. Here, we review the pathophysiology of myocardial infarction and heart failure, as well as current strategies to mitigate this poor prognosis.

A myocardial infarction is an acute medical emergency in which the heart is cut off from blood flow, resulting in severe cardiac ischemia. The lack of nutrient and oxygen supply to the heart results in substantial cell necrosis in the affected area that initiates an inflammatory cascade by release of intracellular signaling components[6,7]. During this inflammatory response, which typically occurs within 1-5 days of MI, a range of immune cells, including macrophages, monocytes and neutrophils are recruited to the injury site, where they actively produce cytokines and proteolytic enzymes[8–10]. This leads to degradation of the cardiac extracellular matrix (ECM) and subsequent release of latent signaling factors.

Cardiac fibroblasts, previously thought to be a senescent cell type, responds to these events and transform into a more active myofibroblast phenotype, producing high amounts of matrix proteins, including collagen I and III, to restore the mechanical properties of the myocardium[11–14]. However, unlike activated fibroblasts present in other areas of the body, cardiac myofibroblasts do not readily revert back to their inactive state, resulting in continuous deposition of scar tissue[15–17]. This progressive tissue stiffening leads to additional stress on the heart and reduces cardiac output. In response, several compensatory mechanisms are activated in

attempts to increase blood output and meet the metabolic demands of the body, which can be categorized into two primary pathways. First, activation of the sympathetic system attempts to increase cardiac output by increasing heart rate and myocardial contractility[4,18]. Second, the renin-angiotensin-aldosterone system (RAAS) is activated to induce vasoconstriction and retention of sodium and water to increase blood volume[4,19]. While able to increase cardiovascular output in the short-term, prolonged activation of these compensatory mechanisms is counterproductive and places excessive strain on the heart. These myocardial stresses induce further pathological tissue remodeling and exacerbates the progression towards heart failure.

**1.2 Acellular therapies for the treatment and management of heart failure**

Several therapeutic interventions have been used to mitigate the progression of chronic heart failure, including pharmacological agents, cardiac patches and bulk polymer injections. Pharmacological agents, such as angiotensin converting enzyme (ACE) inhibitor and beta-adrenergic blocking agents (beta blockers) act on the sympathetic and RAAS systems to reduce the work load on the heart either directly or by vasodilation to reduce blood pressure[3,19–25]. This reduction of mechanical stress limits left ventricular wall thinning and infarct expansion, slowing down the progression of heart failure.

Ventricular restraint devices that entirely enclose either the left ventricle or both ventricles have also been studied for the treatment of heart failure[26–28]. These restraints target infarct expansion by directly reducing myocardial wall stress throughout the ventricle and thereby limiting ECM remodeling and scar tissue formation both within the infarct and throughout the non-infarcted myocardium. The most extensively studied of these devices are the Acorn CorCap Cardiac Support Device and the Paracor HeartNet, both which have undergone

clinical trial testing[28–37]. The Acorn CorCap device is a flexible, polyethylene-terephthalate mesh that is wrapped over both ventricles to limit diastolic volume to prevent LV expansion and increase cardiac output. In animal studies, the CorCap device was shown to not only preserve, but also reverse the changes in cardiac structure and function due to aberrant remodeling[38,39]. The Paracor HeartNet limits LV dilatation in a similar fashion, but is able to exert force onto both ventricles throughout the cardiac cycle due to use of an elastic Nitinol mesh material[37,40].

Despite exciting results in preclinical animal studies, the therapeutic efficacy of these devices was less clear in clinical trials. In a randomized study of 300 patients, the CorCap device demonstrated significant reduction in LV end diastolic volume (LVEDV) and LV end systolic volume (LVESV), but no differences in LV ejection fraction (LVEF) or survival advantage at 12 months compared to controls[29–32]. Similarly, the Paracor HeartNet device showed significant improvements in LV end diastolic dimension (LVEDD), LVEDV and LVESV in a nonrandomized trial of 21 patients, but failed to show improvements in survival or mVO2 in a larger randomized study of 217 patients, casting doubt onto the efficacy of these restraint devices[34,37]. Since then, there have been no updates on the investigation of these materials for the treatment of heart failure. It is also important to note that the application of these materials is limited to a subset of patients with HF. The progression of HF must be severe enough to necessitate surgical procedures, while not advanced enough such that the restraint devices are unable to provide any functional benefits.

These limitations are partially addressed by the use of injectable materials, namely polymeric hydrogels, to increase LV wall thickness and moderate mechanical load to reduce wall stress and pathological LV remodeling. These materials can be injected into the myocardium via catheter injection through less invasive procedures, eliminating the need for surgical operations.

A host of synthetic and natural materials have been studied and extensively reviewed[41–45]. Synthetic materials, such as poly(N-isopropylacrylamide) and poly(ethylene glycol), offer the benefit of being well characterized and easily engineered to impart desired functionalities, such as sheer-thinning properties, controlled degradation, or temperature and pH sensitivity. By comparison, natural materials exhibit greater biocompatibility and degradation kinetics and are often able to recapitulate the biophysical and chemical properties of the native ECM. Hyaluronic acid, for example, has been widely used for this application because it is bioresorbable and has critical roles in wound healing[46–55]. Recently, there has been significant interest in using decellularized ECM for tissue engineering applications. These materials preserve binding motifs and signaling components present in healthy tissue to recruit progenitor cells or improve cell survival and promote endogenous repair mechanisms[56–59]. While many of these materials, both synthetic and natural, have shown great promise in preclinical studies, only a few have proceeded to clinical trials thus far.

The PRESERVATION-1 trial investigated the effectiveness of an alginate hydrogel (IK-5001) for prevention of ventricular remodeling in 303 patients[60–62]. Interestingly, there were no significant improvements in cardiac function compared to control groups, in contrast to the therapeutic benefits observed in a preclinical porcine ischemia/reperfusion model. Another alginate-based material, Algisyl-LVR, was also investigated in clinical trials[63–65]. This material consists of two components: a $Na^+$ alginate solution and a $Ca^{2+}$ alginate solution that are mixed immediately before use. This hydrogel is delivered the alginate hydrogel via 10-15 injections during a coronary artery bypass grafting and showed improvements in LVEDV, LVESV and LVEF in all patients in a preliminary study[63,64]. A follow-up study, AUGMENT-HF, consisting of 78 patients with advanced heart failure investigated the therapeutic benefits of Algisyl-LVR

injections compared to standard medical therapy alone. After 12 month follow-up, mean peak VO$_2$ and mean 6 minute walk distance increased in patients injected with Algisyl-LVR while decreases in these metrics was observed in control patients[65,66]. Additionally, there were improvements in EF shortly after injection, but these improvements were not sustained in the long-term and did not significantly differ from the control treatment group.

**1.3 Cell-based therapies for cardiac tissue regeneration**

In recent years, development of stem cell-based therapies has been at the forefront of preclinical and clinical research in cardiac regeneration and heart failure[67–71]. Initial studies focused on promoting cardiac repair by delivery of stem or progenitor cell populations into the infarct area, which would then differentiate into functional cardiomyocytes. A large number of clinical trials have since been conducted to study the efficacy of a wide range of cell types, including cardiac stem cells, mesenchymal stem cells and iPSCs, but have failed to conclusively demonstrate long-term clinical efficacy[71–74]. This can be attributed to the heterogeneity in study design, such as variation in cell types and origin, dosage, delivery mechanism and patient disease state. Additionally, there is incomplete understanding of the mechanism by which transplanted stem cells contribute to cardiac regeneration, further obstructing the development of a clinically viable stem cell-based therapy. For example, one hypothesis is that stem cells promote cardiac regeneration by release of paracrine factors to stimulate proliferation and differentiation of endogenous cell types, leading many researchers to focus on designing cell-free approaches that act through a similar mode of action[75–81]. It is therefore crucial for investigators to backtrack and precisely standardize study design prior to conducting additional clinical trials, which have so far failed to define a clear and effective clinical approach.

Cardiac patches that incorporate the mechanical elements of an LV restraint device with the regenerative capacity of stem cells have been investigated for replacement of diseased or damaged tissue following myocardial injury[26,82]. Typically, these patches involve the use of a biomaterial scaffold for enhanced cell delivery to infarct area, although their utilization as an acellular therapy has also recently been observed. Scaffolds have been fabricated out of a variety of inert and bioactive materials, such as silk, poly-L-lactic acid, or collage, and impregnated with cells before being sutured onto the infarct area[82]. Recently, Stoppel *et al* developed cardiac ECM-silk graft materials that combine the native signaling properties of cardiac ECM with the tunable mechanical properties of silk to enhance cell infiltration, viability, and functional activity [83]. A major advantage of pre-formed scaffolds is that their structure and geometry can be precisely designed via microfabrication, soft lithography, and electrospinning approaches to support cell infiltration and engraftment. Through this, researchers have been able to grow cardiomyocytes in aligned layers within the patch for synchronous beating post-implant, a key requirement that is often unmet when injecting cells alone. One enduring challenge of this approach, however, is the inability to generate patches with adequate thickness due to diffusion limitations – thick scaffolds must integrate with the host tissue and rapidly vascularize to deliver adequate amounts of oxygen and nutrients to the implanted cells. As very metabolically demanding cells, ischemia for even 30 minutes can result in significant cell death and reduction in graft efficacy[84]. Acellular patches that deliver pharmacological or biological agents to stimulate paracrine signaling pathways and harness intrinsic healing mechanisms may provide a simpler alternative for tissue repair.

**1.4 Microtopographical approaches to modulate cell behavior for cardiac repair**

Cells in the heart are continuously subjected to mechanical forces and are equipped with an abundance of cellular machinery to detect and respond to these forces[85–87]. While this has been recognized since the early 1980s, mechanical stimuli have only recently been utilized for tissue engineering applications. For example, Gwak *et al* demonstrated that cyclic mechanical stretch can influence differentiation and activity of cardiomyocytes *in vitro*[88]. This strategy has been widely used to generate sheets of cardiomyocytes for the previously mentioned cardiac patches. There is therefore great potential in utilizing local mechanical stimuli to locally reprogram native cells in the infarcted myocardium and harness intrinsic regenerative pathways for cardiac regeneration.

As described in this chapter, there is significant degradation of the cardiac extracellular matrix following a myocardial infarction, resulting in altered mechanical stiffness and disruption of cell-cell and cell-ECM interactions[12,89]. These dramatic changes are thought to induce phenotypic changes of cardiomyocytes and cardiac fibroblasts that lead to overexpression of ECM proteins and formation of a stiff myocardial scar. To address this, microengineered materials have been developed to attenuate the fibrotic response by providing anchors to cells in this weakened 3D microenvironment and decrease stress-induced mechanotransductive pathways. Boateng *et al* first observed that when grown on polyethylene glycol dimethacrylate (PEGDMA) micropegs, cardiac fibroblasts form intimate attachments to nearby structures and exhibit reduced proliferation[90]. Similarly, Allen *et al* used a lamination approach to produce polypropylene microfibers of varying aspect ratio and demonstrated reduced fibrotic encapsulation when implanted in mice[91]. For therapeutic applications in cardiovascular repair, adaptation of these technologies towards an injectable therapy is required. Ayala *et al* utilized

free PEGDMA microstructures in 3D culture to attenuate fibroblast proliferation and inhibit expression of key myofibroblast markers implicated in cardiac fibrosis[92]. These PEGDMA microstructures are reproducibly fabricated on silicon wafers via a scalable photolithography approach and can be easily removed from the wafer and stored until use. PEGDMA microrod treatment mitigated loss of cardiac function in a rat model of MI[93]. These studies collectively highlight the potential of microtopography and mechanotransduction for the treatment of cardiac fibrosis and heart failure. There are, however, several limitations that must be addressed before this strategy can be used clinically. Firstly, biocompatibility and degradation of these materials have yet to be rigorously determined and may present complications for long-term use. Second, optimal dosing has not been determined, although higher doses of microstructures have been correlated with improved cardiac function in a rat model of MI. Finally, this microstructural approach has only been tested with an acute MI model for attenuation of fibrosis and it is unclear whether these beneficial effects will also be observed in a chronic model of heart failure. Despite these concerns, this therapeutic approach is still in its infancy and there are exciting opportunities for optimization including, but not limited to, investigation of alternative synthetic and natural materials, codelivery with pharmacological or cellular therapeutics, and development of a precise and reliable delivery method.

## 1.5 Towards development of a comprehensive treatment for heart failure

The development of a comprehensive treatment of heart failure remains an elusive challenge. An ideal treatment strategy would involve attenuation of cardiac fibrosis and LV remodeling, as well as regeneration of cardiac tissue to restore functional output. The ability to monitor disease progression or functional improvements is also critical, as it would enable

patients and healthcare providers to quickly respond to adverse developments in disease state. Finally, all of these interventions should be easily administered by noninvasive routes and be applicable to a wide range of patients with variable disease states.

Here, we describe the use of microengineered hydrogel materials to address these challenges. In chapter 2, we develop and fully characterize a hyaluronic acid-based microrod material for manipulation of fibroblast and cardiomyocyte behavior *in vitro*. In chapter 3, investigate the application of these materials for the treatment of cardiac fibrosis using fibroblast cell lines and a rat model of ischemia/reperfusion, respectively. Chapter 4 expands on the versatility of these microscale materials by incorporation of additional components to impart additional functionalities, such as remote manipulation, release of therapeutics and surface functionalization. Lastly, the development of hydrogel scaffold-nanosensor composite materials for the continuous detection of blood metabolites is described in chapter 5.

## Chapter 2 – Development of Hyaluronic Acid Microstructures for Micromechanical Interaction with Cardiac Fibroblasts and Myocytes

### 2.1. Introduction

Repairing cardiac tissue after myocardial infarction (MI) is one of the most challenging goals in tissue engineering. Following ischemic injury, significant matrix remodeling and the formation of avascular scar tissue significantly impairs cell engraftment and survival in the damaged myocardium[5,7,11,12]. This aberrant response limits the efficacy of endogenous repair mechanisms and cell replacement therapies, necessitating the development of strategies that reduce pathological scarring to create a suitable microenvironment for healthy tissue regeneration. Such advancements would enhance our clinical capabilities in treating the chronic complications of MI in a growing patient population progressing towards heart failure.

Within the past several decades, mechanical forces have gained significant appreciation as a potent mechanism for altering cellular activity[94–100]. Mechanically sensitive cells, such as fibroblasts, cardiomyocytes and endothelial cells, are able to detect environmental forces through ion channels, integrins and other surface receptors[85,86,97,101–103]. These forces are transduced into intracellular signals that elicit transcriptional changes leading to altered cellular phenotype.  Our lab has previously investigated the use of polymeric microrods and microfibers to mitigate the fibrotic response through these biophysical pathways[91–93]. These features locally alter the microenvironment by providing anchors for fibroblast attachment, resulting in significant changes in proliferation, myofibroblast differentiation and ECM protein expression. While promising, the use of bioinert, nondegradable materials for presents several complications for long-term use in the clinical setting. There is also great potential in using bioactive materials to deliver biochemical cues in addition to mechanical stimuli for additional therapeutic benefits.

Hyaluronic acid (HA) is a naturally derived polysaccharide that can be adapted for this microtopography-based approach to cardiac tissue regeneration. It is widely distributed in the body at high molecular weights and is degraded into small fragments by hyaluronidases and oxidative hydrolysis[46,47,104,105]. These two forms of HA have distinct effects on a range of biological processes, including angiogenesis and inflammation[46–49,104–108]. While HMWHA has anti-angiogenic and anti-inflammatory effects, short fragments stimulate proliferation and migration to promote angiogenesis. Accordingly, many HA-based scaffolds have been developed within the past decade to exploit these properties for wound healing applications[52–55].

In this chapter, we present the development of hyaluronic acid-based microrods for the treatment of chronic cardiac fibrosis. These HA-based microrods can be reproducibly fabricated using standard photolithographic techniques and are demonstrated to be biodegradable, promote cell growth and attenuate the myofibroblast phenotype.


## 2.2 Materials and Methods

### 2.2.1 Materials

Sodium hyaluronate (100kDa) was purchased from Lifecore Biomedical (Chaska, MN). Glycidyl methacrylate, triethylamine, 2-hydroxy-4′-(2-hydroxyethoxy)-2-methylpropiophenone (HMPP), Hyaluronidase (type I-S) from bovine testes, sodium tetraborate decahydrate, sulfuric acid, and carbazole were purchased from Sigma-Aldrich (St. Louis, MO). 4'-(aminomethyl)fluorescein and sulfo-SANPAH were purchased from ThermoFisher Scientific (Waltham, MA). Collagenase type II was purchased from Worthington Biochemical (Lakewood, NJ). Acrylamide, n,n'-methylenebisacrylamide (bis) solution, ammonium persulfate, and tetraethylmethylenediamine were purchased from Bio-Rad (Hercules, CA).

*2.2.2 Synthesis of hyaluronic acid methacrylate*

Hyaluronic acid methacrylate was synthesized based on a method published by Bencherif et al[109]. Briefly, sodium hyaluronate (100 kDa) was dissolved in a solution of 1:1 deionized water:dimethylformamide at 3.75 mg/mL. A 100-fold molar excess of glycidyl methacrylate and 35-fold molar excess of triethylamine was then added. The reaction was allowed to proceed for 24 hours at room temperature and away from light. Hyaluronic acid and hyaluronic acid methacrylate were recovered by precipitation in an excess of isopropanol. The precipitate was then pelleted by centrifugation at 700 x g for 5 minutes and dissolved in water. The resulting solution was dialyzed against water for 48 hours with three changes and lyophilized for 3 days at -40 °C and 65 mtorr to yield a dry powder. Degree of methacrylation was determined by $^1$H-NMR in $D_2O$ using a Bruker Avance III HD 400 NMR.

*2.2.3 Characterization of hyaluronic acid methacrylate stiffness*

Crosslinked hyaluronic acid methacrylate hydrogels were fabricated in a range of concentration for mechanical testing. Briefly, HMPP was dissolved in water at a 0.5% w/v concentration. The resulting solution was used to dissolve HAMA at 25, 50, 75 and 100 mg/mL. Once fully dissolved, the solution was centrifuged at max speed for 5 minutes to remove impurities. The precursor solution was then injected into a mold comprising of a 0.8 mm Teflon spacer sandwiched between two glass slides and exposed to 365 nm UV light for 5 minutes. The resulting crosslinked hydrogel was retrieved and allowed to swell further in water. The stiffness of these hydrogels was determined by atomic force microscopy using a MFP3D-BIO inverted optical AFM (Asylum Research) mounted on a Nikon TE2000-U inverted fluorescent microscope. For these measurements, a gold deposited silicon nitride cantilever (k = 0.09 N/m)

with a pyramidal tip was used. 10 measurements were made for each hydrogel at 3 different locations. The average of these 30 measurements was used for each replicate. Cantilevers were calibrated using a thermal oscillation method prior to each session.

*2.2.4 HA microrod fabrication*

Solutions of hyaluronic acid methacrylate were prepared as described above. A 15 µm thick layer of this solution was deposited onto a piranha cleaned silicon wafer and exposed through a photomask to a 365 nm UV light source using a Karl Suss Mask Aligner to crosslink the hyaluronic acid methacrylate in rod shapes (15 µm × 100 µm). The microrods were then gently scraped off the surface of the wafer using a cell scraper and collected into water, where uncrosslinked regions of hyaluronic acid methacrylate would fully dissolve. The microrods were passed through a 150 µm mesh filter to remove large particles and washed thoroughly by centrifugation. The microrods are sterilized with 70% ethanol and resuspended in saline or cell culture medium prior to use. Microrods were imaged using differential interference contrast (DIC). To visualize 3D geometry, HA microrods were labeled with 4'-(aminomethyl)fluorescein (Thermofisher, Waltham, MA) through EDC/NHS coupling and imaged using confocal microscopy.

*2.2.5 Degradation of crosslinked hyaluronic acid methacrylate*

Crosslinked hyaluronic acid methacrylate hydrogels were degraded at 37 °C in 100, 10 or 0 U/mL hyaluronidase in phosphate buffered saline (PBS). The supernatant for each hydrogel was collected and replaced with fresh hyaluronidase solution every 48 hours. For each time point, the amount of uronic acid was measured using a carbazole-based reaction[110]. Briefly, 200

μl of 24 mM sodium tetraborate decahydrate dissolved in concentrated sulfuric acid was added to 50 ul of each sample and heated to 100 °C for 10 minutes. 50 μl of 0.125% carbazole in absolute ethanol was then added to each sample and heated to 100 °C for 15 minutes. 200 ul of each solution was analyzed in a plate reader at 530 nm. Known concentrations of 100 kDa HA were used as a standard. Following the last time point, all remaining hydrogels were placed in concentrated sulfuric acid and assayed to determine the total amount of HA remaining.

For HA microrods, degradation was conducted by incubating the microrods in 100 U/mL, 10 U/mL and 0 U/mL hyaluronidase at 37 °C. The microrods were pelleted by centrifugation at maximum speed for 5 minutes. The supernatant was collected and replaced with fresh buffer solution. Uronic acid was quantified as described above.

### 2.2.6 Neonatal rat ventricular fibroblast and myocyte culture

Primary heart cultures were obtained from neonatal rats according to Institutional and National Institutes of Health guidelines. Hearts were removed from 1- to 2-day-old Sprague-Dawley rats and cells isolated using collagenase type II, per previously established protocol[111]. Fibroblasts, which had been separated from myocytes during isolation, were cultured an additional 2 days before detaching cells with trypsin and seeding in new dishes for experiments.

### 2.2.7 Interaction of cardiac fibroblasts and myocytes with HA microrods

Fibroblasts and myocytes were cultured with HA microrods on a 10kPa polyacrylamide substrate to visualize interactions under physiological stiffness. Briefly, 40% unpolymerized acrylamide and 2% bis solution were diluted in water at final concentrations of 5% acrylamide and 0.3% Bis. Ammonium persulfate and tetraethylmethylenediamine were added to initiate

polymerization. A total of 10 uL of the pre-polymer solution was then added to glass bottom

dishes and covered with a circular coverslip. The solution was allowed to polymerize for 10

minutes, then coverslips were gently removed, leaving behind a flat, circular substrate. Dishes

were washed three times in DI water for 10 min at a time to remove unpolymerized acrylamide.

These surfaces were then treated twice by drying sulfo-SANPAH in HEPES (50 mM, pH 8.5) on

each surface for 60 minutes at 57 °C. A UV exposure box with a 365 nm bulb was used to link

the sulfo-SANPAH to the substrate. The substrate was then washed 3x and then coated with

HEPES containing fibronectin (10 µg/mL) at 37 °C for at least 2 hours before UV-sterilizing in

water for 20 minutes. The water was then aspirated under sterile conditions and HA microrods

were added. Fibroblasts alone, myocytes alone, or a combination of both fibroblasts and

myocytes were plated at desired density.

*2.2.8 Image analysis*

A Zeiss LSM 710 confocal microscope at the University of Illinois at Chicago was used

for fluorescence imaging of myocyte and fibroblast interactions with HA microrods after 24

hours *in vitro*. Single-plane and Z-stack images were obtained using a 63x Zeiss objective. Cells

were fixed in 10% formalin and probed for focal adhesions using a primary antibody for paxillin

[ab32084] (Abcam, Cambridge, MA) at 1:250 dilution. The antibody was incubated overnight,

then counterstained with secondary antibody (A21207, Thermofisher, Waltham, MA),

rhodamine phalloidin (R415, Thermofisher, Waltham, MA), and DAPI (H-1200, Vector

Laboratories, Burlingame, CA). Visualization of fibronectin bound to microrods was conducted

by incubating HA microrods for 2 hours at 37 °C in 10 µg/mL of fibronectin in PBS, or in PBS

alone as a control. Fibronectin was eliminated by three cycles of centrifugation and resuspension

in PBS. Microrods were incubated with a fibronectin antibody (ab26245, Abcam, Cambridge, MA) at a 1:1000 dilution for 1 hour at 37 ºC before centrifugation and resuspension in PBS three times; then, microrods were incubated with fluorescently-labeled secondary antibody (A21202, Thermofisher, Waltham, MA) at a 1:400 dilution for 1 hour at room temperature before imaging in a fluorescence microscope.

### 2.2.9 Statistical analysis

All values for continuous variables are listed as the mean ± one standard deviation, unless otherwise indicated. In vitro and in vivo analysis was performed using a one-way analysis of variance (ANOVA), followed by multiple comparison by Holm-Sidak correction to identify differences between groups.

## 2.3 Results

### 2.3.1 Fabrication of hyaluronic acid-based microrods in a range of stiffness

In order to fabricate hyaluronic acid microrods through photolithography, we adapted published protocols to functionalize HA with UV-sensitive methacrylate groups (Figure 2.1A)[109]. ^{1}H NMR spectroscopy confirmed the substitution of hydroxyls with methacrylate groups, showing methacrylate peaks at 6.1 and 5.65 ppm (Figure 2.1B). To determine the degree of substitution, we compared the integrations of the methacrylate peaks with the acetamide peak in HA at 1.85 ppm and found that we were able to reproducibly synthesize hyaluronic acid methacrylate (HAMA) with 41 ± 3% substitution.

A time course study was conducted on this reaction over 5 days to ensure completeness of reaction (Figure 2.1C). At each time point, a reaction sample was taken, purified and analyzed

by ^{1}H-NMR. Our results indicate that the reaction goes to completion after 24 hours, likely due to the reactivity of the glycidyl group to epoxide ring opening.

We have previously found that microrods must have an elastic modulus of at least 20 kPa in order to significantly affect cell behavior[92]. To determine the concentration of HAMA necessary to yield microrods of desired stiffness, we measured the elastic modulus of hydrogel slabs fabricated with a range of HAMA concentrations. Atomic force microscopy measurements showed that the modulus of these hydrogels increase exponentially from 1kPa to 160kPa with increasing HAMA concentration (Figure 2.2).

Photolithography was used to reproducibly create 15 x 15 x 100 µm HA microrods in a range of stiffness (Figure 2.3A). The dimensions of the microrods were controlled by the photomask while the stiffness was controlled by total HAMA concentration in the precursor solution. Brightfield microscopy confirmed uniform fabrication of HA microrods across the wafer (Figure 2.3B). Since HA is very hygroscopic, the fabricated HA microrods exhibit moderate swelling in solution. The dimensions of fully swollen HA microrods were confirmed by labeling HA microrods with a fluorescein label and imaging with confocal microscopy (Figure 2.3C).

*2.3.2 Degradation kinetics of hyaluronic acid microrods*

We conducted degradation studies on slabs of HAMA to understand the behavior of HAMA breakdown. Slabs of HAMA at varying concentration were incubated in buffer containing 100 U/mL, 10 U/mL and 0 U/mL of hyaluronidase. Samples were taken every two days and the degradation buffer was replenished. A carbazole-based detection assay was used to quantify the amount of HA released by degradation[110]. In samples incubated with 100 U/mL of

hyaluronidase, 25 mg/mL and 50 mg/mL HAMA slabs degraded quickly and were completely disintegrated at 2 and 4 days, respectively (Figure 2.4A). As HAMA concentration increased, degradation was much slower, as seen in the 75 mg/mL and 100 mg/mL slabs, which did not completely degrade until after 3 weeks. This can be attributed to the increasing number of crosslinks that can be formed at higher HAMA concentrations, as observed with the nonlinear increases in elastic modulus with increasing HAMA. This results in a tighter mesh network in which only HAMA fragments on the surface are accessible to hyaluronidase. This is consistent with our observation that 75 and 100 mg/mL HAMA slabs became smaller in size, but maintained their mechanical integrity (Figure 2.4B). By contrast, 25 and 50 mg/mL HAMA slabs became softer over a short period of time and then fully dissolved.

To confirm this, we compared degradation of 100 mg/mL HAMA slabs in 100 U/mL and 10 U/mL hyaluronidase. Not surprisingly, we found that slabs in 10 U/mL hyaluronidase degraded much slower than those in 100 U/mL hyaluronidase (Figure 2.4C-D). However, at two weeks, the rate of degradation for both groups became nearly identical. This suggests that there is an initial phase where there are many accessible HAMA fragments and degradation is dependent on hyaluronidase concentration; and that there is a second phase where the rate limiting factor is the number of accessible HAMA fragments on the surface of the slab. We propose that hydrolysis of the crosslinks, which occurs much slower than enzyme mediated chain scission, loosens the polymer network and is the limiting step in this phase of degradation. This suggests that geometry may be a major factor in determining degradation time, so we proceeded to repeat these studies with HA microrods.

HA microrods were made using 75 mg/mL and 100 mg/mL of HAMA and incubated in buffer containing hyaluronidase, as described above. Samples were taken every two days and

measured using the carbazole assay. Interestingly, we find that there is no significant difference between the degradation of 75 mg/mL and 100 mg/mL HA microrods (Figure 2.5A). The surface area to volume ratio of HA microrods is much greater than HAMA slabs, exposing more HAMA fragments to enzyme for degradation. As a result, the degradation of the HA microrods is also much faster than the HAMA polymer slabs. The 75 mg/mL and 100 mg/mL HA microrods were 50% degraded by 1 and 2 days, respectively, compared to their HAMA slab counterparts which were 50% degraded by 3 and 6 days. Differential interference contrast (DIC) imaging showed that these microrods degrade by surface erosion (Figure 2.5B).

We conducted additional degradation studies with physiological concentrations of hyaluronidase at lower pH to simulate inflamed tissue. HA microrods were made using 50 mg/mL HAMA and incubated at pH 5.7 in 0.26 U/mL hyaluronidase. Our data show that these microrods were approximately 80% degraded after 7 days (Figure 2.6).

### 2.3.3 Influence of hyaluronic acid microrods on cardiac fibroblasts and myocytes in vitro

We grew fibroblasts with HA microrods to evaluate the effect of HA microrods on fibroblast behavior *in vitro*. Primary neonatal rat ventricular fibroblasts (NRVFs) adhered to and spread on the HA microrods, often conforming to and enveloping the entirety of the rod (Figure 2.7). Paxillin staining showed that the NRVFs formed distinct focal adhesions to the edges of the microrods, potentially initiating several mechanotransduction pathways. These results were consistent in fibroblast/myocyte co-culture as well. The fibroblasts appeared to have a stronger affinity for the rods, stretching and spreading across the microrods while the myocytes formed tight attachments to the edges (Figure 2.8A). While a key binding partner to HA, CD44 was not found to be localized to the HA microrod and was instead present at high levels over the entire

fibroblast membrane (Figure 2.8B). We found that HA microrods readily bind to fibronectin, providing surface ligands for focal adhesion formation (Figure 2.9). Together, these data suggest that integrin-binding is a major mechanism for cell attachment to the microrods.

## 2.4 Discussion

In this work, we developed a novel materials-based strategy that combines the wound healing properties of hyaluronic acid with microtopographical cues to modulate the cellular phenotype. We fabricated discrete microrods using a photocrosslinkable derivative of HA, characterized their mechanical properties and enzyme-mediated degradation, and examined their interaction with cardiac fibroblasts and myocytes *in vitro*.

There have been significant advances within the past few decades on the use of micromechanical cues for modulating cell behavior. Microgrooves have been widely used to confine the growth of fibroblasts and cardiomyocytes into aligned rows and influence proliferation and differentiation[112,113]. Microposts in 2D and microstructures in 3D have been demonstrated to affect cellular phenotype by maintaining cellular tension via anchorage and has been used to attenuate the fibrotic response[90–93,113,114]. While applications of these materials have seen success, there remain opportunities to modify these materials for additional biological functionalities.

We utilized a glycidyl methacrylate synthesis strategy to functionalize the HA backbone with UV-curable pendant groups. This reaction mechanism was selected because precise control of reaction pH was not required, unlike syntheses utilizing methacrylic anhydride[109,115–117]. This provided an easy and reproducible way for us to synthesize HA methacrylate. There has been, however, much debate on the mechanism of this reaction. The attachment can occur either by

substitution of the carboxylic acid with the methacrylic acid group, or by epoxide ring opening via the 6' hydroxyl[109,118]. Recent studies have shown that under basic conditions, glycidyl methacrylate reacts with the 6' hydroxyl by both epoxide ring opening and transesterification, with the epoxide ring opening being the dominant mechanism[119]. As epoxides are highly reactive, we hypothesized that the reaction is complete after 24 hours, confirming this by a reaction time course (Figure 2.1C). This contrasts with previous protocols that necessitate 5-10 days of reaction time to get significant degrees of substitution[109]. Despite this, we were able to get consistent substitution efficiencies of between 40-45%. This efficiency varies quite drastically in the literature even when similar protocols are used. This can be attributed to the integration of NMR peaks during analysis. The reference peak used is generally of the acetamide protons, which has significant overlap with other peaks. This can result in highly variable calculation of substitution efficiency, depending on how the integration is done. Further, differences in purification protocol can cause differences in both yield and purity. While not shown here, we observed that changing the dialysis membrane from a 3k cutoff to a 10k cutoff reduced our yield by nearly 50%, possibly due to the polydispersity of HA fragments. Small fragments that were initially restricted by the 3k membrane can move through the 10k membrane. This would also affect the mechanical stiffness of hydrogels formed in later steps, highlighting the influence of each synthesis and purification step.

A significant advantage of HA microrods is that they are degradable by native physiological processes to accommodate new tissue growth[46,47,104,105]. While several studies have investigated the degradation behavior of covalently crosslinked HA hydrogels, it is necessary to characterize each new formulation since molecular weight, degree of methacrylation and weight percent can drastically affect degradation. In our study, we use lower molecular weight HA in

our synthesis to achieve high degrees of methacrylation (Figure 2.1B-C). Additionally, we can get higher concentrations of low molecular weight HA (LMWHA) compared to high molecular weight HA (HMWHA), allowing for fabrication of hydrogels in a greater range of stiffness (Figure 2.2). We used varying concentrations of hyaluronidase to understand the behavior of this degradation. For 100 mg/mL HA hydrogels, we observed an initial linear phase of degradation that was dependent on concentration of hyaluronidase (Figure 2.4C). This was followed by a second slow phase of degradation that was independent of hyaluronidase concentration. These data suggest that these HA hydrogels are first degraded through an enzyme mediated mechanism which break up the accessible HA chains on the surface of the hydrogels. When there is high crosslinking density, the enzyme will only degrade the exterior of the hydrogel, resulting in surface erosion. In contrast, looser hydrogel networks allow the enzyme to penetrate the interior and cause bulk degradation. This is also apparent by morphological analysis wherein lower weight percent HA hydrogels gradually lost mechanical integrity and eventually completely dissolved, while higher percent HA hydrogels became smaller over time, indicating surface degradation.

We originally hypothesized that fibroblasts bind to HA microrods via CD44 receptors on the cell surface, activating a sequence of signaling cascades that induce phenotypic changes. Fibroblasts display a high content of CD44 receptor and conform well to the microrod topography, suggesting that fibroblasts are responsive to HA microrods in the local environment (Figure 2.8). However, both myocytes and fibroblasts exhibit focal adhesions to the HA microrod contour. The deposition of fibronectin to HA explains how cells are able to attach to HA, a material that is traditionally believed to be non-adhesive (Figure 2.9). This is consistent with previous reports that HA is nonadherent during the first few hours of culture, but becomes

adherent and amenable to cell attachment after several hours have passed[120,121]. One possibility is that CD44 facilitates fibroblast association with the HA microrods while fibronectin supports continuous attachment[121,122]. Additionally, it has been shown that modification of the HA backbone can reduce its affinity for CD44[123]. It is possible that our ~41% modification of the 6C-OH is sufficiently high that it impairs the affinity of CD44 on the cell surface to the HA microrods. We therefore hypothesize that integrin binding is a key mechanism of interaction between fibroblasts and HA microrods, which may be amplified by other pathways involving HA and its receptors to cause phenotypic changes. Additional investigation is necessary to elucidate the precise interactions and mechanisms involved.

## 2.5 Conclusion

In summary, we synthesized a UV-curable hyaluronic acid derivative that can be crosslinked into discrete microrods through photolithography. The stiffness and degradation kinetics of these microrods are easily tuned by varying HA concentration in the precursor solution. We further demonstrate that these microrods are highly interactive with cardiac fibroblasts and myocytes and capable of eliciting phenotypic changes through biophysical and biochemical pathways. The antifibrotic effects and therapeutic benefits of these microrods will be discussed in Chapter 3.
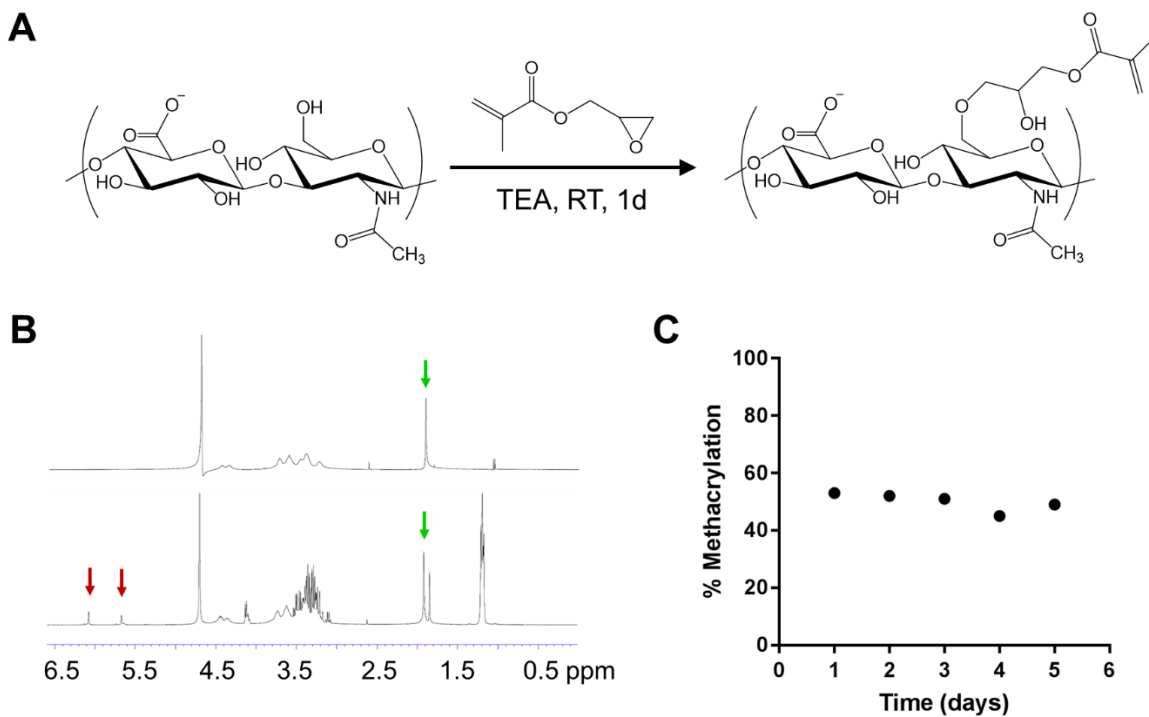
**Figure 2.1. Synthesis and characterization of hyaluronic acid methacrylate.** (A) Hyaluronic acid (100 kDa) was reacted with glycidyl methacrylate to add photosensitive pendant groups to the polymer backbone. (B) $^1$H-NMR was used to quantify the modification of HA (top) with methacrylate groups (red arrows). The product (bottom) had two methacrylate peaks at ~5.65 ppm and ~6.1 ppm, which was compared to the acetamide peak (green arrows) at 1.85 ppm to calculate the degree of substitution. (C) A time course study was conducted on this reaction and showed that the reaction was complete after 24 hours with no increase in % methacrylation with increasing reaction time.
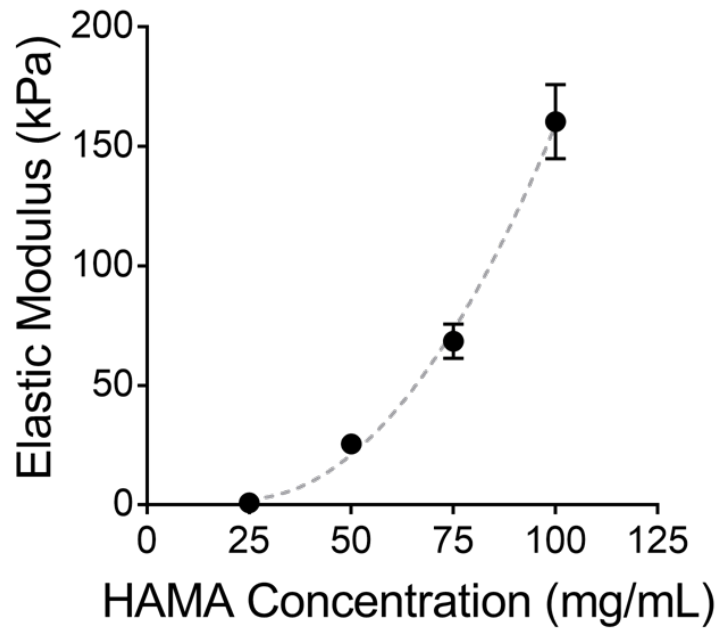
**Figure 2.2. Stiffness characterization of hyaluronic acid hydrogels.** A range of concentrations of HA methacrylate were used to fabricate HA hydrogels with elastic moduli between 1 kPa and 160 kPa. The data are presented as mean ± SD (n = 3 per group).
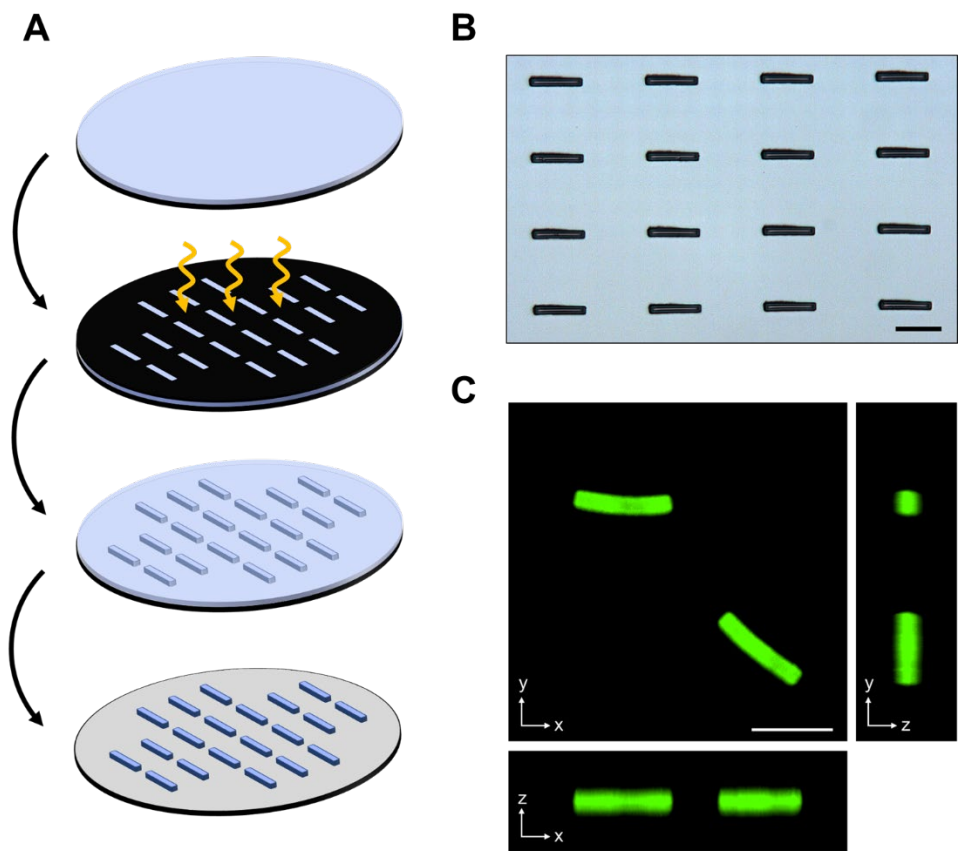
**Figure 2.3. Microrod fabrication and visualization.** (A) HA microrods were fabricated by exposure of a thin film of HAMA to UV light through a photomask followed by development in water. (B) Brightfield images of uniformly produced HA microrods on a silicon wafer. (C) Fluorescent images of HA microrods labeled with fluorescein indicate expected dimensions on all axes. Scale bars = 100 µm.
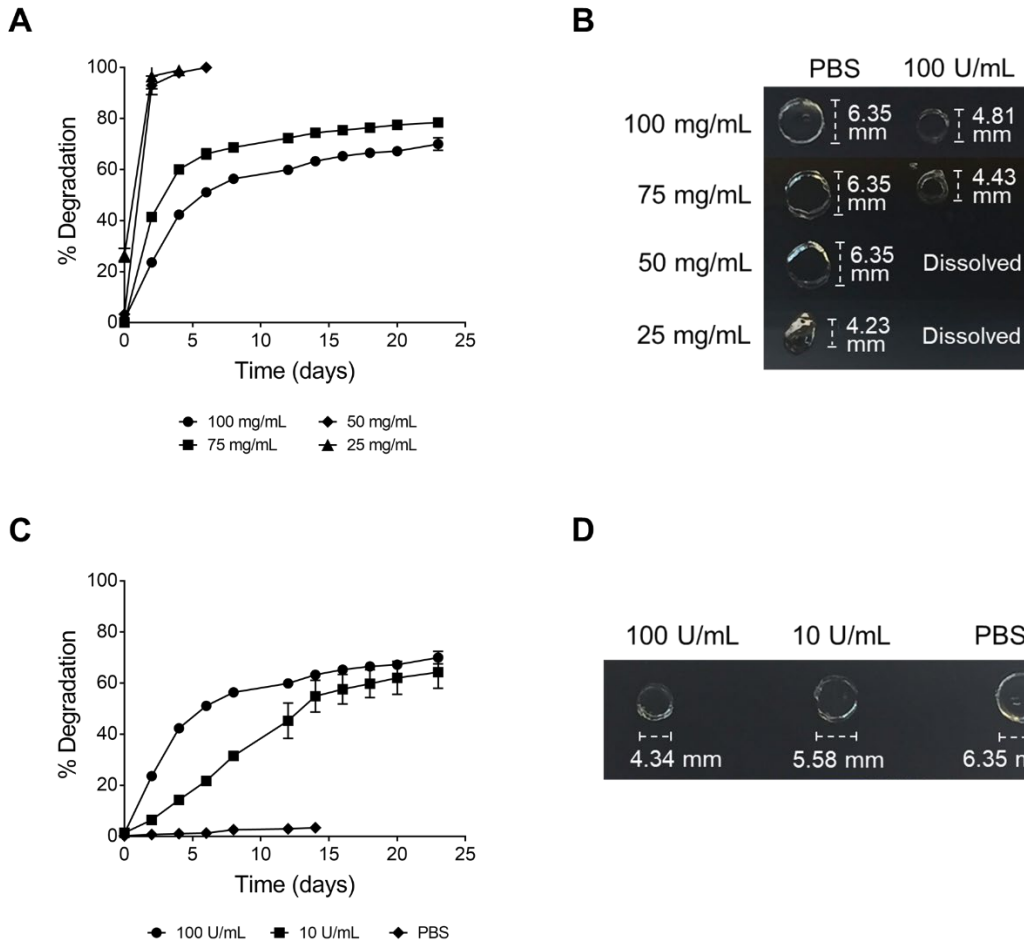
**Figure 2.4. Surface area and crosslinking density affect enzyme-mediated degradation of crosslinked HA.** (A) HA hydrogels made from higher HAMA concentration have reduced rates of hyaluronidase-mediated degradation due to increased crosslinking density (n = 3 per group). (B) Images of HA hydrogels after 16 days of degradation in 100 U/mL hyaluronidase compared to 0 U/mL hyaluronidase. (C) 100 mg/mL HA hydrogels degraded in a range of hyaluronidase concentration suggest biphasic degradation patterns consisting of enzyme degradation on accessible fragments on the surface. Hydrolysis creates new accessible fragments which are degraded by enzyme in the second, slower phase of degradation (100 U/mL: n = 3, 10 U/mL: n = 2, PBS: n = 3). (D) Images of 100 mg/mL HA hydrogels after 16 days of degradation in varying amounts of hyaluronidase.
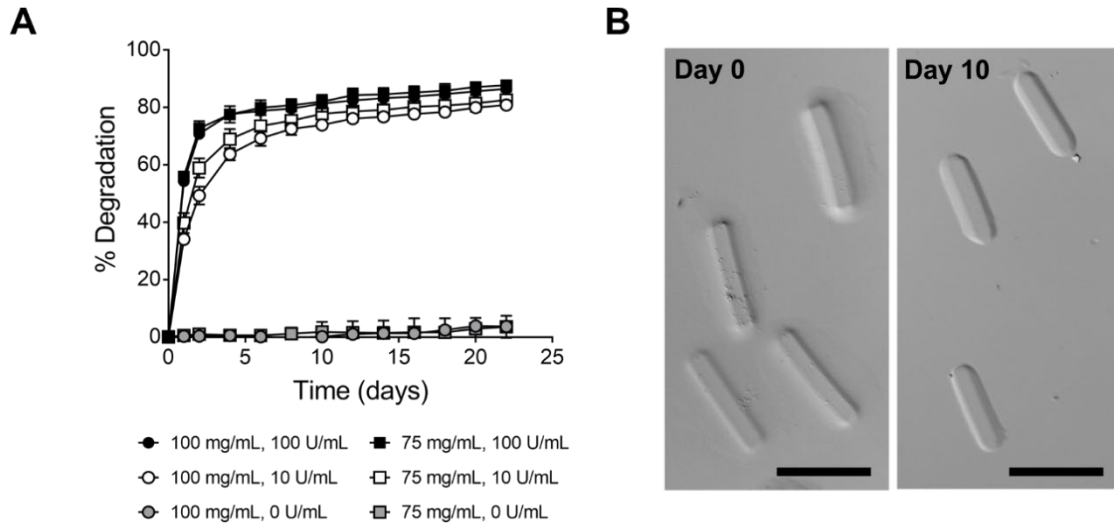
**Figure 2.5. Enzyme-mediated degradation of HA microrods occurs by surface erosion.** (A) Crosslinking density has limited effect on HA microrod degradation due to high surface area to volume ratio (n = 3 per group). (B) Differential interference contrast (DIC) images of 100 mg/mL HA microrods incubated in PBS (left) or 100 U/mL hyaluronidase (right) for 10 days demonstrates surface erosion of microrods. The data are presented as mean ± SD. Scale bars = 100 μm.
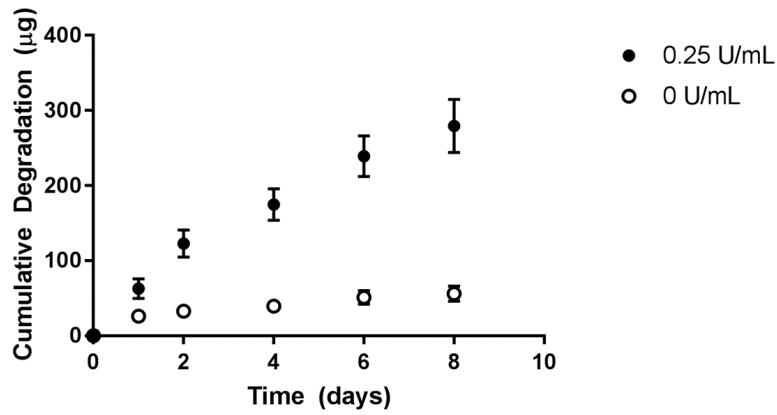
**Figure 2.6. Degradation of HA microrods in physiological concentrations of hyaluronidase.** 50 mg/mL HA microrods were degraded in 0.25 U/mL and 0 U/mL hyaluronidase to assess degradation in physiological concentrations of hyaluronidase. These microrods are expected to last over 2 weeks in the body. The data are presented as mean ± SD (n = 3 per group).
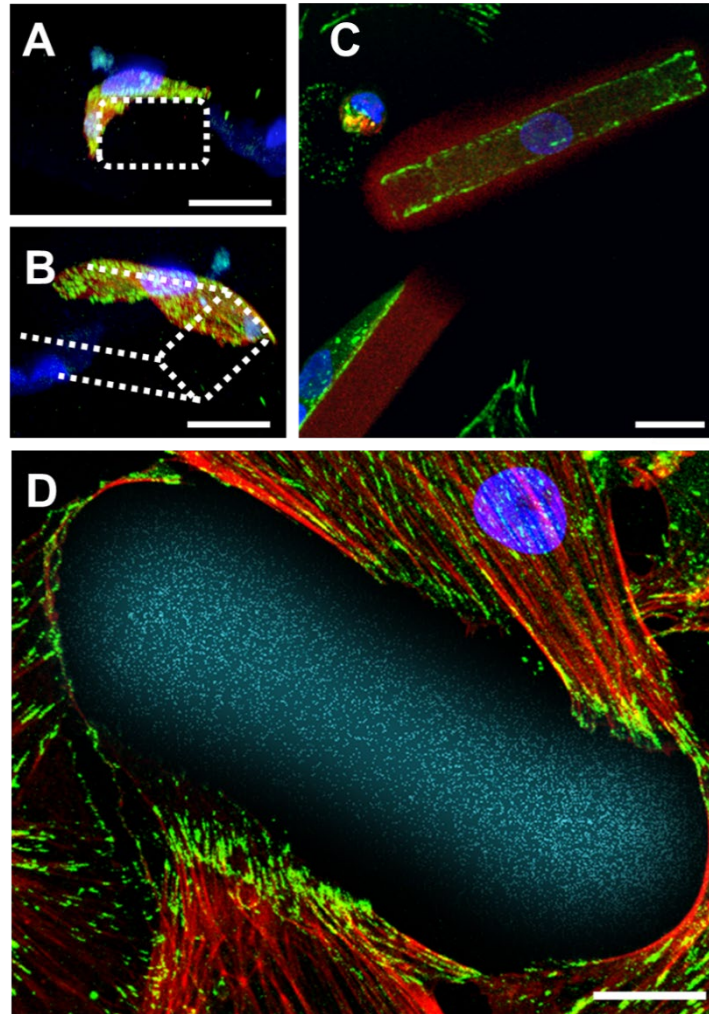
**Figure 2.7. Cardiac fibroblasts interact with HA microrods *in vitro*.** Fluorescent immunocytochemical staining show that neonatal rat ventricular fibroblasts are highly interactive with HA microrods. These interactions include wrapping around the microrods (A,B), spreading across the entire microrod surface (C), and forming focal adhesions to the edges of the microrod (D). Actin (red), paxillin (green), nuclei (blue), microrod (cyan). Scale bars = 20 μm.
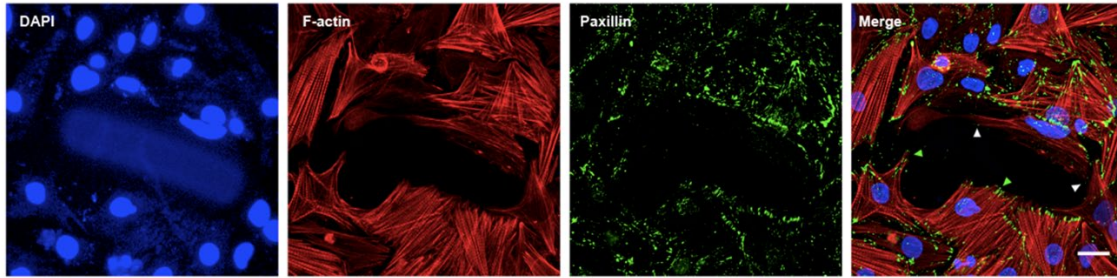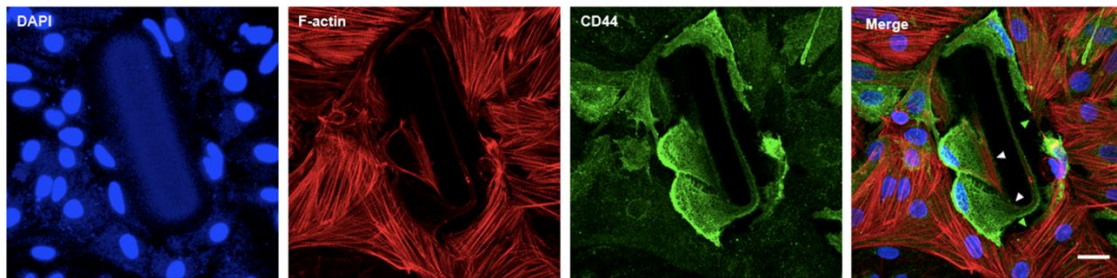
**Figure 2.8. Interaction of HA microrods with primary neonatal ventricular myocytes and fibroblasts in co-culture.** (A) Interaction of myocytes (green arrows) and fibroblasts (white arrows) with HA microrods via focal adhesions (paxillin). (B) CD44 receptor is more abundant in fibroblasts (white arrows) than in myocytes (green arrows). Staining of nucleus and HA microrods by DAPI (blue); F-actin by phalloidin (red); paxillin and CD44 with their respective antibodies (green). Scale bars = 20 µm.
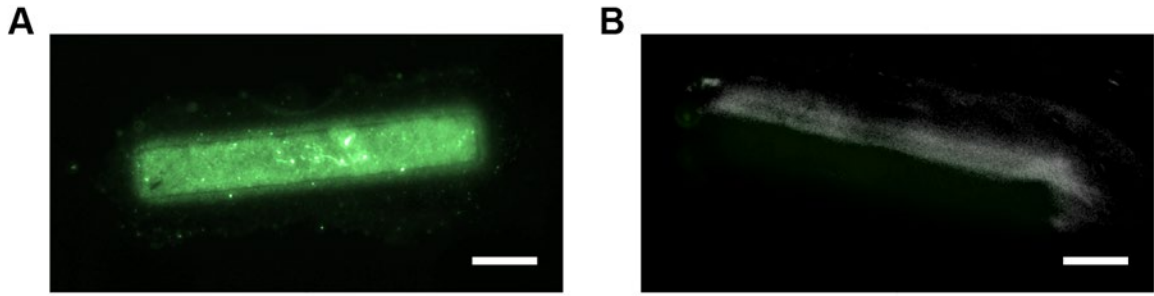
**Figure 2.9. Fibronectin binds to HA microrods.** Merged fluorescence and phase contrast images for (A) microrods incubated with fibronectin and (B) microrods with PBS alone. Scale bars = 20 μm.

## Chapter 3 – Assessment of HA Microrod Administration for the Treatment of Cardiac Fibrosis After MI

### 3.1 Introduction

Ischemic heart disease is the leading cause of death worldwide, accounting for nearly 10 million deaths in 2016[124]. While advancements in preventive and acute treatment of myocardial infarctions (MI) have improved patient outcomes and reduced mortality rates, the resulting tissue damage initiates pathological repair mechanisms that culminate in the formation of non-contractile scar tissue[3,5,10–13]. This progressive tissue stiffening results in additional stress on the heart and reduced cardiac output, which contributes to infarct expansion and left ventricular dilatation[3,7,125]. The lack of treatment for this maladaptive response leads to challenging chronic complications and eventual heart failure in a growing patient population.

Within the past 5 years, there have been significant efforts towards developing intramyocardial hydrogel injections for cardiac tissue repair after MI[42–45,126–128]. These hydrogels act as bulking agents to thicken and mechanically stabilize the damaged myocardium, decreasing left ventricle (LV) wall stress and limiting LV expansion. Furthermore, these materials can be tailored for delivery of pharmacological agents, biologics, or stem cells to support tissue regeneration through several mechanisms. Among the multitude of materials that have been investigated, injectable hyaluronic acid (HA) hydrogels have gained increasing attention for cardiac tissue regeneration due to the implications of HA in wound healing[52–55].

While these approaches have seen success in hindering the progression of heart failure, there lies significant potential in reprogramming native repair processes for healthy cardiac repair. In healthy tissue, cells intimately interact with the native extracellular matrix (ECM), which plays a critical role in regulating the organization, proliferation and differentiation of

33

progenitor and mature cell populations[129–131]. Upon injury, substantial cell death and upregulation of ECM degrading enzymes causes release of latent chemical factors as well as the loss of cell-cell and cell-ECM contacts. This dramatic loss of cellular tension and anchorage stimulates the remaining fibroblasts to undergo phenotypic changes that ultimately lead to excessive deposition of scar tissue[7,11–14,132–134]. We have previously demonstrated the use of polymeric microstructures to study how microscale topographical cues affect the fibrotic response[91–93,114]. These microstructures provided anchors for cardiac fibroblasts with anchors in a softer 3D environment and were able to reduce cell proliferation, myofibroblast differentiation and expression of collagens. Polyethylene glycol dimethacrylate (PEGDMA) microstructures were later used to attenuate cardiac fibrosis and reduce degeneration of cardiac function in a rat model of MI[93].

In chapter 2, we demonstrated the development of hyaluronic acid-based microrods for interaction with cardiac fibroblasts and myocytes. In this work, we demonstrate the application of these HA microrods towards comprehensive cardiac tissue repair after MI. We were able to promote cell growth, attenuate myofibroblast transformation, and preserve myocardial structure and function after MI to a greater extent than previously reports utilizing this bioactive and biodegradable material.

## 3.2 Materials and Methods

### 3.2.1 Materials

2-hydroxy-4′-(2-hydroxyethoxy)-2-methylpropiophenone (HMPP) and 2-methylbutane were purchased from Sigma-Aldrich (St. Louis, MO). Sodium hyaluronate (100 kDa) was purchased from Lifecore Biomedical (Chaska, MN). Hyaluronic acid methacrylate was custom

synthesized per protocols described in chapter 2. Collagenase type-II was purchased from Worthington Biochemical (Lakewood, NJ).

### 3.2.2 Fabrication of HA microrods

A 0.5% w/v solution of HMPP was prepared and used to dissolve hyaluronic acid methacrylate at 75 mg/mL or 100 mg/mL. Once fully dissolved, the precursor solution was centrifuged at max speed for 10 minutes to remove impurities. A 15 µm thick layer of this solution was deposited onto a piranha cleaned silicon wafer and exposed through a photomask to a 365 nm UV light source using a Karl Suss Mask Aligner to crosslink the hyaluronic acid methacrylate in rod shapes (15 µm × 100 µm). The microrods were then gently scraped off the surface of the wafer using a cell scraper and collected into water, allowing uncrosslinked regions of hyaluronic acid methacrylate to fully dissolve. The microrods were passed through a 150 µm mesh filter to remove large particles and washed thoroughly by centrifugation. The microrods are sterilized with 70% ethanol and resuspended in saline or cell culture medium prior to use.

### 3.2.3 Fibroblast and myocyte cell culture

NIH 3T3 mouse fibroblasts (ATCC, Manassas, Virginia) were cultured in the complete medium consisting of Dulbecco's modified Eagle's medium with 10% fetal bovine serum and 1% penicillin/streptomycin. Primary neonatal rat ventricular fibroblasts (NRVFs) and myocytes (NRVMs) were isolated from primary heart cultures obtained from neonatal rats according to Institutional and National Institutes of Health guidelines. Hearts were removed from 1- to 2-day-old Sprague-Dawley rats and cells isolated using collagenase type II, per previously established protocol[111]. Fibroblasts, which had been separated from myocytes during isolation, were cultured

an additional 2 days before detaching cells with trypsin and seeding in new dishes for experiments.

### 3.2.4 NIH 3T3 proliferation and gene expression

NIH 3T3 mouse fibroblasts were harvested and cultured with HA microrods (100 mg/mL) at a high ratio (1:5) or a low ratio (1:20) of microrods to cells. Cell proliferation was assessed at 24, 48 and 72 hours after initial seeding using a Cyquant assay (ThermoFisher Scientific, Waltham, MA). Experiments were done in triplicate. For gene expression studies, NIH 3T3 mouse fibroblasts were cultured with HA microrods for 48 hours. Genetic material was harvested and purified using the RNeasy Miniprep kit. RNA was converted into cDNA using the iScript cDNA synthesis kit (Bio-Rad Laboratories, Hercules, CA). A Viia7 qPCR machine (Life Technologies, Carlsbad, CA) was used to measure relative expression levels of gene targets as compared to a housekeeping gene. Expression levels of all genes were evaluated using SYBR Green Mastermix (Life Technologies, Grand Island, NY) and custom-made DNA primers (Integrated DNA Technologies, Coralville, IA) in triplicate for three biological replicates (Table 3.1).

### 3.2.5 Kymograph analysis of cardiomyocyte contractility

Neonatal ventricular cardiomyocytes were plated on fibronectin-coated dishes (10 µg/mL) or fibronectin-coated dishes with HA previously deposited (10,000 HA microrods/dish). A subset of dishes were chronically exposed to hyaluronic acid (0.042 mg) starting on the plating day. On the second day of incubation, kymographs derived from line scans with DIC illumination were used to derive cardiomyocyte contractile properties as described previously[135].

For HA microrods, line scans were developed on myocytes with close proximity to the HA microrods.

### 3.2.6 Infarct model and microrod injections

The animal protocol for induction of MI was approved by the Committee for Animal Research of the University of California, San Francisco and was performed in accordance with the recommendations of the American Association for Accreditation of Laboratory Animal Care.

The ischemia-reperfusion model used in this study has been extensively tested in our lab. All injections were performed successfully and there were no complications resulting from surgery or injection in any animal. Protocols were approved by the IACUC of UCSF.

To produce the MI model, female Sprague-Dawley rats (180–220 g) underwent occlusion of the left anterior descending coronary artery for 30 minutes followed by reperfusion while under general anesthesia achieved by inhalation of 2% L/min isoflurane[136]. The chest was then closed and the animal was allowed to recover. The rats were randomized two days after MI to saline-injected, HA solution-injected, or microrod-injected treatment groups, and were given one intramuscular injection into the heart wall under blinded conditions via ultrasound guided transthoracic injection using a 29-gauge syringe[136]. Each injection consisted of 50 µL of sterile 0.9% sodium chloride solution (n = 7), HA dissolved in sodium chloride solution at 4.2 mg/mL (n = 9), or 50,000 of microrods in sodium chloride solution (n = 7). Preliminary studies showed that 75 mg/mL HA microrods outperformed the 100 mg/mL microrods. 75 mg/mL HA microrods were used for all microrods injections presented in this study. Each injection was delivered to the center of the infarct region as visualized by hyperechoic signal on ultrasound. Successful injection was confirmed by a slight local increase in ultrasound signal in the vicinity

of the syringe, as well as a brief thickening of the LV wall.

### 3.2.7 Echocardiography

Transthoracic echocardiography was performed with a 15-MHz linear array transducer system (Sequoia c256, Acuson, Erlangen, Germany) on all animals under 2% L/min isoflurane. Echocardiography was done prior to injection on day two post-MI and six weeks post-injection using standard methods that have been performed reproducibly in our lab[93,136]. To determine left ventricular end diastolic volume (LVEDV), left ventricular end systolic volume (LVESV) and ejection fraction (EF) at 48 hours and six weeks, the ventricular shadow was outlined in both systole and diastole and the single plane area length algorithmic method was applied. Two-dimensional images were obtained in both parasternal long- and short-axis views at the papillary muscle level. Stroke volume (SV) was calculated by SV = LVEDV-LVESV, while change in EF was calculated by $\Delta EF = EF_{6\ weeks}-EF_{2\ days}$. Transverse images were obtained at three levels: basal (at the tip of the mitral valve leaflets), middle (at the papillary muscle level), and apical (distal to papillary muscle but before the cap of the cavity). All image analyses were performed in a blinded fashion. In cases where the ventricular shadow was not clearly identifiable in the 48 hour or six-week image, the heart in question was excluded from echocardiographic analyses. Cases where ejection fraction was above 50% at 48 hours were excluded because they indicated an insufficient infarct model.

### 3.2.8 Histology

Sacrifice was performed after six weeks by maintaining the animal at 5% L/min isoflurane for five minutes, followed by bilateral thoracotomy and injection of potassium

chloride into the right atrium to arrest the heart in diastole. The heart was then extracted and frozen in OCT (Sakura Finetech USA, Inc., Torrance, CA) on 2-methylbutane (Sigma Aldrich, St. Louis, MO) on dry ice and sectioned for histology and image analysis. Tissue blocks were cryo-sectioned at a thickness of 10 µm starting at the apex of the left ventricle and collecting 10 serial sections every 350 µm until 100 sections were collected. Sections were stained with H&E stains, Masson's Trichrome stain and Picrosirius red stains using standard protocols. For immunofluorescent stains, tissue sections were air dried and blocked with 10% serum, followed by incubation with primary and secondary antibodies using standard protocols. In brief, samples were incubated overnight with primary antibodies at 4 °C in a solution of 0.1% Triton X-100, 0.05% Tween-20, 10% goat serum and 1% BSA in PBS (anti-vimentin, anti-CD68, anti-CD3, anti-paxillin; Abcam, Cambridge, United Kingdom). After rinsing, secondary antibody was added for 45 minutes at room temperature. DAPI and AlexaFluor 546 phalloidin were added as a counterstain (Thermofisher Scientific, Waltham, MA).

### 3.2.9 Image analysis

A Nikon confocal microscope was used for fluorescence imaging of fibroblast interactions with HA microrods *in vitro*. Single-plane and Z-stack images were obtained using a 40x Nikon objective. Primary antibodies for paxillin [ab32084] and CD44 [ab157107] (Abcam, Cambridge, MA) were used at 1:250 and 1:1000 dilutions, respectively, incubated overnight, then counterstained with secondary antibody (A21207, Thermofisher Scientific, Waltham, MA), rhodamine phalloidin (R415, Thermofisher, Waltham, MA), and DAPI (H-1200, Vector Laboratories, Burlingame, CA).

For whole heart histology, brightfield images were taken using a Nikon 6D optical

microscope (NIKON Instruments, Inc., Melville, NY) with 4–20x magnification (H&E, Masson's Trichrome, Picrosirius Red). Fluorescent images were taken with a Nikon spinning disc confocal microscope at 40x magnification. All quantifications were performed using Nikon Elements. For wall thickness analysis, the minimum length across the infarct area was measured for each tissue section. The absolute minimum length across all available sections in a given heart sample was selected as the minimum wall thickness.

For collagen analysis, five sections of each heart were selected from throughout the coronal plane of the infarct zone and stained with picrosirius red to assess the distribution and density of collagen in the injured hearts. These sections were imaged under brightfield as well as under polarized light to visualize the collagen fibers. Infarct area was quantified and normalized to total area of the left ventricular free wall.

### 3.2.10 Statistical analysis

All values for continuous variables are listed as the mean ± one standard deviation, unless otherwise indicated. In vitro and in vivo analysis was performed using a one-way analysis of variance (ANOVA), followed by multiple comparison by Holm-Sidak correction to identify differences between groups.

## 3.3 Results

### 3.3.1 Influence of hyaluronic acid microrods on fibroblasts and myocytes in vitro

We grew NIH-3T3 fibroblasts with HA microrods to evaluate the effect of HA microrods on fibroblast behavior *in vitro*. Interestingly, interaction with HA microrods increased fibroblast proliferation when cultured over three days (Figure 3.1A). NIH-3T3 fibroblasts grown with HA

microrods in a 1:5 ratio of microrods:cells had increased proliferation rates compared to control cells grown on tissue culture plastic ($p < 0.01$). This contrasts with previous studies using PEGDMA microrods, which reduced fibroblast proliferation[92]. This can be attributed to HA having additional cell growth properties compared to PEG, which is considered relatively bioinert. Despite the increased proliferation of fibroblasts, gene expression studies showed a decrease in key fibrosis markers. In cells grown with HA microrods, there was a dose-dependent decrease in expression of collagen I (Col1A2) and alpha smooth muscle actin (αSMA), markers of a myofibroblast phenotype. (Figure 3.1B). In cells cultured in a 1:20 ratio of microrods:cells, Col1A2 expression was reduced to $0.31 \pm 0.04$ fold expression relative to cells grown without microrods ($p < 0.001$) while αSMA was reduced to $0.09 \pm 0.02$ fold expression ($p < 0.001$). This effect was more profound when the number of microrods was increased to 1 per 5 cells. Additionally, HA microrods significantly reduced TGFβ1 expression and Smad3 expression (Figure 3.1C, $p < 0.05$). These data suggest that the HA microrods act on the TGFβ-signaling pathway to reduce the myofibroblast phenotype. We further examined the effect of HA microrods on the expression of matrix metalloproteinases (MMPs), specifically MMP2 and MMP9. These MMPs are upregulated following myocardial infarction to facilitate the initial breakdown and remodeling of ECM. We found that MMP2 was significantly reduced in fibroblasts cultured with HA microrods compared to control cells (Figure 3.1D, $p < 0.05$), suggesting that HA microrods may attenuate aberrant ECM breakdown during the initial days after MI.

The effect of HA microrods on cardiomyocyte function *in vitro* was also evaluated. Neonatal rat ventricular myocyte (NRVMs) were cultured in the presence of HA microrods or soluble HA for 48 hours and compared to control cells. Kymographs were derived from line

scans under DIC illumination to determine the beats per minute and time to peak tension (Figure 3.2). No significance was found between groups, suggesting that neither HA microrods nor free HA interfere with the contractile properties of the NRVMs. Taken together, these results suggest that HA microrods show promise as a therapeutic strategy to promote regenerative processes in the infarcted myocardium while mitigating pathological scarring.

*3.3.2 Therapeutic effects of hyaluronic acid microrods in a rat model of MI*

An infarct was induced in rats by ischemia reperfusion to generate a cardiac fibrosis model. HA microrods, soluble HA or saline were delivered into the infarct zone by ultrasound-guided, transthoracic injection. Total HA mass was kept equal for soluble HA and HA microrod injections to account for the material effect of HA.

HA microrod treatment was shown to result in improved functional outputs (Figure 3.3, Figure 3.4). At six weeks, stroke volume was significantly greater in animals treated with HA microrods compared to animals treated with saline (Figure 3.3C, $p < 0.01$). Change in ejection fraction (EF) was determined by taking the difference in ejection fraction measured at 2 days (before injection) and 6 weeks (Figure 3.4). Rats treated with HA microrods have a positive improvement in ejection fraction (5.91% ± 3.67%) compared to HA solution controls (-0.36% ± 4.20%, $p < 0.05$) and saline controls (-8.22% ± 7.28%, $p < 0.001$). Animals treated with soluble HA also exhibited significant improvements in ejection fraction compared to saline ($p < 0.01$), suggesting beneficial effects from the material alone. There was no significant difference in left ventricular end diastolic volume (LSEDV) and left ventricular end systolic volume (LVESV) (Figure 3.3A-B).

Cryosections of heart tissue were stained with hematoxylin and eosin (H&E), Masson's

trichrome and Picrosirius red to evaluate the effect of microrod injection on the progression of cardiac fibrosis, as compared to injections of soluble HA or saline (Figure 3.5). Wall thickness measurements were performed on sections throughout the heart where the left ventricle cavity was visible. The left ventricular wall of hearts treated with HA microrods had greater minimum wall thickness ($1.22 \pm 0.38$ mm) compared to saline treated hearts ($0.70 \pm 0.24$ mm), which exhibited significant wall thinning (Figure 3.6A, $p < 0.05$). Animals treated with HA solution had moderate wall thinning compared to saline treated and HA microrod treated hearts ($1.03 \pm 0.21$ mm). Heart sections were then stained with Masson's trichrome and Picrosirius red to quantify the size and collagen content of the infarcts. A comparison of rats treated with HA microrods or soluble HA to those treated with saline showed moderate, although not significant, reduction in collagen deposition in the free wall of the left ventricle (Figure 3.6B, $p = 0.1$).

Examining the HA microrod injection area, we noted that the collagen deposited around the microrods was much less dense and not visible under polarized light, suggesting a local decrease in collagen deposition and maturation (Figure 3.7B,D). This contrasts with areas distant from the injection site where more dense collagen fibrils are present (Figure 3.7C,E). Immunofluorescence staining with markers of vimentin for fibroblasts and CD68 for macrophages indicated that both CD68-positive macrophages and vimentin-positive, CD68-negative fibroblasts were present at the injection site (Figure 3.8A). Additionally, we found that fibroblasts surrounding the HA microrods had more rounded nuclei compared to those found away from the injection site, which were spindle shaped and characteristic of activated myofibroblasts (Figure 3.8B). Immunofluorescent staining of actin and paxillin also showed that cells within the injection site interacted with the HA microrods and formed focal adhesions along the edges of the microrods (Figure 3.9). It is likely that this interaction locally reduces fibroblast

activation *in vivo* as was seen *in vitro*.

### 3.4 Discussion

In this work, we investigated the use of HA microrods to attenuate the fibrotic phenotype associated with pathological LV remodeling and encourage the repair of damaged cardiac tissue after MI. Our results indicate that HA microrods increase fibroblast proliferation while also reducing expression of fibrotic genes such as collagen I and alpha smooth muscle actin. Additionally, these microrods can be injected into the infarcted myocardium to deliver biophysical and biochemical cues to preserve myocardial wall structure and function.

Previous studies have utilized bulk HA injections to mechanically support the damaged myocardium and preserve cardiac function after MI[51–54]. These strategies typically use biocompatible crosslinking chemistries to form the HA hydrogel *in situ*. While this allows for noninvasive catheter-based delivery, the gelation kinetics of HA in these cases can present significant challenges. Rapid gelation can lead to clogging of the catheter during the multiple injections required for treatment, while slow gelation results in diffusion of the hydrogel material into the tissue, leading to compromised hydrogel structure and mechanical properties[44,137]. Utilizing a rigorous interdisciplinary approach, we developed HA microrods to overcome these limitations. These discrete microstructures were fully crosslinked and characterized before injection and can be delivered to the myocardial wall by catheter injection without risk of clogging. Additionally, the ability to crosslink prior to injection gives tighter control over cell shaped morphology and hydrogel stiffness in the physiologic range, which are both crucial properties for mechanotransduction[94–96].

Within the past several decades, mechanical signaling has gained appreciation as a powerful mechanism for controlling cell behavior[94–100]. This includes mechanical stiffness, shear

forces and topography. In contrast to bulk polymer injections that reduce wall stress by providing mechanical support and preventing LV dilation, discrete HA microrods provide local micromechanical and biochemical signals to reprogram the cells of the myocardium. We have used both polypropylene microfibers and polyethylene glycol (PEG) microstructures to supply external mechanical cues and reduce myofibroblast differentiation[91–93]. HA microrods were shown to attenuate the fibrotic response to a greater degree than previously developed materials, likely due to the added biochemical effects of HA (Figure 3.1). Chopra *et al* reported the role of HA receptor binding in integrin mediated mechanotransduction[121,122]. Mesenchymal stem cells and fibroblasts were able to anchor to soft HA hydrogels containing fibronectin and observed increased rates of proliferation compared to soft polyacrylamide gels with fibronectin. Our cell proliferation data are consistent with these results, suggesting that the pro-proliferative effects of HA are preserved. Additionally, expression of key myofibroblast markers, αSMA and collagen 1, were reduced in NIH-3T3 fibroblasts to a greater extent compared to our studies with PEG microrods, an inert microtopographic cue[92].

The results of our *in vivo* experiments support these observations as well. The introduction of HA microrods 2 days after the initial infarct provides anchors for fibroblasts, macrophages and other cell types. Cells found at the injection site interacted with the microrods through focal adhesions, likely due to the increased stiffness relative to surrounding tissue (Figure 3.9). We propose that this stiffness differential leads to attenuation of the myofibroblast phenotype, manifesting in decreased deposition of collagen, reduced wall thinning and improved cardiac output. Similar to our *in vitro* results, HA microrods improved LV ejection fraction ($5.91\% \pm 3.67\%$) to a greater degree as compared to previous studies using PEG microrods (-$2.59\% \pm 8.11\%$)[93]. At 6 weeks, cardiac function of HA microrod treated hearts surpassed

baseline, post-infarct function, highlighting the potential of this technology to promote endogenous repair mechanisms not previously seen in materials-based approaches. We investigated whether this was due solely to the biological effect of HA by injecting a solution of HA into the heart wall after MI. The concentrations used were not high enough to generate a stiff gel, yet there were also improvements on cardiac function (Figure 3.3, Figure 3.4). This is likely due to the wound healing properties of HA, which may contribute to the results seen in studies involving bulk HA injections[50,106,138].

The goal of this study was to fabricate bioresorbable microstructures capable of delivering biophysical and biochemical cues and evaluate their potential for treating the progression of cardiac fibrosis post-MI to improve functional outcomes. These HA microrods act through mechanotransduction pathways to reduce fibrosis and maintain the structural integrity of the myocardium. Additionally, crosslinked HA can be compared to high molecular weight HA, which has anti-inflammatory effects that can limit pathological ECM remodeling during the initial days after an infarct[46,104,106,107]. Throughout degradation, these HA microrods are expected to release HA oligosaccharides that have been demonstrated to promote wound healing[46,49,106,139]. While it is difficult to investigate and tune the temporal interplay of mechanotransduction pathways and biochemical HA signaling pathways, our findings demonstrate that these two modes of action have significant implications for cardiac regeneration. By probing these individual pathways and responses, we will be able to optimize this novel microstructure-based technology to initially reduce the aberrant fibrotic response with micromechanical cues and later stimulate vascularization and other endogenous repair mechanisms for comprehensive myocardial repair.

**3.5 Conclusion**

Our acellular microrod approach is unique and provides biodegradable and bioactive micromechanical signals to directly limit fibrosis and favorably influence the microenvironment to attenuate myocardial wall thinning and improve LV function. Introduction of these microrods to the injured heart provided anchors to surrounding cells during initial inflammatory processes when the ECM is being degraded. This micromechanical interaction attenuated the fibrotic phenotype and improved morphological and functional outcomes in a rat ischemia-reperfusion model of MI. In the future, this innovative strategy can be co-implemented with pharmacologic and cell-based therapies to further advance our limited clinical capabilities in treating the chronic complications of MI.

| Target Gene | Forward Primer (5'->3') | Reverse Primer (5'->3') |
|---|---|---|
| GAPDH | AGGTCGGTGTGAACGGATTTG | TGTAGACCATGTAGTTGAGGTCA |
| Rpl19 | CATTTTGCCCGACGAAAGGG | GATCTGCTGACGGGAGTTGG |
| αSMA | GCTGCTCCAGCTATGTGTGA | CCATTCCAACCATTACTCCCTGA |
| Col1α2 | AAGGGTGCTACTGGACTCCC | TTGTTACCGGATTCTCCTTTGG |
| MMP2 | CAAGTTCCCCGGCGATGTC | TTCTGGTCAAGGTCACCTGTC |
| MMP9 | GGACCCGAAGCGGACATTG | CGTCGTCGAAATGGGCATCT |
| TGFβ1 | GGACTCTCCACCTGCAAGAC | CTGGCGAGCCTTAGTTTGGA |
| TβRII | ACGTTCCCAAGTCGGATGTG | TGTCGCAAGTGGACAGTCTC |
| Smad3 | AAGGCGACACATTGGGAGAG | GGGCAGCAAATTCCTGGTTG |

**Table 3.1. Primer pairs for qPCR**. GAPDH, glyceraldehyde 3-phosphatedehydrogenase; rPL19, ribosomal protein L19, αSMA, alpha smooth muscle actin; Col1α2, collagen type I, MMP2, matrix metalloproteinase-2; MMP9, matrix metalloproteinase-9; TGFB1, transforming growth factor beta-1; TBRII, TGFB receptor type II; Smad3, SMAD family member 3.
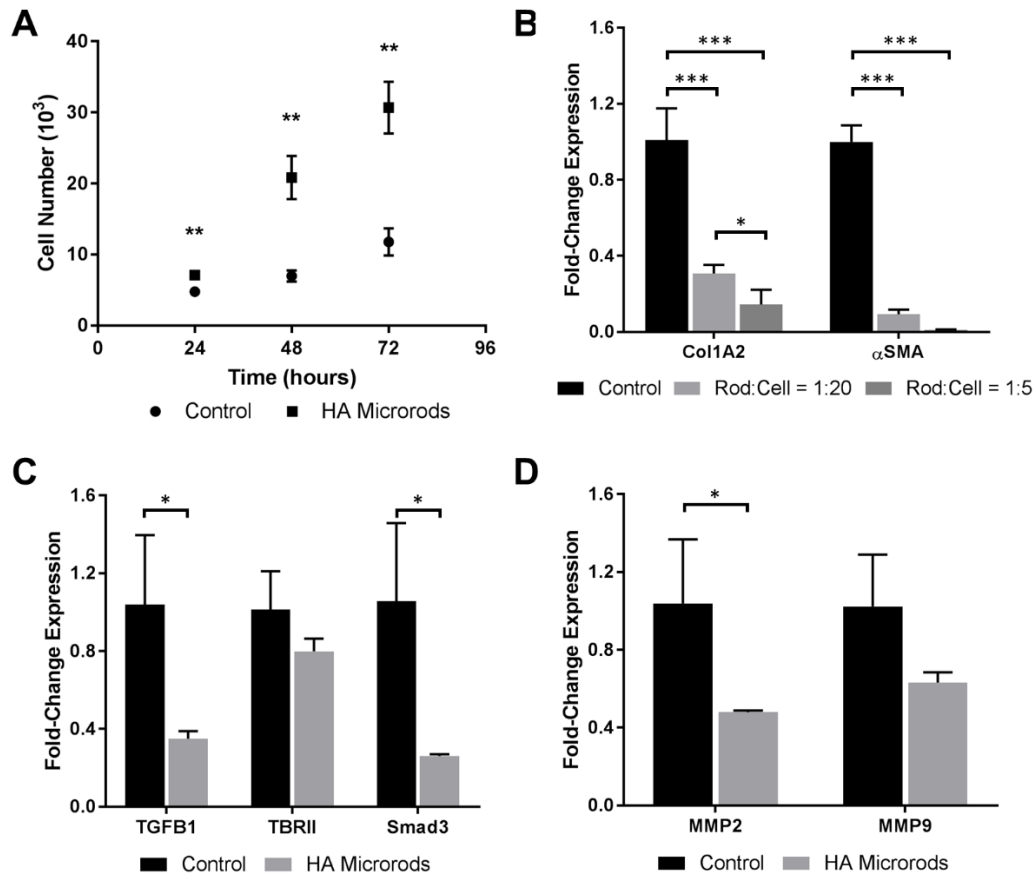
**Figure 3.1. HA microrods modulate the phenotype of fibroblasts *in vitro*.** (A) NIH-3T3 fibroblasts cultured with HA microrods have increased proliferation compared to control cells (n = 3 per group). (B) NIH-3T3 fibroblasts exhibit dose-dependent reduction in Col1A2 and αSMA expression when cultured with HA microrods for 48 hours (n = 3 per group). (C) HA microrods reduce TGFβ1 and Smad3 expression in NIH-3T3 fibroblasts when cultured at a density of 1 rod per 5 cells. (D) MMP2 expression is reduced in NIH-3T3 fibroblasts cultured with HA microrods at a density of 1 rod per 5 cells. The data are presented as the mean ± SD. *$p < 0.05$, **$p < 0.01$, ***$p < 0.001$.
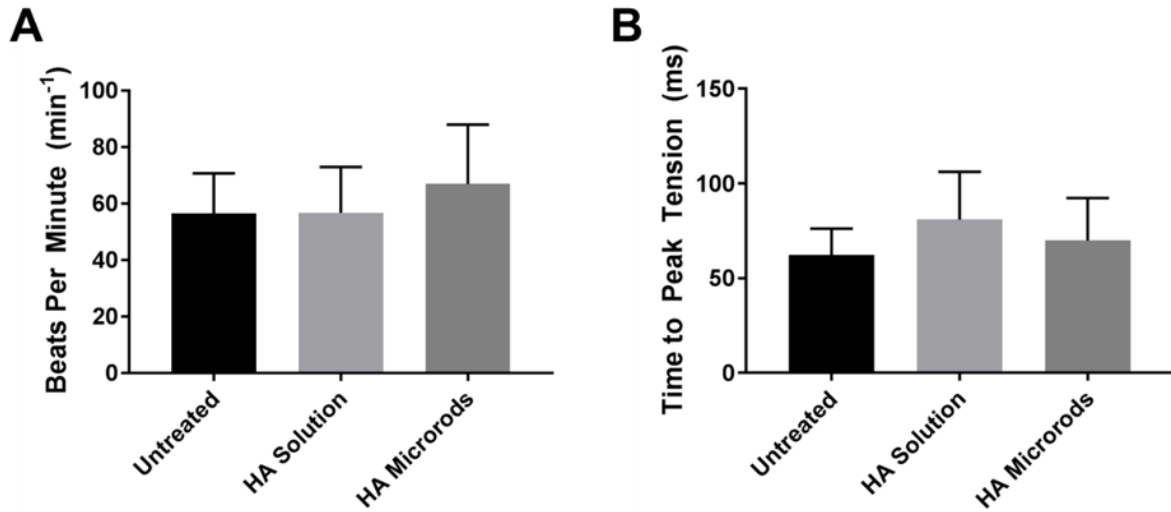
**Figure 3.2. HA microrods or soluble HA do not interfere with neonatal ventricular cardiomyocyte contractility.** Myocytes were plated on glass-bottom dishes (control), in the presence of HA microrods, or chronically incubated with 0.042 mg of HA per dish (HA). Kymographs reveal no significant difference in (A) beats per minute, or (B) time to peak tension relative to control measurements (mean ± SD; n = 15, 15, and 14 for control, HA microrods, and HA, respectively). The data are presented as the mean ± SD.
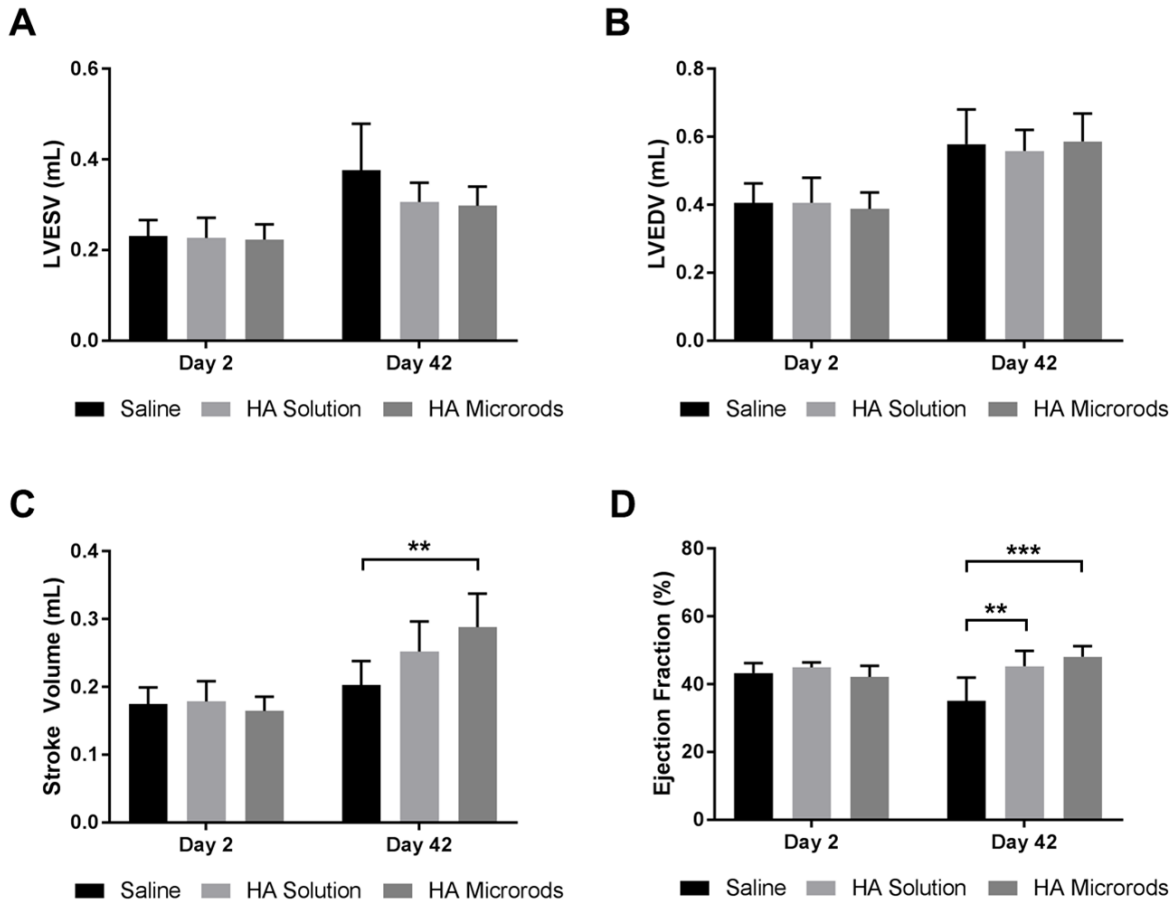
**Figure 3.3. HA microrods improve functional outcomes after MI.** Echocardiography was used to measure the (A) end systolic volume and (B) end diastolic volume immediately prior to injection (2 days after MI), as well as 6 weeks after injection in rats treated with saline (n = 6), soluble HA (n = 9) and HA microrods (n = 7). (C) Stroke volume and (D) ejection fraction were quantified per animal. Animals treated with HA microrods had significantly increased stroke volume and ejection fraction compared to saline controls. The data are presented as the mean ± SD. **$p < 0.01$.
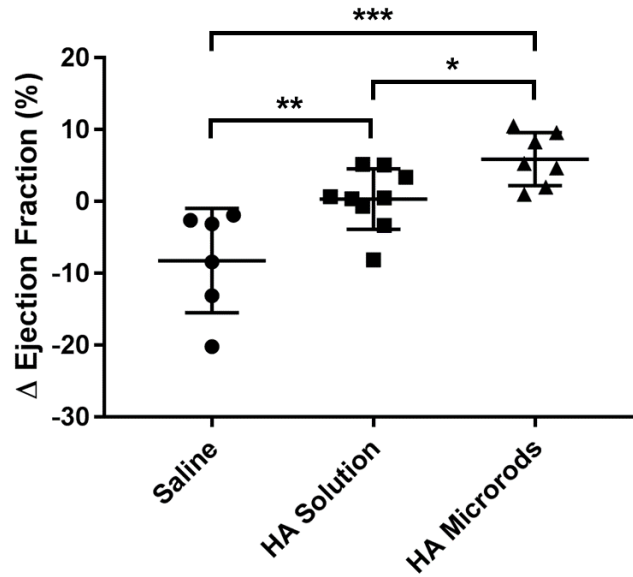
**Figure 3.4. Ejection fraction is significantly improved in rats treated with soluble HA and HA microrods.** Echocardiography was used to compare the ejection fraction (EF) 2 days after MI (immediately prior to injection) and 6 weeks after injection in rats treated with saline (n = 6), soluble HA (n = 9) and HA microrods (n = 7). Rats treated with HA microrods have significantly higher change in EF over rats treated with saline or HA solution. The data are presented as the mean ± SD. *$p < 0.05$, **$p < 0.01$, ***$p < 0.001$.
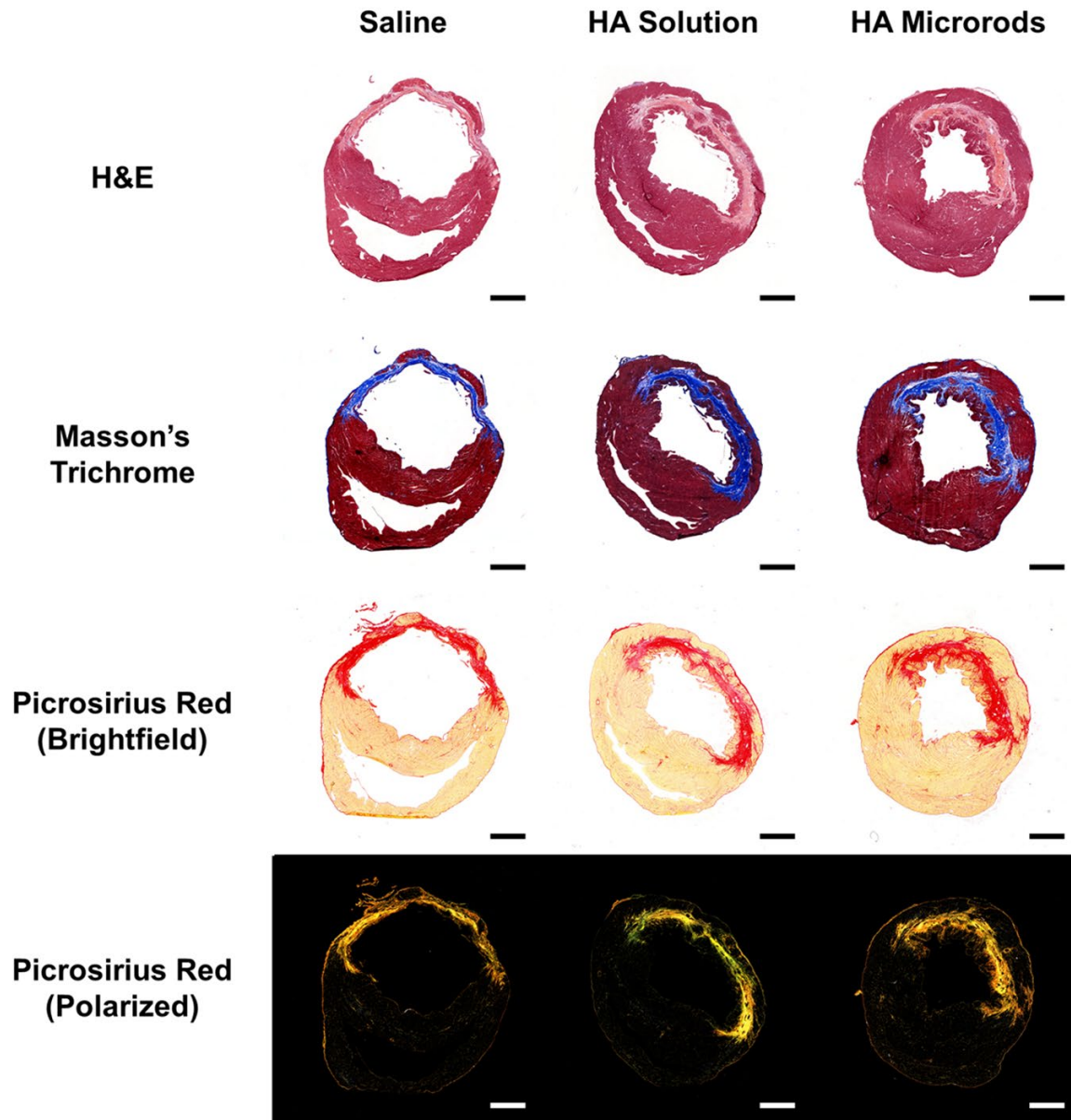
**Figure 3.5. Histological assessment of HA microrod and soluble HA treatment after MI.** Cardiac tissue sections were stained with H&E, Masson's Trichrome and Picrosirius red to visualize cell infiltration, vascularization and scar tissue formation. Scale bars = 2 mm.
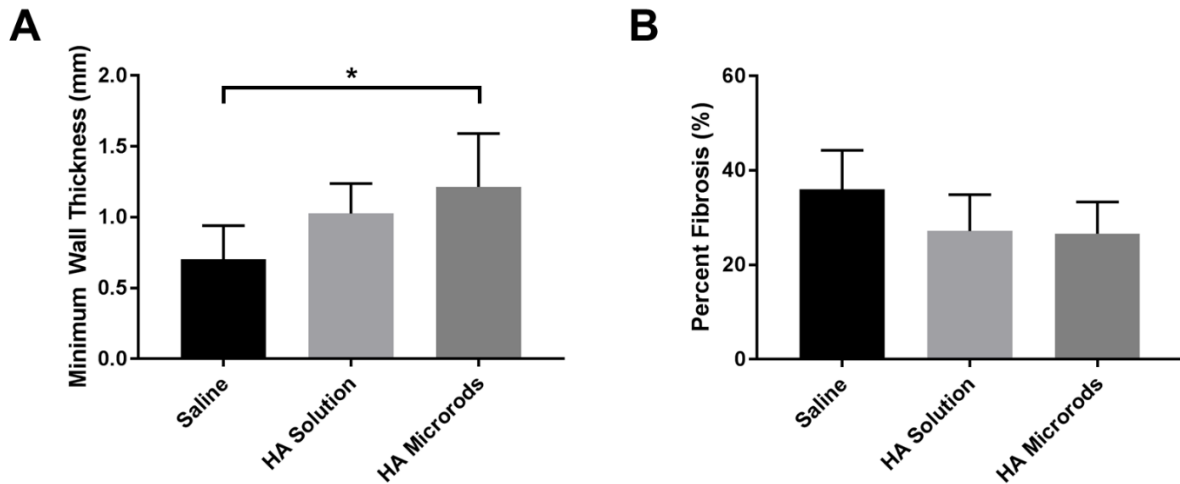
**Figure 3.6. HA microrods attenuate left ventricular remodeling after MI.** (A) Left ventricular wall thinning was significantly reduced in hearts treated with HA microrods (n = 6) compared to saline injection (n = 7). Hearts treated with HA solution had moderate but not significant wall thinning (n = 8). (B) Tissue sections were stained with picrosirius red stain and visualized under polarized light. Fibrosis area in the free left ventricular wall was measured and normalized to total area. While not significant (p = 0.1), fibrosis appears to be moderately reduced after injection of soluble HA and HA microrods. The data are presented as the mean ± SD.
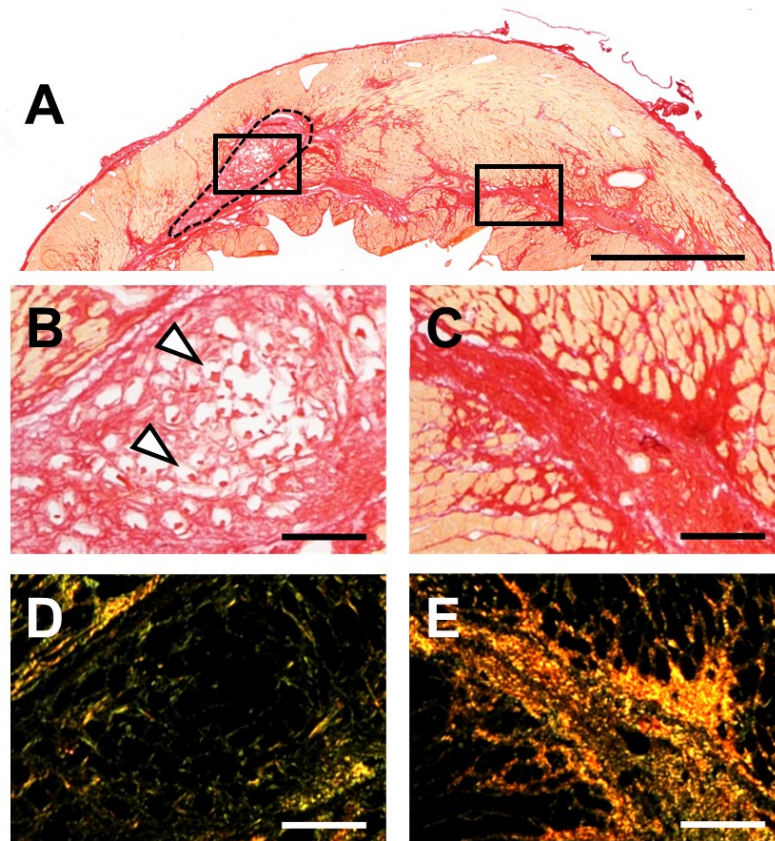
**Figure 3.7. HA microrods interact with fibroblasts *in vivo* and locally reduce collagen deposition.** (A) A representative Picrosirius red stained section of a HA treated heart. The dotted shape indicates the injection site. Collagen around the injection site (B,D) was sparse compared to far away from the injection site (C,E). The collagen near the microrods (white arrows) is loose and does not appear under polarized light, while the collagen away from the injection site matures into dense bundles. Scale bars = 2 mm (A) and 200 μm (B-E).
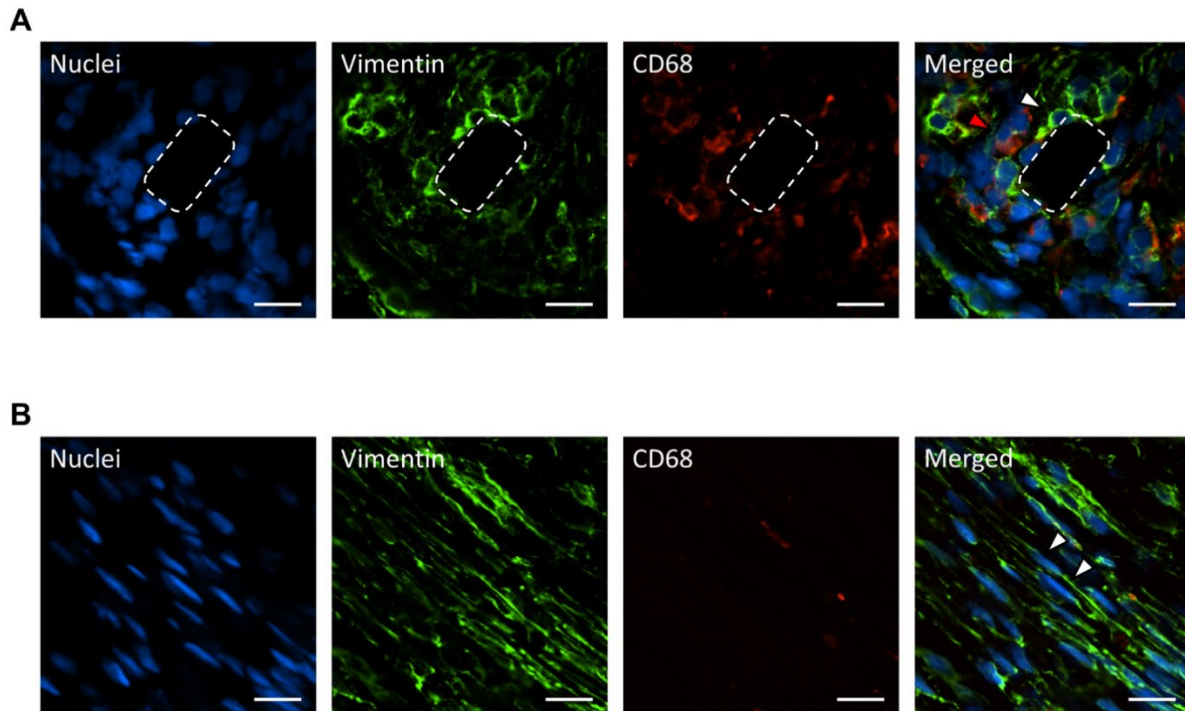
**Figure 3.8. Characterization of cell type and morphology in the injection and infarct sites.** (A) Confocal images of cells stained for vimentin, CD68 and nuclei show that both macrophages (CD68 positive, red arrow) and fibroblasts (vimentin positive, CD68 negative, white arrow) are present around the microrods. These cells appear to adopt a more rounded phenotype. (B) Fibroblasts (white arrows) located in the infarct scar and far from the microrods adopt a more stretched out morphology, characteristic of an activated phenotype. Scale bars = 20 µm.
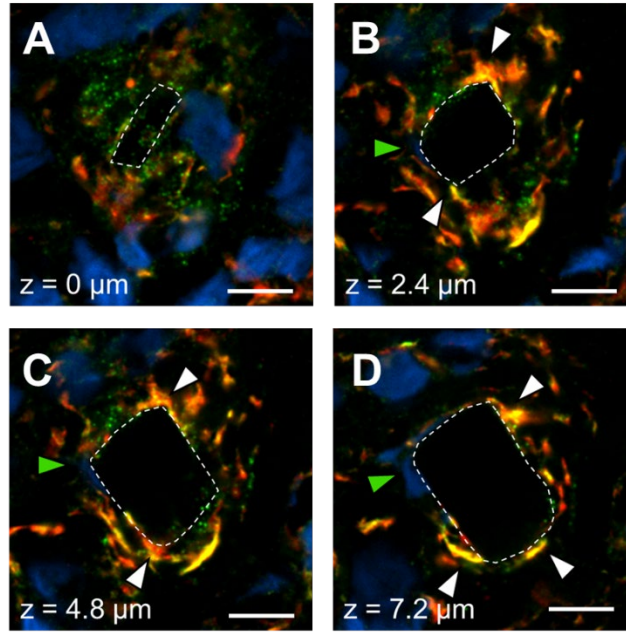
**Figure 3.9. Fibroblasts locally interact with HA microrods *in vivo* through focal adhesions.** Confocal images of microrods show that cells interact closely with HA microrods *in vivo*. Cells formed distinct focal adhesions (white arrow) formed along the edges of the microrods. Tissues were stained for nuclei (blue), actin (red) and paxillin (green). Scale bars = 10 μm.

# Chapter 4 – Novel Functionalization of Polymeric Microrods for Drug Delivery and Tissue Engineering Applications

## 4.1 Introduction

As described in the previous chapters, microtopography is very powerful for tissue engineering applications. While impactful through a biophysical mechanism alone, one notable benefit of using polymeric microstructures is that they can be modified with a variety of chemistries to impart additional functionalities for drug delivery or tissue engineering applications. In this chapter, we present a collection of studies that illustrate the boundless potential of polymeric microstructures as both research and therapeutic materials.

## 4.2 Materials and Methods

### 4.2.1 Materials

Poly(ethylene glycol) dimethacrylate (PEGDMA, $M_n$ = 750), N-vinylpyrrolidone (NVP), 2-hydroxy-4′-(2-hydroxyethoxy)-2-methylpropiophenone (HMPP), l-alanine, 2-aminoethyle methacrylate (AEMA), Tween 20, iron(II) chloride tetrahydrate, iron(III) chloride hexahyrate, ammonium hydroxide, tetraethyl orthosilicate (TEOS), and (3-mercaptopropyl)trimethoxysilane (MPTMS) were purchased from Sigma Aldrich (St. Louis, MO). Fluorescein-NHS, N′-ethylcarbodiimide hydrochloride (EDC), and N-hydroxysulfosuccinimide (NHSS) were purchased from Thermo-Fisher Scientific (Waltham, MA). DNA-NHS was custom synthesized by the Gartner Lab at the University of California, San Francisco. Hyaluronic acid (HA) methacrylate was synthesized in our lab as described in chapter 2.  HepIII (GEFYFDLRLKGDKY) and HepIII-FITC were custom synthesized by GenScript (Piscataway, NJ).  NVP-AEW541 was purchased from ApexBio (Houston, TX).

*4.2.2 Preparation of alanine-loaded PEGDMA microrods*

Precursor solutions consisting of PEGDMA (80%, 50% or 20% v/v), alanine (15 mM, 150 mM, 600 mM respectively) and 10% NVP containing 100 mg/mL HMPP were prepared in phosphate buffered saline (PBS). The solutions were then vortexed to ensure thorough mixing of reagents.

Microrods were fabricated by standard photolithographic techniques[92,93]. Briefly, the precursor solution was spun to a 15 µm thick layer onto a piranha-solution-cleaned silicon wafer (Addison Engineering, San Jose, CA) and exposed through a photomask to a 365 nm UV light source using a Karl Suss MJB3 mask aligner (Suss Microtec, Garching, Germany) to crosslink the desired regions in the shape of microrods (100 µm × 15 µm). The microrods were briefly developed in deionized water, rinsed in isopropanol, and dried with nitrogen gas. Immediately prior to experiments, microrods were removed from the silicon wafer by rinsing the wafer with 70% ethanol and gently scraping off the microrods with a cell scraper. The collected microrods were exchanged into PBS and immediately used.

Alanine-loaded microrods were incubated in 1 mL of PBS at 37 °C. At various time points, the microrods were pelleted by centrifugation and the supernatant was collected and replaced with fresh buffer solution. Alanine concentration was determined using a coupled enzyme reaction kit (Sigma-Aldrich).

*4.2.3 Cell viability experiments*

20% PEGDMA microrods loaded with alanine were selected for cell culture experiments. Primary mouse islets were obtained and cultured at low density (20 islets/mL) or high density (1000 islets/mL) with and without alanine supplement in the form of free alanine or alanine

loaded microrods ($10^4$ and $2\times10^4$ microrods). After 5 hours, cell viability was quantified by propidium iodide staining and flow cytometry.

### 4.2.4 Functionalization of PEGDMA microrods with surface molecules

PEGDMA microrods were prepared as above with slight modifications to incorporate primary amine groups on the surface. Briefly, AEMA was dissolved in 50% dimethyl sulfoxide (DMSO) in water at 0, 10, 50, 100 and 500 mM concentrations. Additionally, a solution of HMPP photo-initiator was prepared in NVP at 100 mg/mL. A precursor solution was prepared by combining PEGDMA, AEMA solution, photo-initiator solution and water in a 70:10:10:10 ratio. Microrods were fabricated by photolithography as described above.

Fluorescein-NHS was attached to the microrods in order to determine the conjugation capacity of the microrods. Aliquots of each microrod formulation were washed into 100 mM 4-(2-hydroxyethyl)-1-piperazineethanesulfonic acid (HEPES) buffer (pH 8.3) by centrifugation. To 450 µL of microrods, 50 µL of 10 mM fluorescein-NHS in DMSO was added and reacted overnight. The microrods were then washed 3x by centrifugation prior to imaging and quantification. DNA-NHS was conjugated to the microrods through similar methods.

### 4.2.5 Fabrication and loading of PEGDMA microrods with IGF-1R inhibitor

A precursor solution containing 50% PEGDMA in PBS was mixed in a 10:1 ratio with NVP containing 100 mg/mL of the photo-initiator, HMPP. The solution was spun to a 15 µm thick layer on a piranha-solution-cleaned silicon wafer and exposed through a photomask to a 365 nm UV light source using a Karl Suss MJB3 mask aligner to crosslink the desired regions in the shape of microrods (100 µm × 15 µm). The microrods were rinsed, scraped from the surface

gently using a cell scraper, and washed in PBS over 3 days to remove excess initiator. PEGDMA

microrods were lyophilized in 1% Tween 20 and rehydrated in 2 mM (0.88 mg/mL) of NVP-

AEW541 over 3 days.


*4.2.6 Release kinetics of NVP-AEW541*

PEGDMA microrods loaded with NVP-AEW541 were washed 3x in 0.1% Tween 20 in

PBS and reduced to a final volume of 150 µL. Over 9 days, samples were taken and the release

buffer was replenished. Concentration of NVP-AEW541 in each sample was determined by

absorbance at 285 nm, as well as by high performance liquid chromatography. Each replicate

contained $8 \times 10^5$ microrods.


*4.2.7 Gene expression analysis of ATDC5 cells with NVP-AEW541 loaded microrods*

Chondrogenic ATDC5 cells were cultured in complete medium consisting of 1:1 DMEM

(2 mM L-glutamine, 4.5 g/L glucose) and Ham F12 supplemented with 5% fetal bovine serum

(FBS), 1 U/mL penicillin/streptomycin, 0.25 ng/ml fungizone, insulin-transferrin-selenium (ITS,

contains 1000 mg/L human recombinant insulin, 550 mg/L human recombinant transferrin and

0.67 mg/L selenious acid). Secondary medium consisting of primary medium supplemented with

0.05 mg/mL ascorbic acid and 10 mM B-glycerophosphate was used for experiments. Cells were

plated in a 24-well plate and grown until confluent. Cells were serum starved for 8 hours prior to

experiments and then treated with IGF-1 (100 ng/mL) along with free IGF-1R inhibitor, IGF-IR

inhibitor loaded microrods ($4x10^3$, $8x10^3$, $12x10^3$) or blank microrods ($4x10^3$, $8x10^3$, $12x10^3$) for

24 hours. The cells were then lysed to collect genetic material for qPCR analysis.

*4.2.8 Animal model for post traumatic osteoarthritis*

A post-traumatic osteoarthritis model was obtained by placing the right lower leg of a 12-week-old C57BL6 mouse between the upper and lower loading cups of a Bose computer controlled electromagnetic load actuator and load cell. A single bout of tibial compression overload (TCO) at 14 N is then applied. The resistance to the load is actively monitored until ACL ruptures has been confirmed by the changes in resistance. Following ACL rupture, mice were injected with 50 µL of IGF-1R inhibitor-loaded microrods ($10^5$ microrods/mL) or saline under 3% isoflurane. The mice were sacrificed after 3 weeks and tissue sections were obtained for histological analysis.

*4.2.9 Fabrication and surface functionalization of HA microrods*

HMPP was dissolved in water at a 0.5% w/v concentration. The resulting solution was used to dissolve hyaluronic acid methacrylate at 100 mg/mL. Once fully dissolved, the solution was centrifuged at max speed for 5 minutes to remove impurities. A 15 µm thick layer of this solution was deposited onto a piranha cleaned silicon wafer and exposed through a photomask to a 365 nm UV light source using a Karl Suss Mask Aligner to crosslink the HA methacrylate in rod shapes (15 µm × 100 µm). The microrods were then gently scraped off the surface of the wafer using a cell scraper and collected into water, where uncrosslinked regions of HA methacrylate would fully dissolve. The microrods were passed through a 150 µm mesh filter to remove large particles and washed thoroughly by centrifugation. The microrods are sterilized with 70% ethanol and washed with sterile water.

HepIII and HepIII-FITC were conjugated to HA microrods by EDC/NHS coupling. Briefly, HA microrods were first washed into 50 mM 2-(N-morpholino)ethanesulfonic acid

(MES) buffer (pH 5.5) by centrifugation. To these microrods, EDC and NHSS were added to a final concentration of 1 mM and 2 mM, respectively, and allowed to react for 30 minutes. A stock of HepIII was prepared (2 mg/mL) in water and diluted to 0.5 mg/mL with 100 mM HEPES buffer (pH 8.0). This was added to the activated microrods in equal volume and allowed to react overnight. The reaction was purified by centrifugation and washing in water.

*4.2.10 Synthesis of magnetic nanoparticles with a silica-thiol coating*

Superparamagnetic iron oxide nanoparticles (SPIONs) were synthesized through coprecipitation of iron chloride salts under inert atmosphere. Briefly, 0.46 grams of iron(II) chloride tetrahydrate and 1.18 grams of iron(III) chloride hexahydrate were dissolved in 20 mL of deoxygenated water in a 100 mL round bottom flask. The solution was degassed further by nitrogen stream for 10 minutes and brought to 80 °C. 2.5 mL of 37% ammonium hydroxide was added under vigorous stirring, resulting in formation of a black precipitate of iron oxide. After an additional 30 minutes of stirring, a neodymium rare earth magnet was used to separate the nanoparticles from the supernatant. The nanoparticles were washed three times with deionized water and stored until further use.

SPIONs were coated with a silica-thiol shell by a modified Stober method[140]. 100 mg of SPIONs were diluted in 50 mL of water. Separately, 1 mL of ethanol was combined with 1.78 mL of TEOS and 1 mL of 2.4 mM hydrochloric acid and heated to 80 °C while stirring. The solution was cooled to room temperature and 0.59 mL of MPTMS was added and stirred for 20 minutes. The silane solution was added dropwise to the SPION solution under stirring over the course of 2 hours. Particles were separated by neodymium magnet and sequentially washed twice with water, twice with ethanol and twice with acetone before storage in neutral pH water.

*4.2.11 Fabrication of PEGDMA micromagnets*

Microrods were fabricated photolithographically as previously described[92,93,141]. To prepare the precursor solution, 1 mL of silica-thiol coated SPIONs in water were added to 9 mL of PEGDMA. Separately, 100 mg of HMPP was dissolved in 1 mL of NVP and added to the PEGDMA-SPION solution. A 15 µm thick layer of this solution was deposited onto a piranha-cleaned silicon wafer and exposed to 365 nm UV light through a chrome mask to crosslink the solution into rod shapes (15 µm x 100 µm). The microrods were developed in water for 3 minutes until the uncrosslinked hydrogel was dissolved. The wafer was then gently sprayed with isopropanol and dried with nitrogen gas. The microrods were collected of the wafer by soaking in ethanol followed by gentle scraping with a cell scraper. The crude solution was passed through a 150 µm mesh filter to remove large impurities. Magnetic microrods (micromagnets) were then concentrated using a neodymium magnet, resuspended in 70% ethanol and stored until further use.

*4.2.12 Culture of neonatal rat ventricular myocytes with magnetic microrods*

Ventricular cardiomyocytes (CMs) were isolated from 1-2 day old Sprague-Dawley rats as previously described[142]. CMs were seeded in the center portion of glass bottom dishes at a density of approximately 62,000 cells/cm$^2$ in previously described plating media[143]. The micromagnets were washed three times and resuspended in plating media prior to use. After 24 hours, dishes were washed with PBS to remove unattached cells, and 10$^4$ micromagnet were added to the entirety of the dish in plating media. CMs were cultured an additional 24-36 hours before beginning assays.

*4.2.13 Contractility measurements after application of load to cardiomyocytes*

A ring-shaped neodymium magnet with axial magnetism was placed above the culture dish to attract a micromagnet that is well-adhered to a CM and able to apply a transverse load. The magnet used in experiments had a 14.3 kg pull force, 3.81 cm diameter, 1.905 cm inner diameter, and 0.635 cm thickness (#RX8C4, KandJ Magnetics).

Line scan assays on spontaneously contracting CMs were carried out as previously described[135]. To provide clear markings for line scans, a line was chosen within the bounds of the cell along the direction of movement upon contraction. Line scan measurements were taken before and immediately after addition of a ring-shaped, axially-magnetized neodymium magnet on top of the dish designed to pull up on SPION microrods.

Displacement was measured on the kymographs as the distance between the resting and fully contracted positions. The spontaneous beat frequency was counted over a period of 30 seconds. The velocity of shortening of the contraction was determined by the amplitude ($\mu$m) for the linear portion of the rising phase divided by the time. The velocity of relaxation was similarly determined for the falling phase.

*4.2.14 Statistical analysis*

All values for continuous variables are listed as the mean $\pm$ one standard deviation unless otherwise indicated. Student's t-tests were performed to identify statistical differences between two groups. For experiments with three or more groups, one-way analysis of variance (ANOVA) was conducted, followed by Holm-Sidak correction for multiple comparisons to identify differences between groups.

## 4.3 Results

### 4.3.1 Alanine-loaded PEGDMA microrods for nutrient delivery

PEGDMA microrods were successfully fabricated in a range of polymer concentration without affecting reproducibility or microrod dimensions (Figure 4.1A). At lower concentrations of PEGDMA, the microrods were less rigid and often appeared to be arched. This is due to a reduced number of crosslinks that could be formed between the polymer chains, which resulted in a looser polymer network. The mesh size of the hydrogel also increases, allowing for more rapid diffusion of alanine in and out of the microrods. 20% microrods had the highest amounts of alanine released after 4 days while 80% microrods had the lowest amount eluted (Figure 4.1B). This difference is partially a result of higher loading of alanine into the 20% PEGDMA microrods, as alanine is more soluble in precursor solutions containing less PEGDMA. 20% PEGDMA microrods contained 600 mM alanine, while 50% and 80% PEGDMA microrods were loaded with 150 mM and 15 mM alanine, respectively. Since our goal is to deliver as much alanine to pancreatic islets as possible, we proceeded with 20% PEGDMA microrods for cell viability experiments (Figure 4.1C).

Islets were cultured at low density (20 islets/mL) and high density (1000 islet/mL) with and without alanine supplementation. Free alanine was previously shown to rescue the viability of nutrient-deprived primary islets *in vitro*[144]. Compared to low density islets, which exhibited 80% viability, high density islets had 65% viability (Figure 4.1D). Consistent with previous reports, addition of 10 mM alanine restored the viability of HD islets. When cultured with alanine-loaded microrods, there was a dose dependent increase in cell viability. Interestingly, this effect was much greater than the addition of free alanine at 10 mM concentration despite the microrods being predicted to elute significantly less alanine. One possibility is that the islets are

grown in great proximity to the microrods such that local concentrations of alanine are much higher. This suggests that co-delivery of drug-loaded microrods with islets may improve the success of cell replacement therapies by providing the transplanted cells with the required nutrients to survive the first few days before they are able to integrate with the host vasculature. In sum, our results illustrate the tunability and therapeutic potential of microrods for drug delivery and tissue engineering applications.

*4.3.2 Surface functionalization of PEGDMA microrods*

PEGDMA microrods were doped with AEMA to introduce primary amines to the hydrogel matrix. This provides a functional handle that can be used to attach carboxylic acid-containing compounds to the microrods via carbodiimide coupling (Figure 4.2A). We demonstrate that increasing amounts of AEMA linearly increases the amount of fluorescein-NHS that can be attached to the microrod surface (Figure 4.2B-C). DNA molecules can also be attached to the microrod surface, which can later coordinate with small molecules, nanoparticles or cells that present the complementary strand of DNA (Figure 4.3A). Despite improved conjugation at higher concentrations of AEMA, there is also more nonspecific adsorption of DNA oligos to blank microrods, likely due to charge interactions between primary amines and the DNA molecules (Figure 4.3B). This can also affect microrod-cell adhesions, suggesting that presentation of DNA may not be necessary to promote this interaction.

*4.3.3 Treatment of post-traumatic osteoarthritis by IGF-1R inhibitor loaded PEGDMA microrods*

PEGDMA microrods were also used as drug delivery devices for the treatment of post-

traumatic osteoarthritis. NVP-AEW541, a small molecule IGF-1R inhibitor, was incorporated into the 50% PEGDMA microrods by diffusion. The drug-loaded microrods were washed into PBS and samples were collected for over 1 week to assess release kinetics (Figure 4.4). There was initial burst release during the first day, followed by a linear phase between 2 and 10 days. When added to ATDC5 cells treated with IGF-1, there was reduced expression of MMP9 and MMP13 compared to cells without microrods (Figure 4.5). A mouse model of PTOA was generated via a single bout of tibial compression overload to create an ACL rupture (ACLR) (Figure 4.6A). After 24 hours, saline or NVP-AEW541 loaded microrods were injected into the injured knee. μCT indicated that ACLR decreased bone volume/total volume (BV/TV) in the subchondral bone, while microrod treatment prevented bone loss (Figure 4.6B). Similarly, microrod treatment blunted the increase in trabecular spacing caused by ACLR (Figure 4.6C). Immunohistochemistry (IHC) of tissues isolated 2 weeks after injection indicated that microrods remained in the knee capsule (Figure 4.7). ACLR induced phosphorylation of Erk in the vehicle treated knees, but the effect was blocked in the inhibitor treated knees, verifying inhibition of IGF-1 signaling (Figure 4.8A-C). Safranin O/fast green staining revealed erosion of the articular cartilage and formation of osteophytes in the ACLR knees treated with vehicle, but these effects were not observed in the control knees or injured knees treated with microrods (Figure 4.8D-F). Additionally, ACLR increased the number of proliferating cell nuclear antigen (PCNA) positive articular chondrocytes (Figure 4.8G-I) and MMP-13 production (Figure 4.8J-L) in the vehicle-treated injured knee, but these effects were blunted in the IGF-1R inhibitor-treated injured knee. VEGF production was also increased by ACLR, resulting in vessel formation within articular cartilage (as indicated by CD31) in the vehicle-treated injured knee, but these effects were blocked in the IGF-1R inhibitor-treated injured knee (Figure 4.9)

*4.3.4 Surface modification of HA microrods with proangiogenic peptides*

Surface functionalization of PEGDMA microrods was previous described in this chapter through incorporation of monomers containing primary amines. In contrast, HA microrods readily contain free carboxylic acid pendant groups which can be attached to primary amines via carbodiimide chemistry. We utilized EDC/NHS coupling to attach an amine-modified fluorescein, as well as a FITC-conjugated peptide, to HA microrods with minimal nonspecific adsorption (Figure 4.10). The peptide used, HepIII, is a fragment of collagen IV that has previously been demonstrated to promote neovascularization in a rat model of MI[136,145,146]. We grew human umbilical vein endothelial cells (HUVECs) with saline, bare HA microrods and HepIII functionalized microrods and quantified differences in proliferation rate. HA microrods, which were demonstrated in chapter 3 to increase fibroblast proliferation, had no effect on HUVEC proliferation (Figure 4.11). HUVECs cultured with HepIII modified microrods increased proliferation rate of HUVECs compared to control and bare HA microrods. This suggests that HepIII functionalized microrods may be able to promote tube formation *in vitro* and neovascularization *in vivo* while simultaneously reducing myofibroblast transformation. Animal experiments are currently underway to compare the effect of HepIII-functionalized HA microrods with bare HA microrods in a rat model of MI.

*4.3.5 Ferromagnetic microrods enable remote force manipulation of cardiomyocytes*

Previously, PEGDMA microrods containing ferromagnetic particles were fabricated for applications in 3D imaging[141]. We reconfigured these microdevices for manipulation of cardiac muscle cells in culture in order to study contractile function in a live cell modality. Magnetic nanoparticles were synthesized by coprecipitation of iron salts, followed by coating with a silica-

thiol shell (Figure 4.12A). This coating notably improved the stability of the nanoparticles in PEGDMA solution while also providing functional thiol groups for direct crosslinking of the particles to the polymer backbone by free radical addition. The ferromagnetic precursor solution was used to fabricate magnetic microrods by UV-photolithography (Figure 4.12B). These microrods were grown with cardiomyocytes and shown to be nontoxic as no cell death was observed during 4 days in culture. During this time, cardiomyocytes formed attachments to the microrods, enabling remote force loading using a neodymium magnet (Figure 4.12C). Line scans were taken before and after loading through the SPION microrod (Figure 4.13A-B). Kymographs showed an increase in contractile displacement, as well as permitting measurements for the contractile rising and relaxation falling phases. Changes in contractile metrics due to SPION microrod loading was studied in 30 cells. As determined by an increase in contractile displacement, success rate for eliciting a response through SPION microrod loading was approximately 66.6% (20 out of 30 cells), though all experiments were included in the analysis. Contractile displacement was significantly different in cells following loading, increasing from 1.88 $\mu$m to 2.17 $\mu$m (Figure 4.13C, $p = 0.028$). Beats frequency showed no difference before and after loading CMs, at 47.49 beats/minute and 46.69 beats/minute (Figure 4.13D). A change in contractile velocity was observed between the two conditions, increasing from 50.47 $\mu$m/s to 59.48 $\mu$m/s following loading (Figure 4.13E, $p = 0.046$). No difference was seen in relaxation velocity before and after loading CMs, at 21.18 $\mu$m/s and 22.75 $\mu$m/s (Figure 4.13F).

## 4.4 Discussion

While initially presented as a tissue engineering tool for delivery of mechanical cues, polymeric microrods can be adapted for a variety of therapeutic and research applications.

Microrods made of PEGDMA and HA can be used as drug carriers for drug delivery or as a secondary arm of therapy in addition to the previously described microtopography-based mechanisms[90,92,93,114]. Doroudian *et al* fabricated PEGDMA microrods that released mechano-growth factor (MGF) peptide over 14 days to stimulate migration of human mesenchymal stem cells (hMSCs) and protect neonatal rat ventricular myocytes (NRVMs) from hypoxia induced apoptosis[147]. PEGDMA microstructures were initially selected for these investigations because it is commercially available and its crosslinking density can be easily tuned, allowing for facile optimization of release kinetics. In contrast, HA microrods have a very large mesh network at all practical concentrations and are not suitable for delivery of small molecules, releasing them almost instantaneously. Instead, HA microrods can be used for delivery of larger biologics, relying on enzyme mediated degradation to slowly release proteins or peptides entrapped in the polymer matrix.

There are many benefits to using drug-loaded microrods to deliver therapeutic cargo. First, incorporation of small molecules into the PEGDMA matrix allows for tunable release kinetics. Increasing crosslinking density will lengthen the therapeutic timeframe while lower monomer concentrations may be ideal for when a high loading dose is required. This ease of tunability is crucial for using microrods in drug delivery applications because different diseases will require different drug release profiles. Further, encapsulation of the drug cargo within the polymer matrix may protect it from degradation until eluted from the microrod, enhancing the stability of the treatment. Interestingly, we also observed that the alanine-loaded microrods were able to improve cell viability to an equal or greater extent than high concentrations of free alanine. This suggests that there may be a local effect at play, where cells near the microrods will have access to high concentrations of drug. This is a major advantage in cases where it is only

necessary to have high local drug concentrations around a specific cell, such as in cell transplants, which would normally require much higher amounts of drug in a bolus dose.

There are, however, many questions left to be answered regarding the use of microrods as drug delivery devices. One concern is the unknown residence time of these microrods *in vivo*. Therapies requiring multiple injections may result in accumulation of microrods in the tissue due to negligible degradation. Incorporation of degradable functional groups into the polymer backbone is a potential solution to this issue and has been investigated in bulk hydrogels[148–152]. Further, we have extensively shown that bare microrods have anti-fibrotic properties, but their effects on beta cells, chondrocytes and stem cells requires more investigation. This information is crucial to decoupling the effects of the therapeutic and the microtopography for a more thorough understanding of the therapeutic mechanisms of action.

We attached a variety of molecules to the microrod surface to impart additional functionalities and further explore possible applications of this microrod technology. Presentation of DNA on cell surfaces has previously been demonstrated for temporary control of cell-cell interactions and microtissue organization[153–155]. Here, we show that this strategy can be adapted to transiently attach small molecules, proteins, nanoparticles, or cells onto the microrod via binding of complementary sequences. For a therapeutic application, beta cells can be transiently adhered to microrods loaded with alanine, creating a nutrient "backpack" to promote survival after transplantation. This approach can also be used for a variety of cell types and diseases, such as transplantation of iPSC-derived cardiomyocytes for heart failure therapy.

A range of ligands can also be conjugated to the microrod surface to activate signaling pathways upon binding and induce changes in cellular phenotype. HepIII, a collagen IV fragment, was previously shown to increase vessel density within the infarct area of a rat MI

model[136,145,146]. Here, we demonstrate the successful attachment of HepIII to HA microrods and cultured them with HUVECs to increase proliferation. This functionality can improve the overall therapeutic efficacy of HA microrod therapy after MI by stimulating formation of a vascular bed to support intrinsic myocardial repair mechanisms, in addition to the previously established antifibrotic effects.

Microrods are also a powerful tool for studying the effects of mechanical forces on cell behavior. Magnetic nanoparticles were previously incorporated into the microrod matrix and used to align the microrods in 3D for controlled growth of fibroblast and cardiomyocytes[156]. Additionally, magnetic microrods can also be used for applications in 3D imaging. In the present study, SPION loaded microrods are used as force actuators that are compatible with live-imaging to study the effect of discrete forces on cardiomyocyte response. A simple placement of an external neodymium magnet allowed accurate measurement of transverse loading on cardiac myocyte contractility using phase microscopy. The focal adhesions formed between the microrods and the CMs were strong enough to load and displace CMs when the external magnet was introduced. The displacement resulted in significant changes to the rate of rise in tension of the CMs.

Previous attempts have been made using magnetically actuated micropost surfaces to provide forces along the underlying surface of a cell, but these do not mimic the type of three-dimensional strain experienced by cells *in vivo*[157,158]. Additionally, many of these studies could not be imaged while the cell was mechanically deformed. Signals and remodeling were also studied after static strain or after bouts of exercise, but these were not live cell recordings[111,159–161]. In the current experimental arrangement, the microrods provide load mainly in a transverse direction across the myocyte. Changing the position of the external magnet to the side of the

culture dish would pull the SPION microrods along the longitudinal axis of the CM that could allow for sarcomere length dependent studies at the single cell level, potentially recapitulating the Frank-Starling law of the heart[162,163].

**4.5 Conclusion**

Collectively, these studies demonstrate the immense versatility of the microrod platform. We explored a wide range of chemical, biological and mechanical modifications that confer additional functionalities to the microrods, making them suitable for drug delivery, tissue engineering and basic research applications. While still in its infancy, this microstructural approach is a highly promising and fruitful technology for continued investigation, with many modifications and optimizations that have yet to be explored.
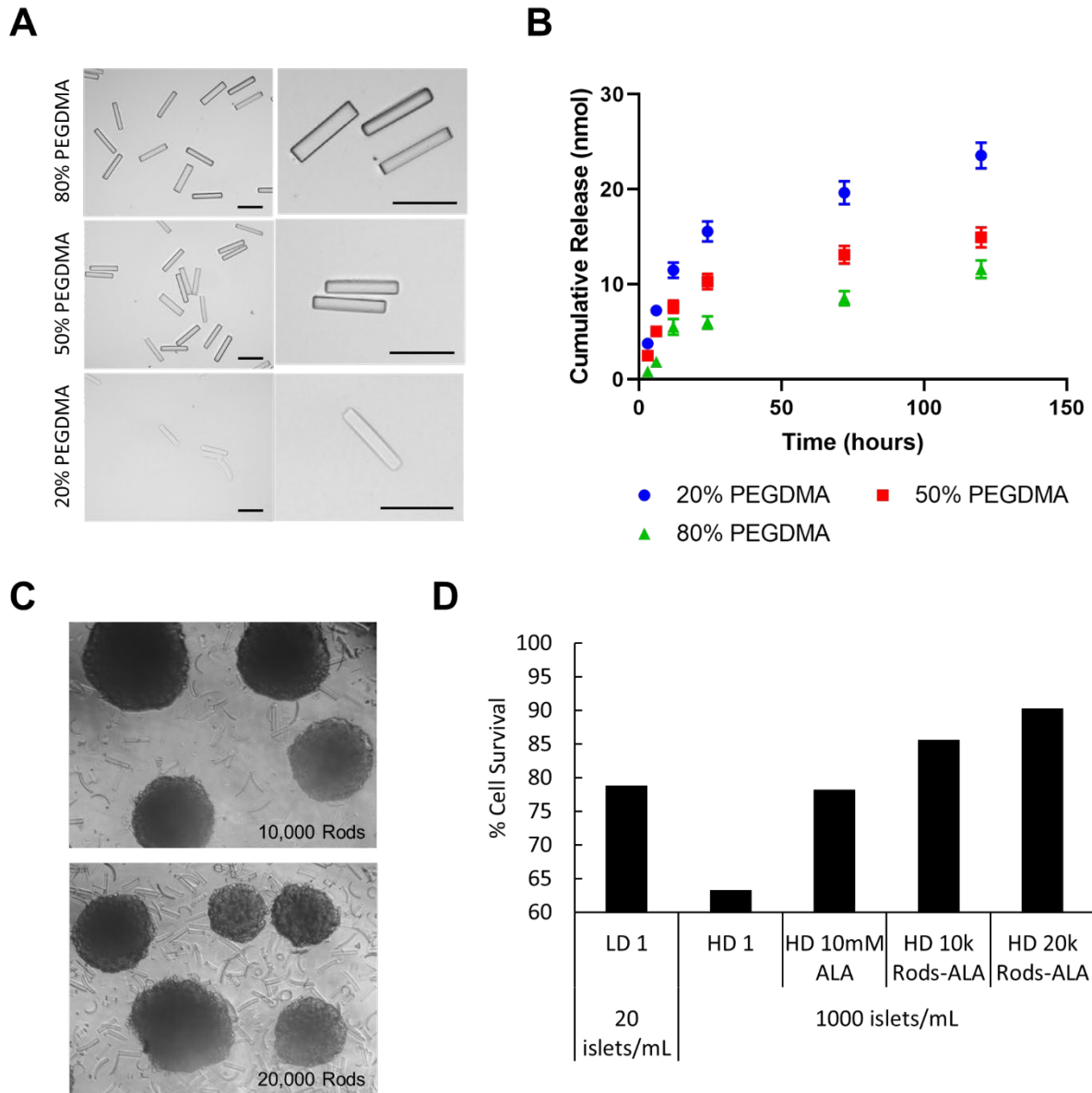
**Figure 4.1. Alanine-loaded microrods improve pancreatic islet survival.** (A) PEGDMA microrods were successfully fabricated in a range of monomer concentration. (B) Release of alanine from microrods with lower PEGDMA concentration had more rapid release of alanine over 4 days. (C) Brightfield image of primary pancreatic mouse islets cultured with 20% PEGDMA microrods containing alanine. (D) Islets cultured with alanine-loaded microrods had higher % survival compared to untreated islets, as well as compared to islets treated with free alanine.
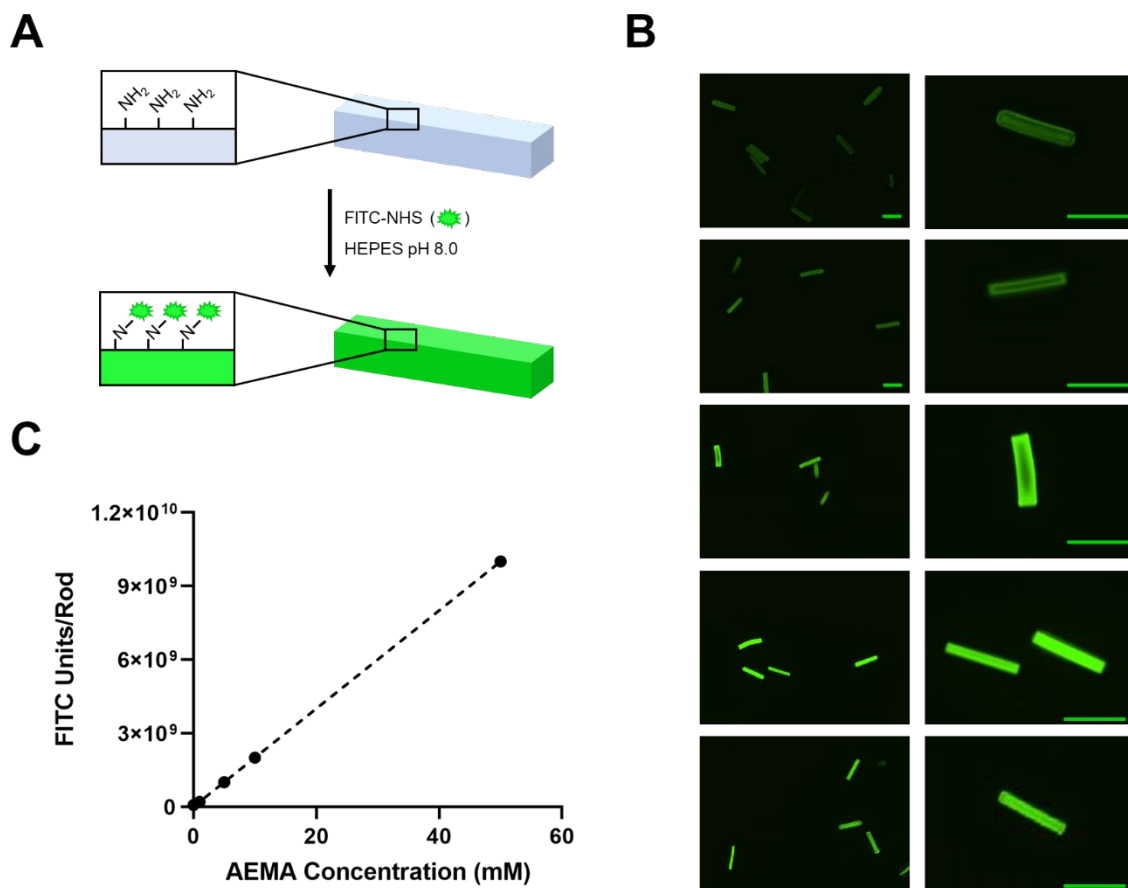
**Figure 4.2. Surface functionalization of PEGDMA microrods.** (A) PEGDMA microrods doped with primary amine groups can be functionalized with small molecules by EDC/NHS crosslinking. (B,C) Increasing the amount of primary amine groups result in increased fluorescence of microrods when conjugated with FITC-NHS.
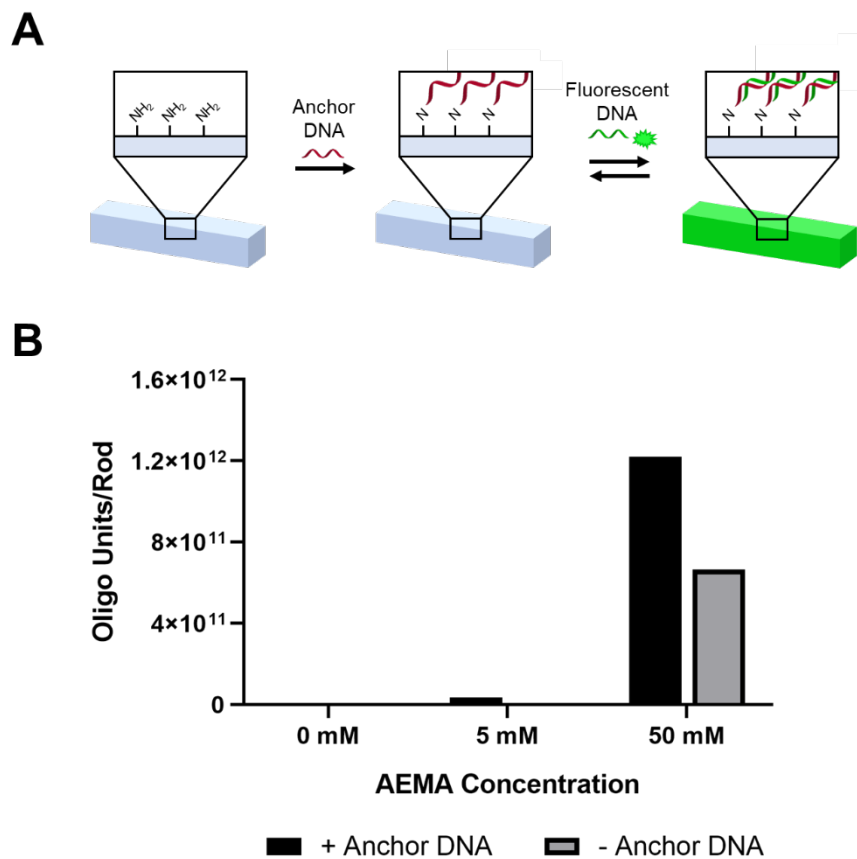
**Figure 4.3. Presentation of DNA oligos onto a microrod surface.** (A) Amine-doped PEGDMA microrods can be functionalized with DNA molecules and complexed with fluorescent oligos. (B) Increasing AEMA results in more DNA functionalization, as well as nonspecific adsorption, likely due to charge interactions.
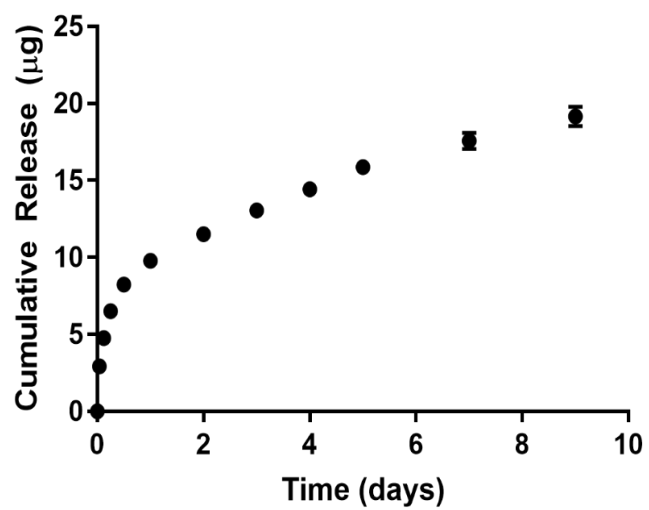
**Figure 4.4. NVP-AEW541 loaded microrods elute drug over 9 days.**
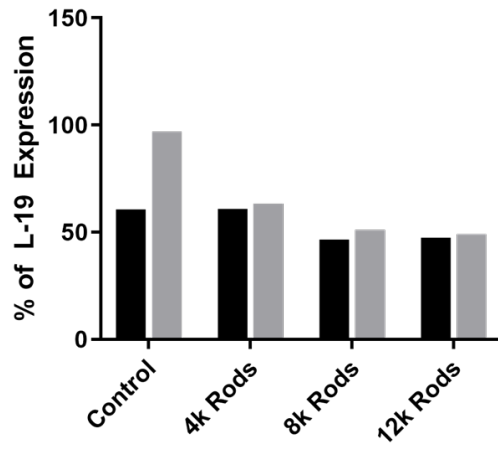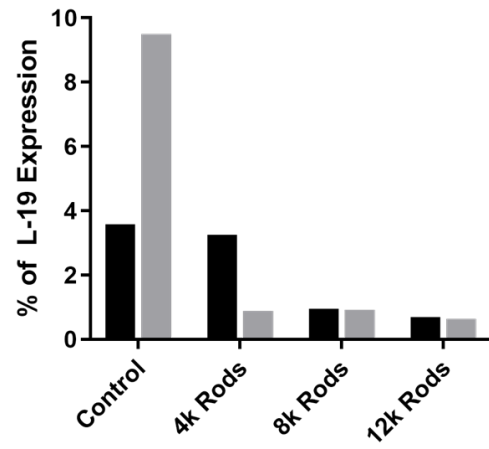
**Figure 4.5. NVP-AEW541 loaded microrods blunt the effect of IGF-1 treatment on matrix metalloproteinase expression *in vitro*.** (A) Incubation with NVP-AEW541 loaded PEGDMA microrods reduces expression of MMP9 and (B) MMP13 in ATDC5 cells treated with IGF-1 (black bar = control, grey bar = IGF-1 treated).
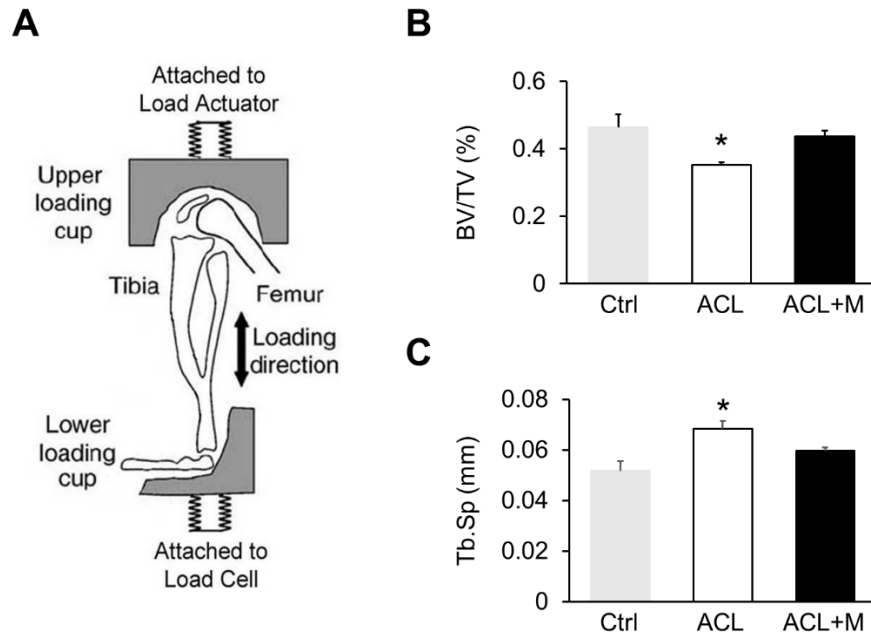
**Figure 4.6. Microrods loaded with IGF-1R inhibitor prevent subchondral bone loss during PTOA.** (A) Schematic of loading device for ACL rupture. The lower leg is placed between the upper and lower loading cups which are attached to the load actuator and load cell, respectively. A single 18N compression is applied. The resistance to the load is monitored by the attached computer, and the change in resistance documents the rupture of the ACL. This load did not result in fractures. (B) Vehicle or IGF-IR inhibitor loaded microrods were injected in to the injured knee one day after ACL rupture. The left knee of each mouse was used as a normal control. Samples were collected 2 weeks after injury. As determined by μCT, ACL rupture (ACL, open bars) decreased the trabecular bone volume (BV/TV) compared to control knees (Ctrl, grey bars), while microrods blunted these effects (ACL+M, solid bars). (C) ACL rupture increased trabecular space (Tb.Sp) compared to control. IGF-IR inhibitor loaded microrods (ACL/M, solid bars) attenuated this increase in Tb.Sp. Results are expressed as mean ± SD. *$p < 0.05$ vs. non-injured knee.
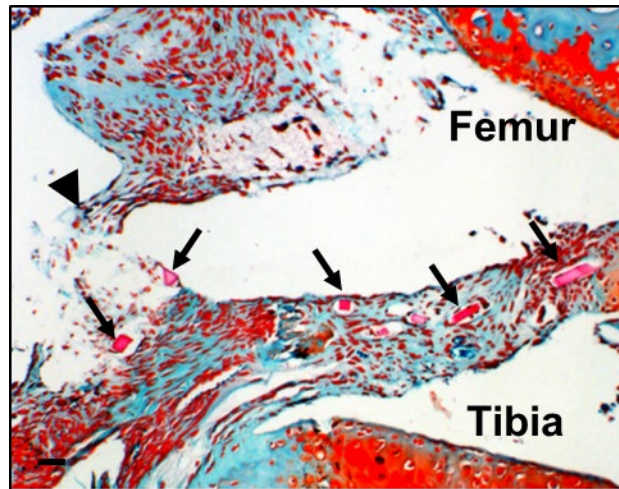
**Figure 4.7. IGF-1R inhibitor-loaded microrods remain in knee capsule two weeks after injection.** Large arrowhead indicates broken ACL and small arrows indicate microrods.
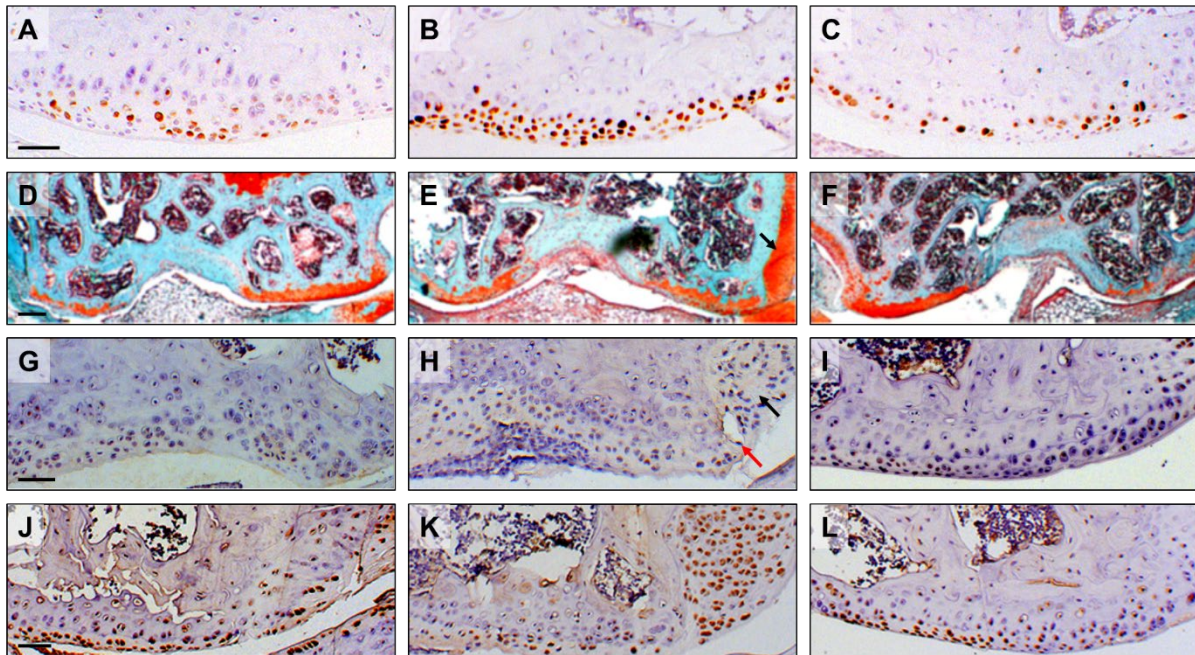
**Figure 4.8. IGF-1R inhibitor-loaded microrods blunt the effects induced by ACL rupture and attenuate OA development.** (A-C) Immunohistochemistry (IHC) staining using a phosphorylated ERK (pERK) antibody shows increased pERK expression (brown) in the articular chondrocytes of the injured knee (B) compared to the normal knee (A). These effects were blunted in the IGF-IR inhibitor treated knee (C). (D-F) Safranin O/fast green (S/F) staining shows that osteophyte was observed in the injured knee (E) but not in the normal (D) or microrod treated (F) knees. (G-I) IHC staining using a PCNA antibody showed that ACL rupture induces PCNA positive cells (brown) in the injured knee (H) compared to the non-injured knee (A), but these effects were not observed in the microrod treated knee (I). (J-L) ACL rupture (K) induces VEGF production when compared to the non-injured knee (J). IGF-1R inhibitor microrod treatment (L) blunted these effects. Black arrows indicate osteophyte, red arrow indicates abnormal vasculature in the cartilage. Scale bars = 50 µm (A-C), 200 µm (D-F) and 50 µm (G-L).
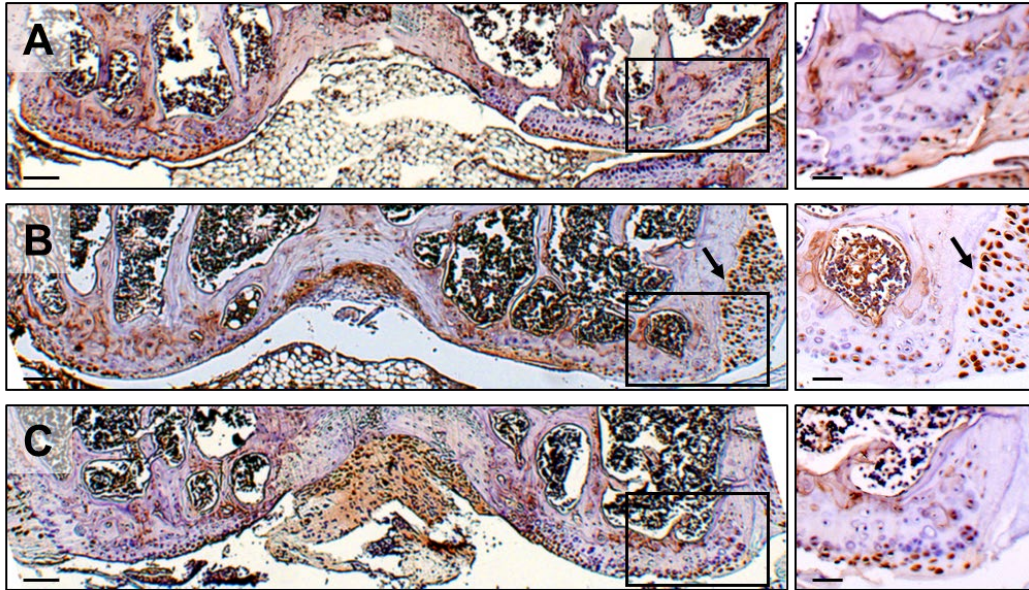
**Figure 4.9. IGF-1R inhibitor loaded microrods block MMP-13 production induced by ACL rupture.** Immunohistochemistry using an MMP-13 antibody showed that compared with the non-injured knee (A), injury (B) induced MMP-13 production (brown). Treatment of the injured knee with IGF-1R inhibitor-loaded microrods (C) blunts the production of MMP-13. Pictures to the right are high magnification (scale bars = 50 µm) of the framed areas of the pictures on the left (scale bars = 100 µm).
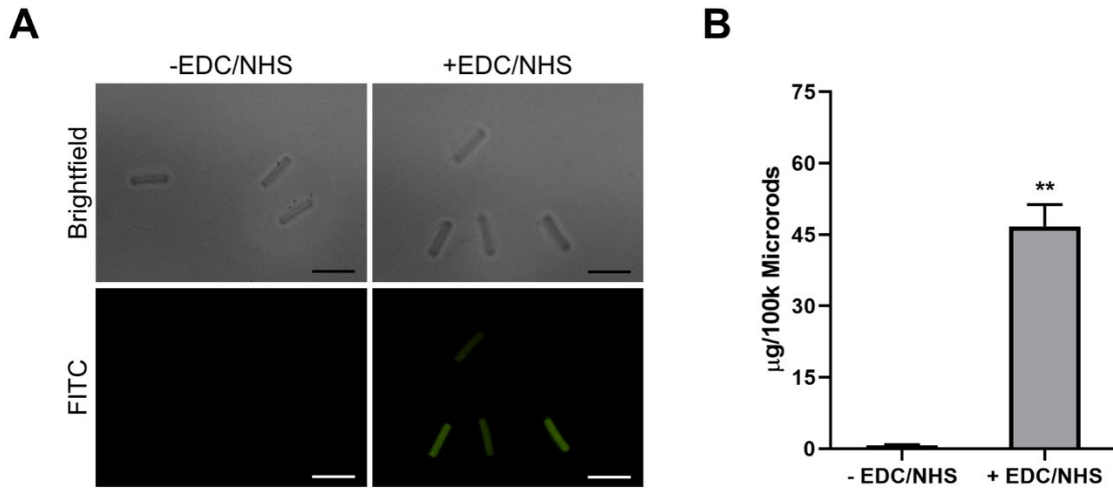
**Figure 4.10. HA microrods can be functionalized with amine-containing compounds via EDC/NHS coupling.** (A) Fluorescence imaging confirms successful conjugation of HA microrods with a fluorescein-labeled HepIII peptide via EDC/NHS carbodiimide coupling. (B) Spectroscopy was used to quantify the amount of HepIII-FITC on the microrods and indicate 46 µg of peptide per 100,000 microrods with limited nonspecific adsorption. Scale bars = 100 µm. The data are presented as the mean ± SD (n = 3). **$p < 0.01$.
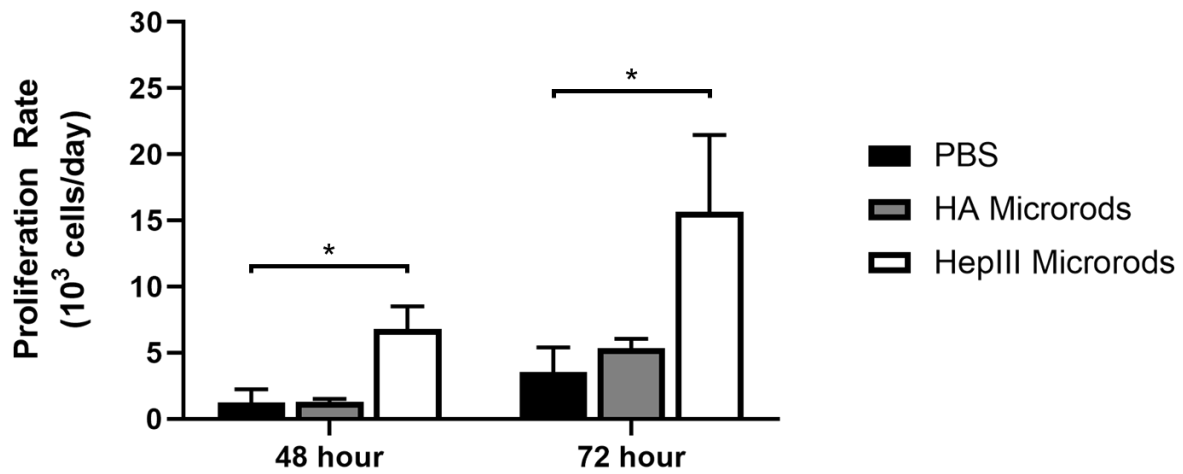
**Figure 4.11. HepIII microrods increase endothelial cell proliferation.** Treatment of human umbilical vein endothelial cells (HUVECs) with HepIII-conjugated HA microrods increases proliferation rates compared to bare HA microrods and PBS controls. The data are presented as the mean ± SD (n = 3). *$p < 0.05$.
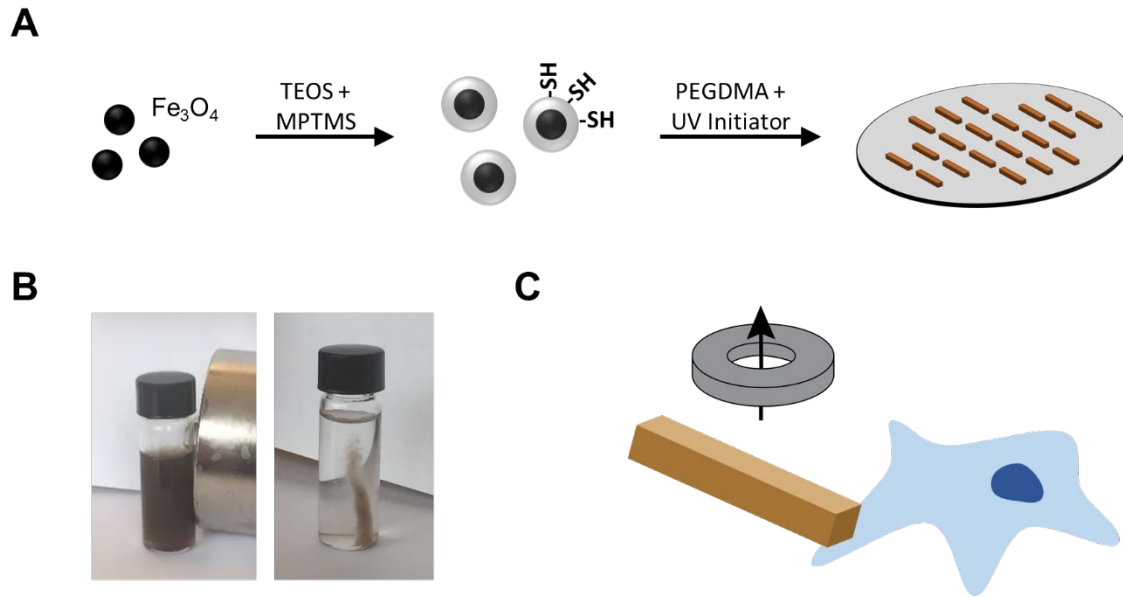
**Figure 4.12. Development of ferromagnetic microrods for remote application of force on cardiomyocytes.** (A) Fabrication scheme of PEGDMA microrods loaded with silica-thiol coated magnetic nanoparticles. (B) SPION-loaded microrods maintain magnetic properties and are rapidly attracted to a neodymium magnet. (C) Schematic of experimental setup, in which CMs are cultured with SPION microrods and form focal adhesions on them. An external neodymium magnet is then brought above the dish to provide load.
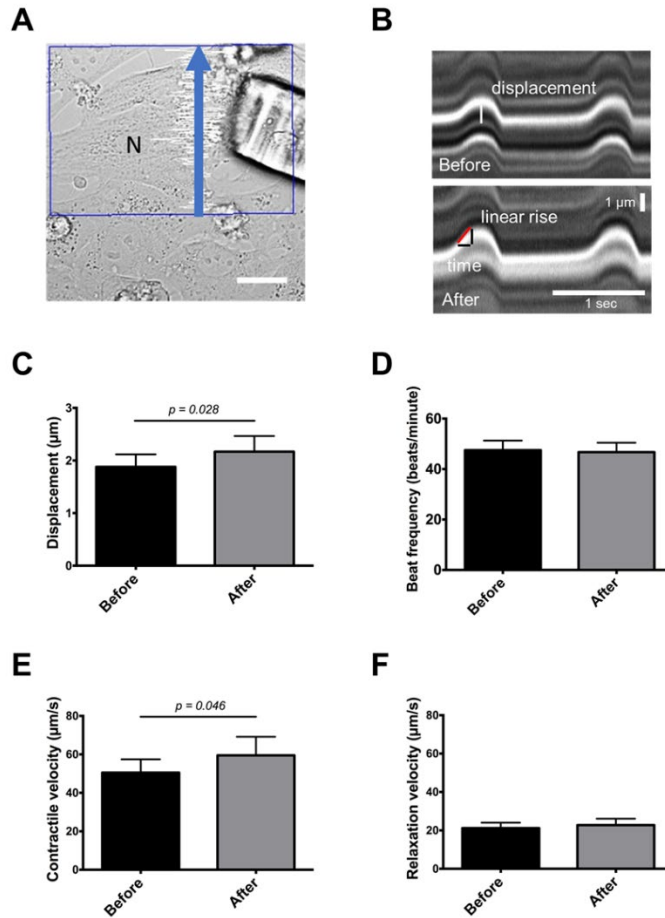
**Figure 4.13. Cardiomyocyte cultured with magnetic microrods to study the effect of acute load on contractility.** (A) Representative bright field image of line scan taken through cell interior. N indicates cell nucleus Scale bar: 20 µm. (B) Line scan kymographs before and after addition of magnet to provide load. Contractile velocities are obtained by measuring displacement and time of linear portion of contraction or relaxation and taking the slope. (C) Contractile displacement of myocytes increases with load, $p = 0.028$. (D) Beat frequency is unchanged following load from SPION microrods. (E) Contractile velocity increases with load, p $= 0.046$. (F) Relaxation velocity is unchanged following load from SPION microrods.

## Chapter 5 – Near-Infrared Hydrogel-Nanosensor Composites for Real-Time Detection of Blood Analytes

### 5.1. Introduction

Chronic cardiovascular diseases are a daunting health challenge, costing the American healthcare system over 30 billion dollars annually[164]. This spending is expected to dramatically increase each year due to an aging patient population that continues to grow larger in the wake of improved diagnosis and treatment in the acute setting[1]. Currently, management of chronic heart failure (CHF) consists of periodic visits to primary care or specialized centers to obtain snapshots of disease progression followed by appropriate treatment[2,165]. Despite attentive care, an alarming number of adverse events still occur between visits, resulting in hospitalization of the patient, reduced quality of life and increased healthcare costs[166–169]. It is therefore necessary to change our approach in treating chronic diseases and develop technologies that allow patients to continuously monitor and control the progression of their disease state.

In recent decades, there has been a push towards point-of-care testing for the self-management chronic diseases[165,170]. The ability to monitor total health state from the bedside would inform patients and healthcare providers with greater frequency on the progression of chronic disease or the onset of additional comorbidities. This allows for more timely interventions and improve patient quality of life. It has been demonstrated that several blood metabolites correlate with unfavorable cardiovascular outcomes[171–173]. For example, high levels of lactate are indicative of low oxidative capacity and is predictive of CHF and HF-related mortality[171,174]. Similarly, monitoring of blood glucose levels facilitate the detection of diabetes, a major risk factor and comorbidity of cardiovascular disease[175–178]. The ability to accurately and

frequently measure these metabolites would help notify individuals when expert interventions are required, limiting the incidence of adverse events and improving patient quality of life.

The most common of point-of-care tests are finger-prick blood tests, which utilize discrete blood samples that are analyzed *ex vivo* by a portable device. This allows patients to obtain a snapshot of their current health state in the convenience and comforts of their own home. Low patient compliance, however, significantly impairs the effectiveness of these tests, demanding alternatives for self-management[179,180]. Alternatively, implantable electrochemical sensors have been developed to continuously monitor blood analyte levels through percutaneous electrodes[181–184]. Benefits of this strategy include reduced responsibility from the patient to conduct discrete blood tests and the ability to detect major fluctuations throughout the day. However, the insertion of these electrodes causes undesired tissue trauma and carry a high risk for infection, resulting in a substantial immune response and eventual fibrotic encapsulation. In turn, the sensitivity of these sensors are severely compromised after implantation and require recalibration or replacement every 7-10 days[184–186]. Despite significant efforts to improve the sensitivity and durability of implantable sensors, there are few effective options for long-term, continuous metabolite sensing today.

The development of a fully implantable, tissue-integrating sensor that can rapidly and reliably detect substrates in the physiological range would be a major advancement for continuous monitoring of chronic cardiovascular diseases. Here, we present the development of three hydrogel-nanoparticle composite sensors for the detection of oxygen, glucose and lactate. The use of a composite material allows us to independently optimize the mechanical and biochemical properties of the scaffold component and the responsiveness and specificity of the sensor component to create an optimal subcutaneous sensor. Furthermore, incorporation of

multiple nanoparticle sensors within one tissue-integrating hydrogel scaffold would generate a simple, personalized device for total health sensing.

## 5.2 Materials and Methods

### 5.2.1 Materials

Tetraethylene glycol dimethacrylate (TEGDMA), 2-hydroxyethyl methacrylate (HEMA), N-dimethylacrylamide (DMA), poly(methyl methacrylate) (PMMA) microparticles, 1-Hydroxybenzotriazole hydrate (HOBt), ascorbate oxidase (AOx), o-dianisidine dihydrochloride, sodium L-lactate, horseradish peroxidase, sodium alginate, calcium carbonate, and glucono-δ-lactone were purchased from Sigma Aldrich (St. Louis, MO). 1-ethyl-3-(3-dimethylaminopropyl)carbodiimide hydrochloride (EDC), N-hydroxysulfosuccinimide (NHSS), and L-ascorbic acid were purchased from Thermo-Fisher Scientific (Waltham, MA). Calcium chloride was purchased from bioWORLD (Dublin, OH). 100 nm amine-terminated silica nanoparticles were purchased from Nanocomposix, Inc (San Diego, CA). Lactate oxidase from Aerococcis viridans was purchased from A.G. Scientific (San Diego, CA). VA044 thermal initiator was purchased from Wako Chemicals USA, Inc (Richmond, VA). Acid-terminated palladium benzoporphyrin (Pd-BP), palladium benzoporphyrin methacrylate (Pd-BPMA), viologen boronic acid, and IRDye680 were donated by PROFUSA, Inc (South San Francisco, CA).

### 5.2.2 Preparation of microporous HEMA:DMA hydrogels

Hydrogel scaffolds were fabricated utilizing previously described techniques[187,188]. Briefly, a 3 mm teflon spacer was sandwiched between two glass slides and used as a mold for

hydrogel polymerization. A prepolymer solution consisting of 50% monomer solution, 20% dimethyl sulfoxide (DMSO), 2% TEGDMA crosslinker, VA044 thermal initiator (10 mg/mL), and water/nanoparticle solution/free dye solution was prepared. The monomer solutions consisted of either pure HEMA or a 50:50 mixture of HEMA and DMA. The prepolymer solution was injected into the prepared mold and incubated at 37 °C for at least 4 hours. The crosslinked hydrogel was gently removed from the mold and allowed to swell in PBS.

In order to form hydrogel scaffolds with interconnected micropores, PMMA microparticles were packed into the assembly described above and sintered to form a bead cake. Prepolymer solution was then injected and crosslinked as described above to form a hydrogel with interconnected PMMA beads. The PMMA beads were leached out by incubation in acetone, leaving behind a hydrogel with interconnected micropores.


### 5.2.3 Synthesis and characterization of oxygen nanosensors

An acid-terminated palladium (II) benzoporphyrin (Pd-BP acid) was custom synthesized and donated by PROFUSA, Inc. Pd-BP acid was attached to amine-terminated silica nanoparticles using EDC/HOBt crosslinking chemistry. Pd-BP acid was dissolved in DMSO at 2 mM and activated with EDC and HOBt for 30 minutes. The final concentrations were 1 mM, 10 mM and 20 mM, respectively. This solution was added to aminated silica nanoparticles in 100 mM 4-(2-hydroxyethyl)-1-piperazineethanesulfonic acid (HEPES) buffer (pH 8.0) and allowed to react overnight on a shaker. Conjugated nanoparticles were centrifuged, washed thrice into HEPES buffer and stored until further use.

Absorbance spectra were obtained in order to account for any shifts in peak excitation and emission wavelengths of the Pd-BP dye after conjugation to a nanoparticle. Pd-BP

nanoparticles were assayed for oxygen sensitivity by fluorescence in a plate reader format. Solutions of free Pd-BP, blank nanoparticles, and Pd-BP nanoparticles were degassed by $N_2$ stream for 15 minutes. The fluorescence of the nanoparticles was then measured over the course of 30 minutes to monitor reoxygenation due to gas exchange at the liquid-air interface. The solutions were then mixed thoroughly for complete reoxygenation to serve as baseline.

*5.2.4 Ratiometric oxygen sensor calibrations*

A methacrylate oxygen-insensitive dye (Cy5.5-MA) was prepared by reacting Cy5.5-NHS with AEMA in equimolar concentrations. HEMA hydrogel sensors containing Cy5.5-MA and a methacrylated Pd-BP (Pd-BPMA) were fabricated as described above. Hydrogels were placed in a 96-well plate with 200 µL of PBS and degassed for 15 minutes by nitrogen stream. The fluorescence of all dyes was measured over the course of 30 minutes to monitor reoxygenation (excitation = 630 nm, emission = 665 nm, 800 nm). A calibrated NeoFox oxygen probe (Ocean Optics, Largo, FL) was used to track oxygen content of PBS that had also been deoxygenated for 15 minutes by $N_2$ stream. Oxygen %/time was then compared to fluorescence/time to obtain a relationship curve for fluorescence and oxygen %.

An ascorbate oxidase assay was developed to slowly deplete solution of oxygen for calibrations in a controlled manner. For these assays, hydrogel sensors containing Pd-BPMA and an oxygen-insensitive reference dye were donated by PROFUSA, Inc. A solution of ascorbate oxidase (2.5 U/mL) was prepared in PBS and allowed to equilibrate for 20 minutes. For plate reader calibrations, hydrogels were placed into a 96-well plate with 200 µL of ascorbate oxidase. To this, 10 µL of 10 mM ascorbate was added and the fluorescence was measured for 30 minutes (excitation = 630 nm, emission = 700 nm, 800 nm). Addition of ascorbate was repeated until 0%

oxygen was achieved. Similarly, a NeoFox oxygen probe was used to measure equilibrium oxygen content in solutions of ascorbate oxidase for each addition of ascorbate. These calibrations were repeated with an *in vivo* imaging system (IVIS) to measure oxygen tension in mice.

*5.2.5 Synthesis of glucose nanosensors*

Glucose nanosensors were synthesized using procedures similar to the oxygen sensors. An acid-terminated near-infrared wavelength fluorescent dye (IRDye680) and a viologen-based boronic acid (VBA) quencher were custom synthesized and donated by PROFUSA, Inc. Both compounds were attached to aminated silica nanoparticles in a range of concentrations using EDC/NHSS crosslinking chemistry. VBA and IRDye680 were dissolved in DMSO in a range of concentrations and activated with a 10-fold excess of EDC and 20-fold excess of NHSS for 30 minutes. This solution was added to 10 mg/mL of aminated silica nanoparticles in 100 mM HEPES buffer (pH 8.0) and allowed to react overnight on a shaker. Conjugated nanoparticles were centrifuged, washed thrice into HEPES buffer and stored until further use. Absorbance spectra were obtained in order to account for any shifts in peak excitation and emission wavelengths of IRDye680 after conjugation to a nanoparticle.

*5.2.6 Quantification of IRDye680 and VBA on glucose nanosensors*

IRDye680 content on nanoparticles was quantified by absorbance at 680nm and subtracting baseline absorbance from blank nanoparticles. A degradation assay was developed to determine VBA content on the nanosensors. 200 µL of glucose nanosensors and standard solutions of free VBA were treated with 100 µL of 50 mM sodium hydroxide and incubated for 5

minutes. The absorbance of the glucose nanosensor sample was measured at 405 nm and compared to the standard curve to calculate VBA content.

*5.2.7 Characterization of glucose sensitivity*

To test the optical response of the nanosensors, samples were placed in a 96-well plate and challenged with gradual additions of glucose. Fluorescence was measured (excitation = 680 nm, emission = 710 nm) for 10 minutes before any glucose addition to obtain baseline fluorescence readings. The concentration of glucose was increased to 50 mg/dL by addition of concentrated glucose (20 mg/mL) and the fluorescence was measured continuously until the signal stabilized. This process was repeated several times to reach 100 mg/dL, 200 mg/dL and 600 mg/dL. Glucose sensitivity was reported as a ratio of intensity at 200 mg/dL over intensity at 50 mg/dL.

*5.2.8 Determination of lactate oxidase activity*

Lactate oxidase activity was measured by a coupled enzyme assay. A reaction mix containing o-dianisidine dihydrochloride (0.0535 mg/mL), sodium L-lactate (16.611 mg/mL), and horseradish peroxidase (2 U/mL) were prepared in 80 mM sodium acetate buffer, pH 5.1. 200 µL of this reaction mix was placed into a 96-well plate and lactate oxidase or lactate oxidase nanoparticles (LoxNP) were added. Immediately after addition, absorbance readings were taken at 449 nm to track the rate of conversion of lactate to pyruvate. The slope during the first minute was calculated and presented as OD/min as a measure of lactate oxidase activity.

*5.2.9 Assessment of lactate oxidase stability*

Lactate oxidase stability and activity was assessed after being exposed to a variety of environmental conditions, including heat, UV exposure, pH levels to optimize chemical conjugation strategy. After these challenges, samples were assessed for enzymatic activity per the o-dianisidine assay mentioned above (5.2.8).

*5.2.10 Synthesis of lactate nanosensors*

Lactate nanosensors were prepared in a similar fashion to the previous sensors mentioned. Lactate oxidase in a range of concentration (5 U/mL to 1000 U/mL) was activated with a 10-fold molar excess of EDC and 20-fold molar excess of NHSS in phosphate buffer (pH 5.5) for 30 minutes. To this solution, a 1.5-fold volume of 10 mg/mL amine-terminated silica nanoparticles in 100 mM HEPES buffer (pH 11) containing 0.1% polyethylene glycol (MW = 5000 Da) was added and reacted for 4 hours while stirring. The particles were washed eight times by centrifugation to eliminate all traces of free lactate oxidase.

*5.2.11 Preparation of alginate hydrogels*

Alginate hydrogels were prepared using an internal gelation method[189,190]. Alginate was dissolved in water at a 4% w/v concentration and filtered through a 0.22 µm filter. Lactate oxidase nanoparticles and calcium carbonate were added to the filtered alginate solution and thoroughly mixed. Glucono-δ-lactone was then added and thoroughly mixed to initiate gelation. The final concentrations of lactate oxidase nanoparticles, calcium carbonate and glucono-δ-lactone in the hydrogel solution were 8 mg/mL, 4.2 mg/mL, and 7.5 mg/mL, respectively. The final concentration of alginate was 1.5% w/v or 2.0 w/v depending on the formulation. The

solution was immediately injected into a mold to crosslink overnight. Once fully set, the alginate hydrogel was removed from the mold and stored in TRIS buffer containing 90 mg/mL calcium chloride.

## 5.3 Results

### 5.3.1 Synthesis of oxygen nanosensors

A carboxylic acid-modified palladium benzoporphyrin was activated with EDC/HOBt and successfully attached to amine-coated silica nanoparticles (Figure 5.1A-C). Nanoparticles that were reacted with EDC/HOBt activated Pd-BP were bright green after purification, compared to nanoparticles that were reacted with control Pd-BP. Absorbance spectra of conjugated nanoparticles, control particles and free Pd-BP showed that the absorbance peaks of Pd-BP did not shift upon conjugation to a particle (Figure 5.1D). Pd-BP nanoparticles also maintained an emission peak at 800 nm (Figure 5.1E). A solution of Pd-BP nanoparticles was degassed by nitrogen stream and allowed to reoxygenate over time. There was a 10-fold difference in fluorescence between nanoparticles in the absence of $O_2$ compared to fully oxygenated particles (Figure 5.1F).

### 5.3.2 Calibration of ratiometric fluorescence to oxygen tension

In order to optimize this system for detection of oxygen *in vivo*, a ratiometric sensor was developed using a methacrylated Pd-BP (Pd-BPMA) and a methacrylated Cy5.5 (Cy5.5-MA). HEMA hydrogels were fabricated in a range of Pd-BPMA concentrations and a fixed concentration of Cy5.5-MA. For all hydrogel samples, there was no response of the Cy5.5 dye (665 nm) to variations in oxygen (Figure 5.2A). Increasing Pd-BPMA concentration increased

$O_2$ response, with less improvement after 1 mM Pd-BPMA. The fluorescence ratio ($I_{800}/I_{665}$) was calculated and plotted over time to be used as a measure of oxygen level (Figure 5.2B). Additionally, the reoxygenation kinetics of an oxygen-depleted solution was measured over time using a NeoFox oxygen probe (Figure 5.2C). This was used to calibrate the oxygen sensors and give a relationship between fluorescence ratio, which can be measured *in vivo*, to oxygen tension (Figure 5.2D).

An ascorbate oxidase-based assay was developed to more precisely modulate oxygen levels for $O_2$ sensor calibrations. In the presence of ascorbate oxidase, ascorbate is converted to dehydroascorbate, consuming oxygen in the process. We found that adding specific concentrations of ascorbate to an ascorbate oxidase solution quickly depletes oxygen in the solution, with increasing ascorbate leading to linear decreases in oxygen tension to a minimum of 0% at 0.75 mM ascorbate (Figure 5.3A). Similarly, addition of ascorbate increases fluorescence of Pd-BPMA as a result of reduced oxygen tension (Figure 5.3B-C). These relationships were used to calibrate the fluorescence ratio of hydrogel sensors to oxygen tension (Figure 5.3D). We repeated these calibrations within an *in vitro imaging system* (IVIS) and were able to determine oxygen tension within free hydrogel sensors, sensors encapsulated in polycaprolactone thin-film devices, and sensors implanted into a mouse (Figure 5.4D).

### 5.3.3 Optimization of glucose sensitivity

A two-component sensing system consisting of a near infrared dye (IRDye680) and a boronic acid-based viologen (VBA) quencher was used to detect glucose (Figure 5.5A). In the absence of glucose, there is electrostatic association of VBA with the fluorescent dye, leading to reduced fluorescence. Upon binding to glucose, VBA is neutralized and has diminished

quenching efficiency. It has been previously established that boronic acid positioning plays an important role in determining quenching activity. It is therefore likely that total IRDye680 and VBA concentration, and thereby molecular proximity, would be critical for optimization of a glucose sensor. We fabricated HEMA-based hydrogels containing IRDye680 and VBA in a fixed 1:10 ratio at varying total concentrations to examine this dependence (Figure 5.5B). When challenged with glucose, hydrogel sensors with higher concentrations of IRDye680 and VBA have better sensitivity to glucose, while those with less than 5 mM VBA and 0.5 mM IRDye680 have limited sensitivity that was more similar to drift than stepwise increases in fluorescence (Figure 5.5B-C).

This high proximity position of dye and quencher can be reproduced on a nanoparticle, where each component is concentrated on the nanoparticle surface. We first developed an assay to determine the concentration of VBA, which is normally colorless, on a nanoparticle. Upon treatment with a strong base, the viologen degrades and obtains an absorbance peak at 400 nm (Figure 5.6A). A range of concentrations of VBA were treated with increasing concentrations of sodium hydroxide to determine the degradation kinetics of VBA. Interesting, we find that 100 mM NaOH is required to fully degrade VBA in the detectable range (Figure 5.6B). We compared standard curves generated with each concentration of NaOH and found that 10 mM NaOH to 100 mM NaOH generated the same standard curves (Figure 5.6C).

We proceeded to conjugate these components onto an amine-coated silica nanoparticle. Both VBA and IRDye680 were activated by EDC/NHS chemistry and attached to the nanoparticle under basic conditions (Figure 5.7A). The ratio of VBA and IRDye680 was varied from 1:15 to 1:50 to optimize glucose sensitivity of the nanoparticles. When VBA and IRDye680 were not treated with EDC/NHS, silica nanoparticles exhibited no conjugation of quencher and

dye compared to particles treated with EDC/NHS activated VBA and IRDye680, which appeared bright blue (Figure 5.7B). When challenged with glucose, all nanoparticles exhibited sensitivity to glucose, with 1:50 ratio of IRDye680:VBA having the greatest glucose modulation (Figure 5.7C-D). When these sensors were treated with control solution, sensors with a 1:15 ratio of IRDye680:VBA had some drift in fluorescence while 1:50 sensors had little to no response.

*5.3.4 Lactate sensitivity and stability*

An enzyme-based nanoparticle was developed for the detection of lactate. Compared to analyte-responsive fluorophores, enzyme-based sensing systems benefit from short response times and high specificity. However, enzymes can be more sensitive to degradation or denaturing, leading to reduced activity. Our goal was to attach lactate oxidase onto a silica nanoparticle by formation of a stable amide bond. We initially tested the sensitivity of lactate oxidase to a variety of buffer conditions that were used during EDC/NHS coupling. Lactate oxidase maintained its activity in MES and HEPES buffer relative to activity in PBS (Figure 5.8A). Interesting, lactate oxidase had slightly higher activity in HEPES buffer ($p < 0.001$), suggesting that storage in HEPES buffer may provide additional stability.

We then investigated the conjugation of lactate oxidase through formation of amide bonds via lysine residues. Sodium acetate was activated by EDC/NHSS and reacted with lactate oxidase. Interestingly, conjugation via lysine residues leads to significantly reduced activity compared to both control (MES buffer) and sodium acetate without EDC/NHSS activation (Figure 5.8B, $p < 0.0001$). This suggests that conjugation by lysines causes occupation of key reactive sites on the enzyme, leading to significantly reduced enzymatic activity. Therefore, we investigated conjugation of lactate oxidase to amine-coated silica nanoparticles by the C-

terminus of the enzyme. Lactate oxidase was activated with EDC/NHSS and attached to silica nanoparticles as previously described (Figure 5.9A). The lactate oxidase nanoparticle sensors maintained enzymatic activity, suggesting limited loss in activity after conjugation (Figure 5.9B). In order to maximize enzymatic activity of the nanosensors, silica nanoparticles were conjugated with increasing concentrations of lactate oxidase. Enzymatic activity of nanoparticles was maximized (2000 mU/mg of particle) in reactions with 500 U/mL of EDC/NHSS activated lactate oxidase, after which there was a decline due to aggregation of enzyme (Figure 5.9C). Stability of these nanosensors at physiological temperature was assessed and found to be unaffected (Figure 5.9D). By contrast, challenge of nanosensors with lactate resulted in gradual reduction of activity, likely due to the production of reactive peroxidases during the enzymatic conversion of lactate to pyruvate (Figure 5.9E).

These nanoparticles were incorporated into a HEMA scaffold and found to have significantly reduced enzymatic activity (Figure 5.10A). While lactate oxidase is stable to UV exposure and incubation at 37C, the presence of thermal and photo-initiators that result in the formation of free radicals causes substantial degradation of the enzyme (Figure 5.10B-C).

Milder crosslinking strategies were therefore to incorporate lactate nanosensors into a hydrogel scaffold without affecting enzymatic activity. Alginate hydrogel scaffolds were fabricated by an internal gelation method using calcium carbonate and a weak acid[189,190]. This enabled incorporation of nanosensors, as well as other sensing chemistries, without the use of free radicals or covalent crosslinking (Figure 5.10D). When challenged with lactate, 1.5% w/v and 2.0% w/v alginate hydrogels containing lactate oxidase nanosensors had considerable enzymatic activity, as compared to those made with HEMA via free radical polymerization (Figure 5.10E)

**5.4 Discussion**

The ability to continuously detect blood oxygen, glucose and lactate presents exciting opportunities for heart failure diagnosis. Although a variety of specific biomarkers are associated with myocardial infarction and heart failure, these substrates typically consist of proteins or peptides that are difficult to continuously measure via an implantable sensor[25,173,191,192]. By contrast, detection of small molecule targets, such as oxygen, glucose and lactate, have been frequently reported in the form of optical and electrochemical sensors, and can be applied towards risk assessment of cardiovascular disease[171,174,193–195]. For example, high blood lactate indicate hypoxemia and can warn patients and medical providers of compromised cardiac function and output[174]. Elevated blood glucose levels can inform patients on the development of diabetes, a major comorbidity of cardiovascular disease that increases the risk for MI[175–178]. Conversely, individuals who have experienced MI are also more likely to develop diabetes, which exacerbates the progression and risk for total heart failure[196,197].

In this study, we describe the synthesis of three novel nanoparticle sensors for continuous measurement of blood oxygen, glucose and lactate levels. These sensors utilize near-infrared dyes in combination with a range of chemistries to modulate fluorescence as a function of metabolite concentration. Additionally, these dyes can be excited and detected through skin with minimal loss in signal due to the exceptional penetration depth of near infrared wavelengths.

The ideal optical sensor would rapidly integrate with the host tissue, avoid fibrotic encapsulation, and maintain sensitivity and specificity for extended periods of time. Our nanoparticle sensors were embedded into a microporous hydrogel scaffold that supports ingrowth of blood vessels to promote intimate integration with the host tissue. This design reduces the diffusion distance between the vasculature and the nanosensors for rapid detection.

Additionally, our nanosensors were independently optimized for sensitivity without affecting the properties of the hydrogel matrix. This separation of function also enables incorporation of multiple different types of nanosensors within the same scaffold for simultaneous monitoring of multiple analytes.

For the oxygen sensor, we utilized a fluorescent palladium benzoporphyrin (Pd-BP) that coordinates with oxygen similarly to the heme functional group (Figure 5.1A). The emission intensity of the phosphor is very low at ambient conditions as a result of collisional quenching. When oxygen levels are low, there is less energy transfer from the phosphor to the oxygen molecules, leading to increased fluorescence intensities[187,188,198]. This relationship between fluorescence and oxygen concentration can be described by the following Stern-Volmer equation, where $I^0_f$ is the intensity without quencher, $I_f$ is the intensity in the presence of quencher with quencher coefficient $k_q$, $\tau_0$ is the emissive lifetime and $[Q]$ is the concentration of the quencher.

$$\frac{I^0_f}{I_f} = 1 + k_q \tau_0 \cdot [Q]$$

Methacrylated derivatives of this benzoporphyrin have been utilized in combination with hydrogel scaffolds to fabricate oxygen sensors for continuous tracking of tissue hypoxia in rats, pigs and humans[198,199]. These sensors utilize emission lifetimes as an output for oxygen tension. In our study, we utilize fluorescence intensity as an output, requiring additional calibrations. As shown in Figure 5.2B, we demonstrate that responsiveness of Pd-BP fluorescence to time after deoxygenation, which can be correlated to absolute oxygen levels. This was assessed more rigorously through an ascorbate oxidase assay that was used to control oxygen tension of a solution (Figure 5.3). In order to use these sensors *in vivo,* it is necessary to develop a dual-dye system to account for fluctuations in baseline fluorescence. An oxygen-insensitive near-IR dye

was utilized for ratiometric sensing. A ratio between the oxygen-sensitive dye and the oxygen-insensitive dye could be used and prevent ambiguities due to loss in signal due to tissue depth. We demonstrate that fluorescence ratio can also be used as a measure of oxygen tension *in vitro* as well as *in vivo* (Figure 5.2D, Figure 5.3D, Figure 5.4).

We conjugated an acid-modified derivative of this benzoporpyrin to silica nanoparticles in order to generate oxygen nanosensors that have a ten-fold increase in fluorescence at low oxygen compared to ambient conditions. This is comparable to the aforementioned homogeneous sensors where the dye was directly conjugated to the polymer matrix[199]. With these nanosensors, we are therefore able to maintain the oxygen sensitivity while being able to change the polymer matrix to accommodate other functionalities – such as reducing crosslinking density to enable more rapid diffusion of analytes.

The ability to localize the sensing chemistries onto a nanoparticle surface was tantamount for the development of a glucose sensor. This novel optical sensing chemistry utilized a near-IR wavelength dye that is modulated by a nearby quencher molecule. This quencher molecule is responsive to glucose due to the inclusion of two boronic acid groups, which upon binding to diols, gains additional negative charges that significantly hinders electron transfer between the quencher and fluorophore[200–205]. It has been previously demonstrated that positioning of the boronic acid moiety plays a large role in glucose modulation[206]. Therefore, it is likely that the sensitivity of a hydrogel scaffold consisting of these components would heavily depend on proximity of the dye and quencher.

We hypothesized that the distance between the fluorophore and the quencher could be tuned by adjusting their total concentrations within the hydrogel scaffold, allowing for optimization of sensitivity. This was confirmed through generation of a library of sensors with

both IRDye680 and VBA covalently incorporated into the hydrogel network. Our results indicated that with a fixed ratio of dye to quencher, increasing their absolute concentrations, and by extension, their proximity to each other, improved the sensitivity of these hydrogel scaffolds to glucose. Conjugation of these moieties to a nanoparticle surface allowed us to significantly reduce the distance between dye and quencher and increase sensitivity. We further optimized these glucose nanosensors by optimizing the ratio of dye to quencher. With minimal amounts of quencher, there is increased fluorescent signal due to limited fluorescence inhibition. However, there is also reduced glucose modulation due to a reduction of glucose responsive groups. By increasing the amount of quencher, there was greater glucose modulation that was accompanied by overall lower fluorescence values. This trend continued up to a 1:50 ratio of dye to quencher. For all ratios, there were no additional increases in fluorescence after 600 mg/dL of glucose, which exceeds the physiologically relevant range.

The final sensor utilized lactate oxidase for the detection of lactate. Enzymes are highly specific and have rapid response times, which are ideal for incorporation into a hydrogel sensor. While a multitude of enzyme-based sensors have been developed, the variable sensitivity and stability of different enzymes necessitate thorough optimization for applications in sensing. Glucose oxidase has been widely used for optical and electrochemical glucose monitoring with great success[207–209]. In contrast, most lactate oxidase-based biosensors have limited operational lifetimes and efficacy due to the marked instability of the enzyme[210–212]. We conducted several assays to assess the stability of lactate oxidase for fabrication of lactate nanosensors. Enzymes are particularly sensitive to pH, which spans a large range during our EDC/NHS coupling strategy. Lactate oxidase was stable when incubated in buffers ranging from pH 5.5 to pH 8.0. Activity assays were performed with small quantities of lactate oxidase in concentrated buffers

to account for the variable activity of lactate oxidase at different pH values.

A major concern when immobilizing proteins onto surfaces is the potential to occupy key reactive sites on the protein. For example, immobilization of antibodies must be done away from the antigen binding site to retain affinity and specificity. When conjugated to a carboxylic-acid terminated nanoparticle, there was limited lactate oxidase activity, suggesting that specific lysine groups make up the enzyme active site. This was confirmed by conjugation of lactate oxidase to acetate-NHSS esters (Figure 5.8). Conjugation of the enzymes carboxylic acid groups to an amine-terminated nanoparticle results in retention of enzymatic activity (Figure 5.9). Unsurprisingly, this activity was increased when more enzyme was attached to the nanoparticle surface. After 500 U/mL of lactate oxidase, there was significant aggregation of the enzyme leading to reduced nanosensor yield, and activity. These nanosensors retained their activity when incubated at physiological temperature, but were sensitivity to lactate challenge. We suspect that this is due to the accumulation of hydrogen peroxides that are a byproduct of the conversion of lactate to pyruvate. Clearance of peroxides in vivo is anticipated to alleviate this problem.

The sensitivity of proteins to UV irradiation and free radicals is also well appreciated. Our previous nanosensors were embedded into a poly(hydroxyethyl methacrylate) (pHEMA) hydrogel scaffold, which were crosslinked by free radical polymerization. While stable to UV exposure and physiological temperatures, the incorporation of free-radical initiators severely diminished the activity of lactate oxidase, necessitating alternative hydrogel scaffolds or crosslinking strategies. Alginate scaffolds can be gently crosslinked with calcium ions while preserving enzyme activity. Typically, alginate is immersed in a solution of calcium chloride to immediately crosslink the polymer. Here, we utilized an internal gelation method that is compatible with molds. This method utilizes water-insoluble calcium carbonate in combination

with a weak acid to slowly release calcium into the polymer network. This slowly gels the alginate and can be used in combination with microbeads to generate microporous hydrogel scaffolds. The activity of the lactate oxidase was maintained after incorporation into the.

In order to use these for sensing *in vivo*, we propose to combine this enzyme-based sensor with the palladium benzoporphyrin described above. Conversion of lactate to pyruvate is accompanied by consumption of oxygen, which can therefore be used as a proxy for lactate concentration. Additional optimization is required to incorporate Pd-BP into the alginate scaffold, which lacks functional handles that can be crosslinked to the acid groups. The oxygen nanosensors described in this chapter can be incorporated with the lactate nanosensors to introduce both functionalities into the alginate matrix. The addition of catalase to consume evolved hydrogen peroxide and prevent enzyme degradation can also be investigated to improve the sensitivity and stability.

As a whole, these studies show that optical nanosensors are a promising for the detection of blood analytes relevant to cardiovascular disease. Despite successes in the optimization of sensitivity, the long-term stabilities of these materials have yet to be assessed. For clinically relevant applications, it is necessary to have continuous sensors that can accurately measure and report blood analyte levels over a long period of time without loss in sensitivity or signal. When activity is lost or the sensor is deemed inaccurate, additional sensors can be implanted to replace them as these hydrogel sensors are biocompatible and can be fabricated with a small form factor. However, to accomplish the practical goal of reducing the frequency of doctor visits and putting the power of diagnostics into the patients' hands, a lifespan of over three months is ideal. Additionally, while outside the scope of the present study, the development of instrumentation that can noninvasively excite and detect fluorescent signals from the nanosensors is also

necessary. A patient would ideally be able to read their blood analyte levels and be alerted to seek medical attention whenever certain threshold levels or patterns arise. By addressing these requirements, we can make self-diagnosis of heart disease more approachable to patients and empower them to take control of their disease state.

## 5.5 Conclusion

Nanoparticle sensors capable of detecting oxygen, glucose and lactate were synthesized and incorporated into tissue-integrating hydrogel scaffolds to form a composite implantable sensor. These materials utilize three unique sensing chemistries that are in the near-infrared spectrum and can therefore be detected through tissue. We systematically optimized each nanoparticle sensor to detect their respective analytes in the physiological range. Of these, the oxygen sensors were most rigorously calibrated for *in vivo* applications via ratiometric sensing. Future work will focus on calibrating the more complex glucose and lactate sensors for *in vivo* sensing, combining several nanoparticles sensors for multi-analyte sensing, and developing an optical reader to continuously excite and detect the fluorescent signals. Together, these advancements facilitate the development of personalized sensors capable of continuously monitoring crucial blood analytes, thereby enhancing our ability to manage chronic diseases.
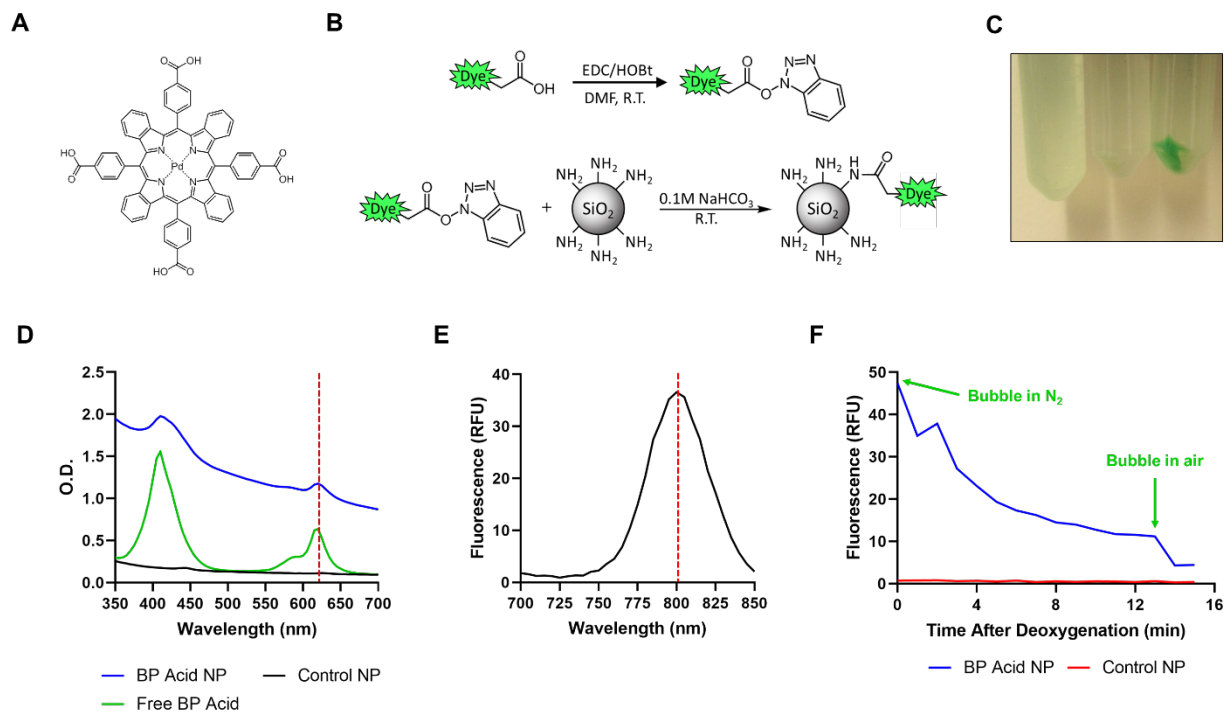
**Figure 5.1. Conjugation of silica nanoparticles with oxygen sensitive Pd-BP**. (A) Chemical structure of Pd-BP. (B) Pd-BP was conjugated to silica nanoparticles by EDC/HOBt activation of the carboxylic acid groups followed by reaction with primary amines on the silica nanoparticle surface in basic conditions. (C) Images of purified silica nanoparticles show that treatment of Pd-BP with EDC/HOBt results in successful conjugation to nanoparticles (right), compared to nanoparticles reacted with Pd-BP without EDC/HOBt (middle) and blank nanoparticles (left). (D) Pd-BP nanoparticles retain absorption peaks of free Pd-BP and have a distinguishable emission peak at 800nm (E). (F) Pd-BP nanoparticles show sensitivity to oxygenation with ~10-fold difference in fluorescence (ex/em = 625/800).
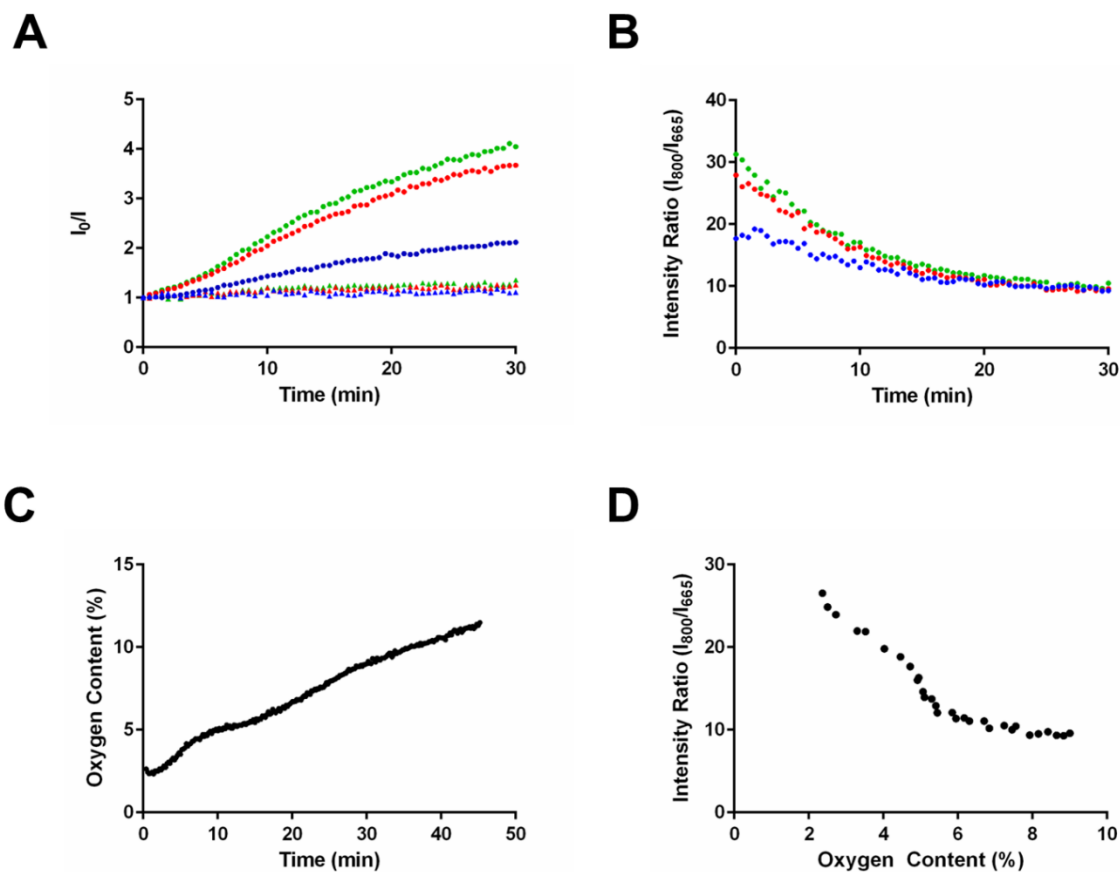
**Figure 5.2. Oxygen and fluorescence calibrations for ratiometric sensing.** (A) Hydrogel sensors were fabricated with varying concentrations of $O_2$ sensitive Pd-BP and 0.008 mM of Cy5.5, an $O_2$ insensitive reference dye. Stern-volmer plots indicate dramatic loss in oxygen modulation below 1 mM (circles = 800 nm emission, triangles = 665 nm emission, blue = 0.75 mM Pd-BP, red = 1 mM Pd-BP, green = 2 mM Pd-BP). (B) Intensity ratio of $O_2$ sensitive Pd-BP to $O_2$ insensitive Cy5.5 during oxygen modulation. (C) A NeoFox probe was used to measure the static reoxygenation kinetics of a deoxygenated solution over time. (D) Correlation curve of intensity ratio to oxygen content.
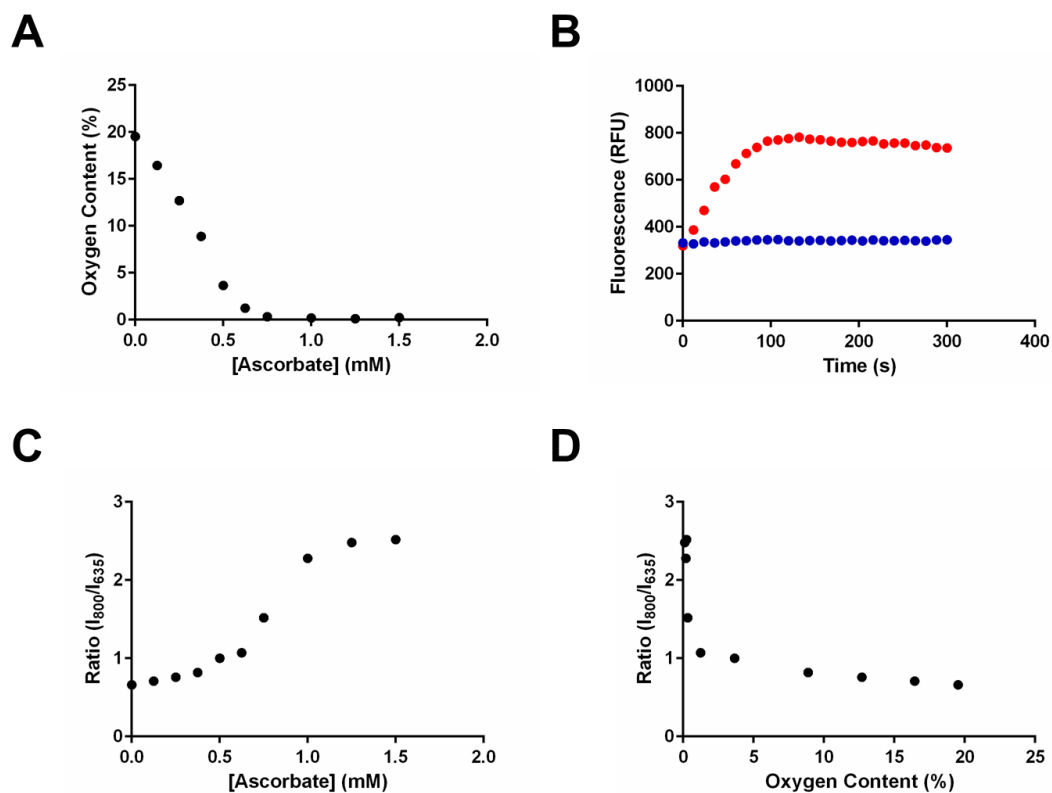
**Figure 5.3. Development of ascorbate oxidase-based oxygen modulation.** (A) Equilibrium oxygen content after addition of varying concentrations of ascorbate. (B) Representative fluorescence response of hydrogel sensors containing Pd-BP (emission = 800 nm) and a reference dye (emission = 700 nm) after addition of 1 mM ascorbate. (C) Equilibrium fluorescence ratio of Pd-BP to reference dye after addition of ascorbate. (D) Calibration of fluorescence ratio to oxygen content.
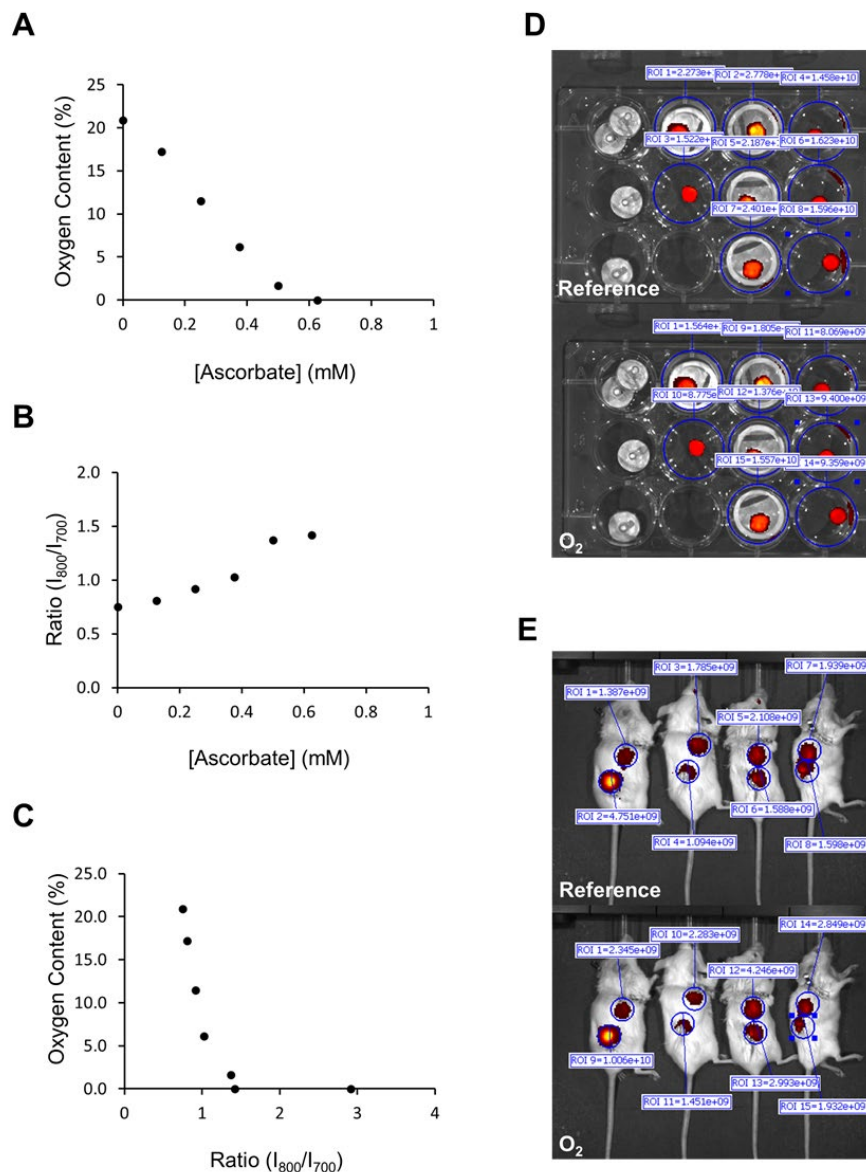
**Figure 5.4.** *In vivo* **imaging of ratiometric optical sensors predict oxygen tension.** (A) Equilibrium oxygen content after addition of varying concentrations of ascorbate. (B) Equilibrium fluorescence ratio of Pd-BP to reference dye after addition of ascorbate as measured by an *in vivo* imaging system (IVIS). (D) Representative IVIS images of free hydrogel sensors and sensors encapsulated within a polycaprolactone thin film device. (E) Representative IVIS images of hydrogel sensors implanted into a mouse model.
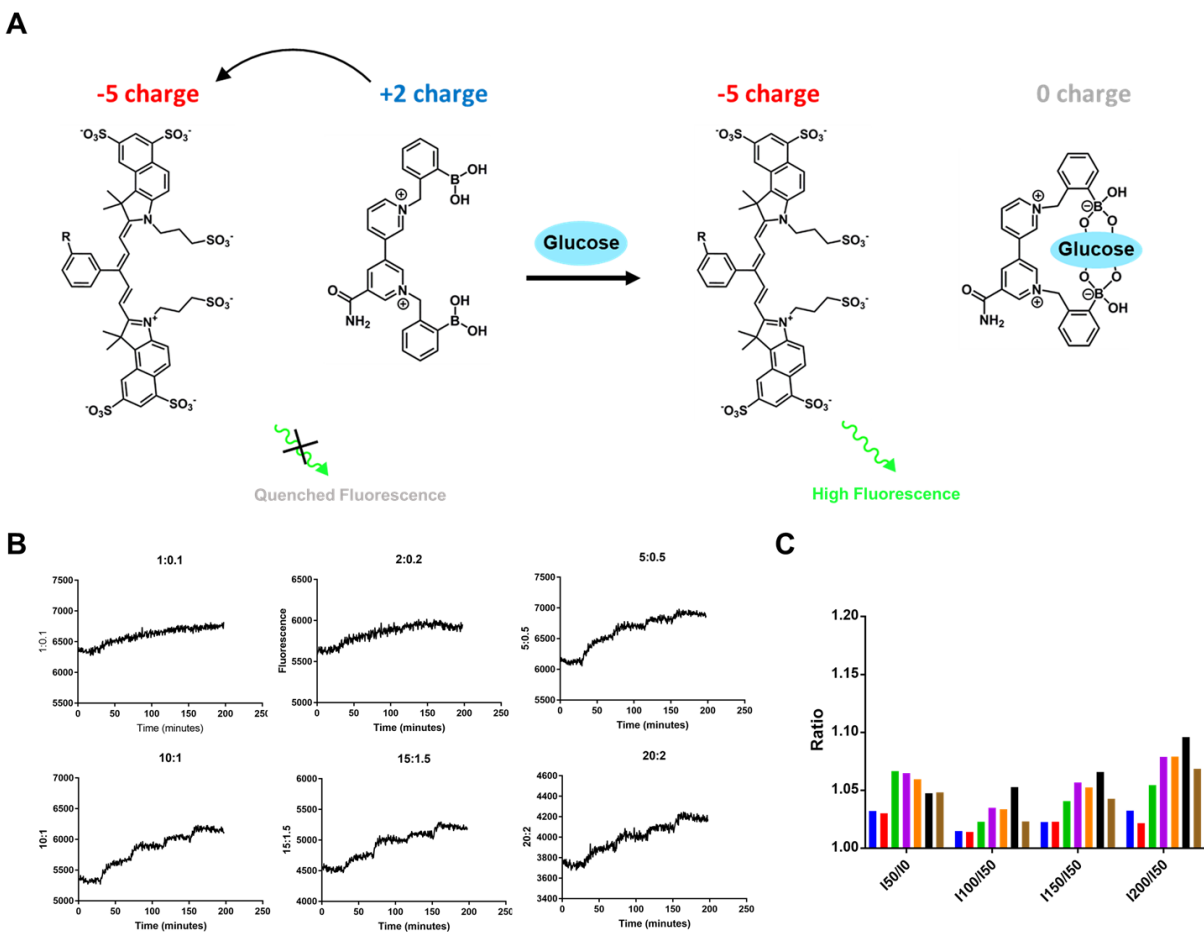
**Figure 5.5. Two-component glucose sensing chemistry is concentration dependent.** (A) A boronic-acid modified viologen molecule binds glucose to modulate the fluorescence of a near-infrared dye (B) HEMA hydrogels containing IRDye680 and VBA at a fixed 10:1 ratio in a range of concentrations were challenged with additions of glucose (C) Intensity ratios of glucose sensitive hydrogels reveal that high total concentrations of IRDye680 and VBA are required for optimal sensing.
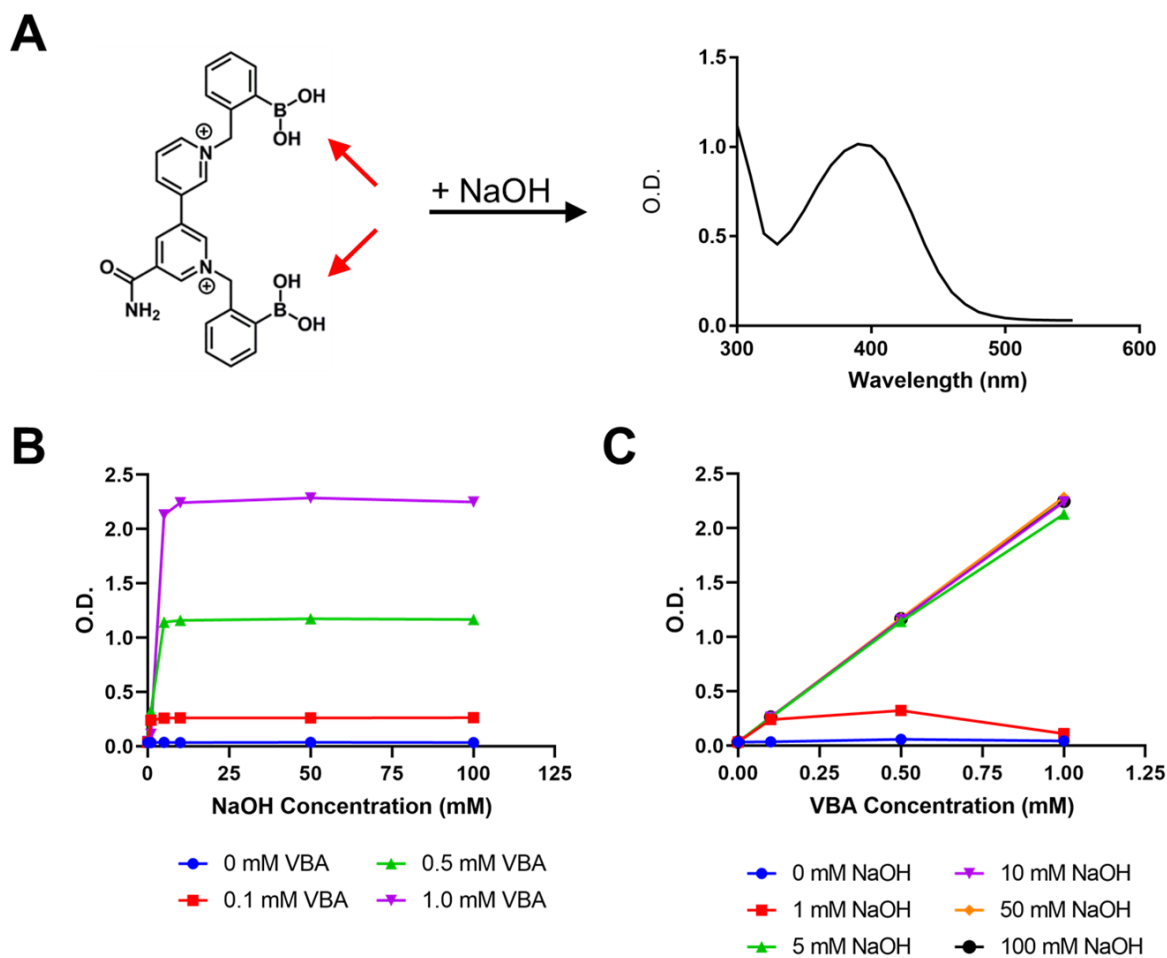
**Figure 5.6. Detection of VBA quencher on glucose nanosensors.** (A) Treatment of VBA with NaOH results in the appearance of an absorbance peak at 400 nm. (B) Absorbance of VBA at all concentrations plateau after treatment with 10 mM NaOH. (C) Standard curves of VBA are indistinguishable after treatment with at least 10 mM NaOH.
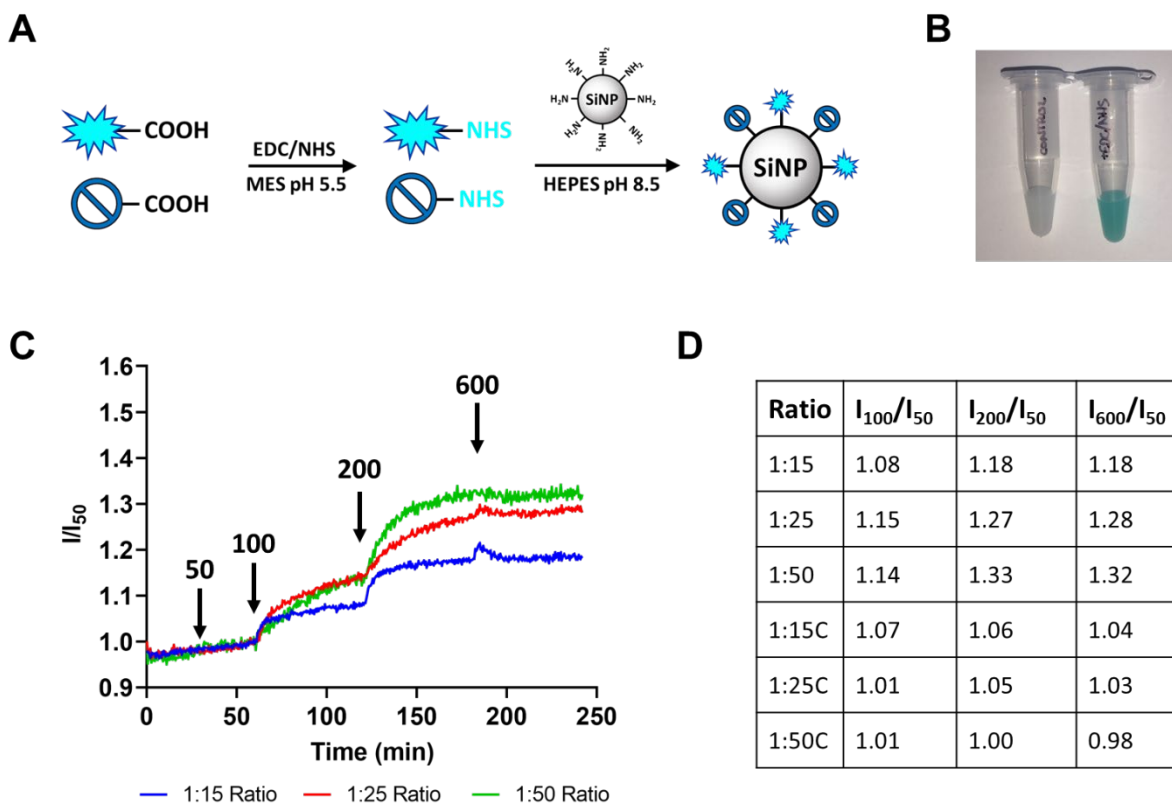
**Figure 5.7. Optimization of glucose nanosensor fabrication.** (A) Synthesis scheme of glucose nanosensors with IRDye680 and VBA quencher. (B) Comparison of silica nanoparticles reacted with IRDye680/VBA (left) and EDC/NHS activated IRDye680/VBA (right). (C) Glucose modulation of glucose nanosensors containing a range of IRDye680:VBA ratios show that higher ratios provide better modulation. (D) Table of intensity ratios for particles treated with glucose and particles treated with control (saline) indicate that higher IRDye680:VBA ratios have better modulation within physiological ranges ($I_{200}/I_{50}$) and limited drift in fluorescence upon addition of saline.
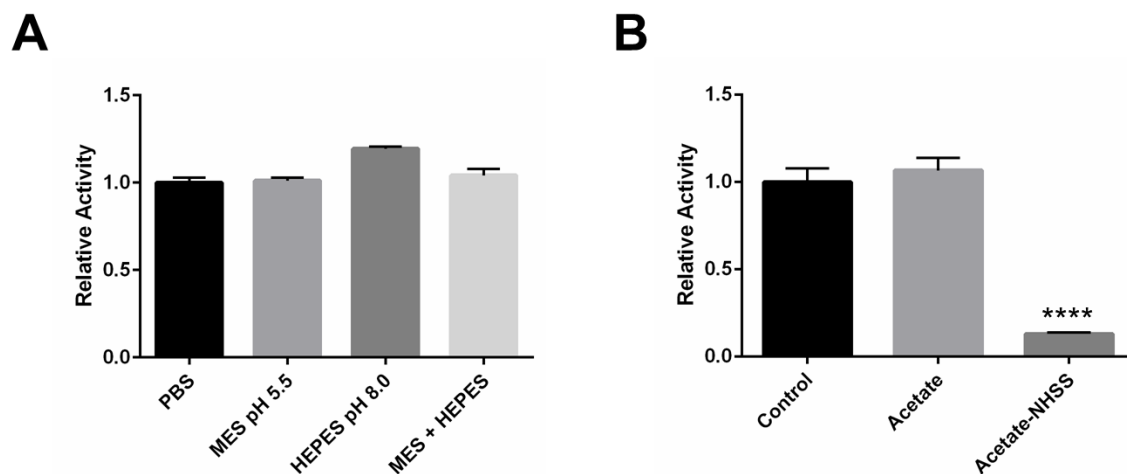
**Figure 5.8. Stability of lactate oxidase in EDC/NHS coupling conditions.** (A) Lactate oxidase activity is unaffected by incubation in buffers using during EDC/NHS coupling. (B) Conjugation of lactate oxidase to EDC/NHSS activated acetate results in the absence of enzymatic activity, likely due to the occupation of key reactive sites on the enzyme. The data are presented as the mean $\pm$ SD (n = 3). ****$p < 0.0001$.
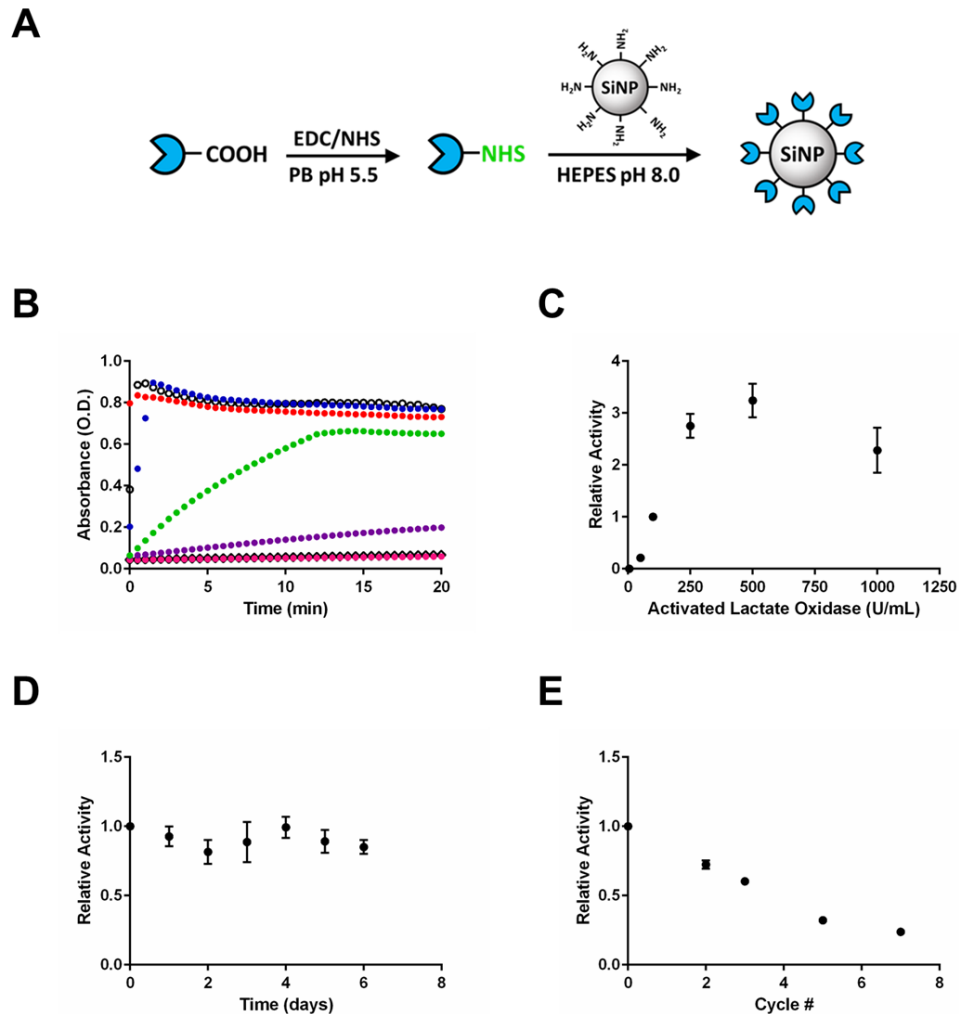
**Figure 5.9. Synthesis of lactate oxidase-coated silica nanoparticles for detection of lactate.** (A) Reaction scheme of lactate oxidase conjugation involving EDC/NHS activation of the enzyme followed by attachment to amine-coated silica nanoparticles by amide bonds. (B) Enzymatic activity of lactate oxidase is maintained when attached to a nanoparticle. (C) Conjugation of silica nanoparticles with increasing concentrations of activated lactate oxidase reaches a maximum at around 500 U/mL, after which the particles begin to aggregate and yield significantly decreases. (D) Lactate oxidase nanoparticles are stable at 37C and do not lose activity over 6 days. (E) Lactate oxidase nanoparticles are sensitive to lactate challenge and have reduced activity over repeated lactate exposure. The data are presented as the mean $\pm$ SD (n = 3).
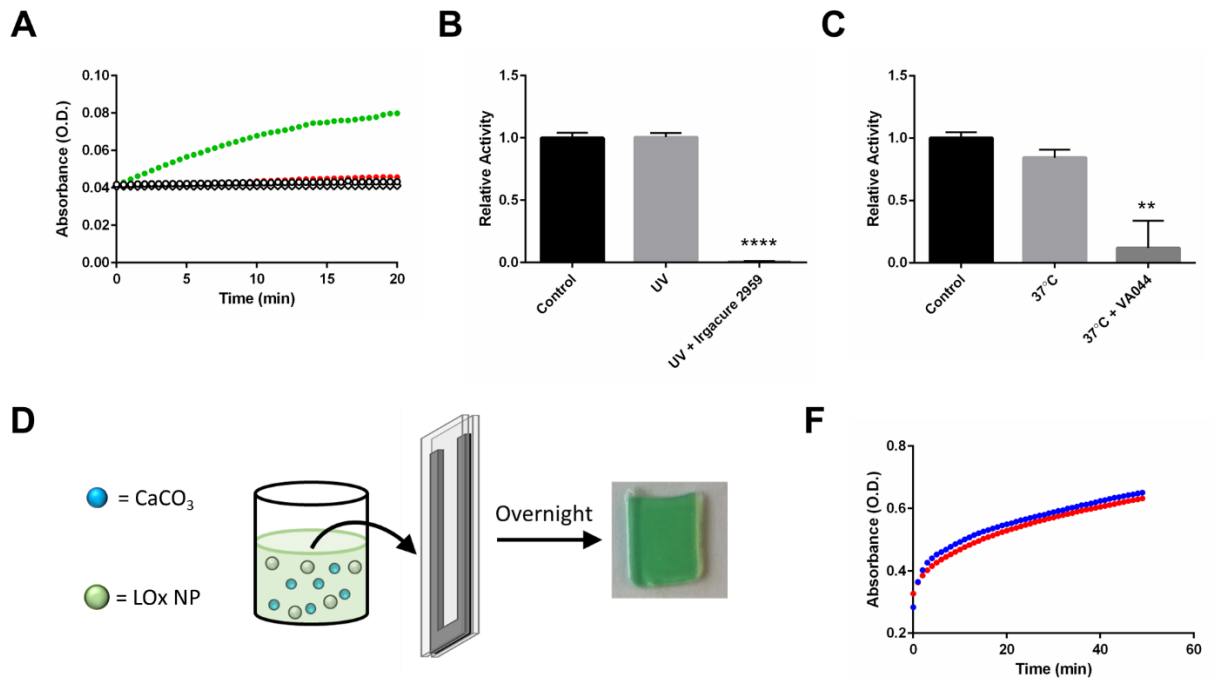
**Figure 5.10. Incorporation of lactate oxidase nanoparticles in alginate hydrogels scaffolds maintains enzymatic activity.** (A) Lactate oxidase nanoparticles lose enzymatic activity after incorporation into HEMA hydrogels (white circle = LOx hydrogel, white diamond = blank hydrogel, red = 0.125 mU/mL, green = 1.25 mU/mL, blue = water). (B,C) Lactate oxidase is stable at 37 °C and in the presence of UV light, but loses activity in the presence of thermal and photo-initiators. (D) Schematic of alginate hydrogel synthesis using internal gelation methods. (E) Activity of lactate oxidase is maintained after incorporation into the alginate hydrogel (blue = 1.5% w/v alginate, red = 2% w/v alginate). The data are presented as the mean ± SD (n = 3). **$p$ < 0.01, ****$p$ < 0.0001.

117

## Chapter 6 – Conclusion and Future Work

Chronic heart failure is a complex and debilitating medical condition affecting more than 26 million people worldwide[213]. While a multitude of therapeutic interventions have been developed to address the symptoms of CHF and improve patient quality of life, there is no effective therapy that treats the underlying complications of LV remodeling and reparative/interstitial fibrosis that lead to progressive deterioration of cardiac function. This is largely attributed to our incomplete understanding of the multifaceted processes involved in innate myocardial repair. For example, tissue scarring is a necessary response to acute injury that facilitates tissue recovery after trauma. In myocardial tissue, this physiological response becomes aberrant and pathological, leading to excessive synthesis of scar tissue and continuous tissue stiffening[5,7,11,12]. The mechanisms by which this happens has been extensively studied but effective interventions remain elusive. It has therefore become a large focus of heart failure research to target heart failure on a cellular level and elucidate the mechanisms myofibroblast transformation and phenotype to mitigate the aberrant responses that contribute to pathological fibrosis while allowing the beneficial aspects of rapid healing and recovery. In this dissertation, we presented novel research in the use of micro-engineered hydrogel materials for diagnostic and therapeutic applications for the management of heart failure.

First, we developed bioresorbable hyaluronic acid-based microrods that deliver local biophysical and biochemical cues to fibroblasts and cardiomyocytes for the attenuation of cardiac fibrosis and preservation of cardiac function after MI. The mechanical properties and degradation behavior of these microrods were extensively characterized and optimized for applications in cardiac fibrosis. These microstructures were shown to interact closely with cardiac fibroblasts *in vitro* and *in vivo*, which resulted in downregulated expression of genes

characteristic of myofibroblast transformation, including αSMA and Col1A2, as well as TGFβ and Smad3, key factors in mechanotransduction. Further, there was a downregulation of matrix metalloproteinases involved in LV remodeling, suggesting beneficial effects beyond attenuation of fibrosis. All of these changes resulted in functional improvements in an *in vivo* model of MI. While fabrication of microrods with bioactive polymers conferred favorable chemical and therapeutic properties to this micromechanical approach, there is great promise in adding chemical functionality through surface functionalization or drug loading to fit a range of scientific and therapeutic applications. We were able to attach single-stranded DNA to the surface of PEGDMA microrods for cell delivery applications, as well as attach proangiogenic peptides to the HA microrods to improve endothelial cell growth and promote vascularization. Microrods were also loaded with small molecule drugs to treat osteoarthritis and amino acids to improve beta cell survival for the treatment of type-1 diabetes. Additionally, magnetic nanoparticles were incorporated into the microrods, enabling remote manipulation of cardiomyocytes to study the effect of mechanical load on cellular phenotype by imaging. Collectively, these studies illustrate the immense diversity of modifications that can be made to this microtopography-based approach to improve existing therapeutic strategies and address a multitude of diseases.

Lastly, as with many chronic conditions, disease management is paramount to improving patient quality of life and increasing life expectancy. We synthesized a set of three optical nanosensors for the detection of oxygen, glucose and lactate. These nanosensors were incorporated into hydrogel scaffolds that can be implanted subcutaneously for continuous detection of these blood metabolites, which can be used to inform patients and healthcare providers of any changes in disease state for rapid and effective treatment.

In summary, this dissertation presents a broad set of technologies developed to address the chronic challenges of heart failure. While the material properties and therapeutic effects of the hyaluronic acid-based microrods have been thoroughly characterized, there remain unanswered questions regarding mechanism of action. The material effect of HA in myocardial infarction has been well appreciated in the presented experiments, as well as in the literature, but the biological mechanisms underlying the combination of HA with microtopography is still unclear. Future experiments will investigate the individual and synergistic roles of HA receptors and integrins on mechanotransduction that lead to the observed phenotypic changes in fibroblasts and cardiomyocytes. Furthermore, while the current HA microrod formulation was demonstrated to be effective in attenuating aberrant LV remodeling and preserving cardiac function, there remain opportunities to optimize stiffness or methacrylate percentage for improved therapeutic effects in the context of MI or for applications in other biological systems. Lastly, it will be critical to implant the optical nanosensors described in chapter 5 in an animal model to validate sensitivity, accuracy and stability. Together, these proposed studies will improve upon the technologies presented in this dissertation and enhance our currently limited capabilities in treating heart failure in a rapidly growing patient population.

**References**

1.  Peterson, E. D. *et al.* Trends in quality of care for patients with acute myocardial infarction in the National Registry of Myocardial Infarction from 1990 to 2006. *Am. Heart J.* **156,** 1045–1055 (2008).

2.  Inamdar, A. & Inamdar, A. Heart Failure: Diagnosis, Management and Utilization. *J. Clin. Med.* **5,** 62 (2016).

3.  Sutton, M. G. S. J. & Sharpe, N. Left Ventricular Remodeling After Myocardial Infarction. *Circulation* **101,** 2981–2988 (2000).

4.  Jackson, G., Gibbs, C. R., Davies, M. K. & Lip, G. Y. ABC of heart failure: Pathophysiology. *BMJ* **320,** 167–170 (2000).

5.  Segura, A. M., Frazier, O. H. & Buja, L. M. Fibrosis and heart failure. *Heart Fail. Rev.* **19,** 173–185 (2014).

6.  Chiong, M. *et al.* Cardiomyocyte death: mechanisms and translational implications. *Cell Death Dis.* **2,** e244 (2011).

7.  Frangogiannis, N. G. Pathophysiology of Myocardial Infarction. in *Comprehensive Physiology* **5,** 1841–1875 (John Wiley & Sons, Inc., 2015).

8.  Frangogiannis, N. G. The inflammatory response in myocardial injury, repair and remodelling. *Nat. Rev. Cardiol.* **11,** 255–265 (2014).

9.  Frangogiannis, N. G. Regulation of the Inflammatory Response in Cardiac Repair. *Circ. Res.* **110,** 159–173 (2012).

10. Prabhu, S. D. & Frangogiannis, N. G. The Biological Basis for Cardiac Repair After Myocardial Infarction. *Circ. Res.* **119,** 91–112 (2016).

11. Talman, V. & Ruskoaho, H. Cardiac fibrosis in myocardial infarction—from repair and

remodeling to regeneration. *Cell Tissue Res.* **365,** 563–581 (2016).

12. Li, L., Zhao, Q. & Kong, W. Extracellular matrix remodeling and cardiac fibrosis. *Matrix Biol.* **68–69,** 490–506 (2018).

13. van den Borne, S. W. M. *et al.* Myocardial remodeling after infarction: the role of myofibroblasts. *Nat. Rev. Cardiol.* **7,** 30–37 (2010).

14. Hinz, B. Formation and Function of the Myofibroblast during Tissue Repair. *J. Invest. Dermatol.* **127,** 526–537 (2007).

15. Desmoulière, A., Redard, M., Darby, I. & Gabbiani, G. Apoptosis mediates the decrease in cellularity during the transition between granulation tissue and scar. *Am. J. Pathol.* **146,** 56–66 (1995).

16. Willems, I. E., Havenith, M. G., De Mey, J. G. & Daemen, M. J. The alpha-smooth muscle actin-positive cells in healing human myocardial scars. *Am. J. Pathol.* **145,** 868–875 (1994).

17. Turner, N. A. & Porter, K. E. Function and fate of myofibroblasts after myocardial infarction. *Fibrogenesis Tissue Repair* **6,** 5 (2013).

18. Triposkiadis, F. *et al.* The Sympathetic Nervous System in Heart Failure. *J. Am. Coll. Cardiol.* **54,** 1747–1762 (2009).

19. Ma, T. K., Kam, K. K., Yan, B. P. & Lam, Y.-Y. Renin-angiotensin-aldosterone system blockade for cardiovascular diseases: current status. *Br. J. Pharmacol.* **160,** 1273–1292 (2010).

20. Gheorghiade, M., Colucci, W. S. & Swedberg, K. β-Blockers in Chronic Heart Failure. *Circulation* **107,** 1570–1575 (2003).

21. Olsen, S. L. *et al.* Carvedilol improves left ventricular function and symptoms in chronic

heart failure: A double-blind randomized study. *J. Am. Coll. Cardiol.* **25,** 1225–1231 (1995).

22.    Pfeffer, M. A., Lamas, G. A., Vaughan, D. E., Parisi, A. F. & Braunwald, E. Effect of Captopril on Progressive Ventricular Dilatation after Anterior Myocardial Infarction. *N. Engl. J. Med.* **319,** 80–86 (1988).

23.    Pfeffer, M. A. *et al.* Effect of Captopril on Mortality and Morbidity in Patients with Left Ventricular Dysfunction after Myocardial Infarction. *N. Engl. J. Med.* **327,** 669–677 (1992).

24.    MERIT-HF Study Group. Effect of metoprolol CR/XL in chronic heart failure: Metoprolol CR/XL Randomised Intervention Trial in-Congestive Heart Failure (MERIT-HF). *Lancet* **353,** 2001–2007 (1999).

25.    Ponikowski, P. *et al.* 2016 ESC Guidelines for the diagnosis and treatment of acute and chronic heart failure. *Eur. Heart J.* **37,** 2129–2200 (2016).

26.    Christman, K. L. & Lee, R. J. Biomaterials for the Treatment of Myocardial Infarction. *J. Am. Coll. Cardiol.* **48,** 907–913 (2006).

27.    Rane, A. A. & Christman, K. L. Biomaterials for the Treatment of Myocardial Infarction. *J. Am. Coll. Cardiol.* **58,** 2615–2629 (2011).

28.    Kwon, M. H., Cevasco, M., Schmitto, J. D. & Chen, F. Y. Ventricular restraint therapy for heart failure: A review, summary of state of the art, and future directions. *J. Thorac. Cardiovasc. Surg.* **144,** 771–777.e1 (2012).

29.    Mann, D. L. *et al.* Clinical Evaluation of the CorCap Cardiac Support Device in Patients With Dilated Cardiomyopathy. *Ann. Thorac. Surg.* **84,** 1226–1235 (2007).

30.    Starling, R. C. *et al.* Sustained Benefits of the CorCap Cardiac Support Device on Left

Ventricular Remodeling: Three Year Follow-up Results From the Acorn Clinical Trial. *Ann. Thorac. Surg.* **84,** 1236–1242 (2007).

31.	Mann, D. L. *et al.* Beneficial effects of the CorCap cardiac support device: Five-year results from the Acorn Trial. *J. Thorac. Cardiovasc. Surg.* **143,** 1036–1042 (2012).

32.	Mann, D. L. *et al.* Rationale, design, and methods for a pivotal randomized clinical trial for the assessment of a cardiac support device in patients with New York health association class III-IV heart failure. *J. Card. Fail.* **10,** 185–192 (2004).

33.	Starling, R. C. & Jessup, M. Worldwide clinical experience with the CorCap™ Cardiac Support Device. *J. Card. Fail.* **10,** S225–S233 (2004).

34.	Costanzo, M. R. *et al.* Ventricular Elastic Support Therapy (VEST) in Stage C Heart Failure-Analysis from the PEERLESS-HF Study. *J. Card. Fail.* **16,** 912 (2010).

35.	Oz, M. C. Surgical Implantation of the Acorn Cardiac Support Device. *Oper. Tech. Thorac. Cardiovasc. Surg.* **7,** 107–110 (2002).

36.	Walsh, R. G. Design and Features of the Acorn CorCapTM Cardiac Support Device: The Concept of Passive Mechanical Diastolic Support. *Heart Fail. Rev.* **10,** 101–107 (2005).

37.	Klodell, C. T. *et al.* Initial United States experience with the Paracor HeartNet∗ Paracor Medical, Inc, Sunnyvale, Calif. myocardial constraint device for heart failure. *J. Thorac. Cardiovasc. Surg.* **133,** 204–209 (2007).

38.	Blom, A. S. *et al.* Cardiac Support Device Modifies Left Ventricular Geometry and Myocardial Structure After Myocardial Infarction. *Circulation* **112,** 1274–1283 (2005).

39.	Pilla, J. J. *et al.* Passive ventricular constraint to improve left ventricular function and mechanics in an ovine model of heart failure secondary to acute myocardial infarction. *J. Thorac. Cardiovasc. Surg.* **126,** 1467–1475 (2003).

40. Magovern, J. A. *et al.* Effect of a Flexible Ventricular Restraint Device on Cardiac Remodeling after Acute Myocardial Infarction. *ASAIO J.* **52,** 196–200 (2006).

41. Li, Z. & Guan, J. Hydrogels for Cardiac Tissue Engineering. *Polymers (Basel).* **3,** 740–761 (2011).

42. Tous, E., Purcell, B., Ifkovits, J. L. & Burdick, J. A. Injectable Acellular Hydrogels for Cardiac Repair. *J. Cardiovasc. Transl. Res.* **4,** 528–542 (2011).

43. Nelson, D. M., Ma, Z., Fujimoto, K. L., Hashizume, R. & Wagner, W. R. Intra-myocardial biomaterial injection therapy in the treatment of heart failure: Materials, outcomes and challenges. *Acta Biomater.* **7,** 1–15 (2011).

44. Johnson, T. D. & Christman, K. L. Injectable hydrogel therapies and their delivery strategies for treating myocardial infarction. *Expert Opin. Drug Deliv.* **10,** 59–72 (2013).

45. Zhu, Y., Matsumura, Y. & Wagner, W. R. Ventricular wall biomaterial injection therapy after myocardial infarction: Advances in material design, mechanistic insight and early clinical experiences. *Biomaterials* **129,** 37–53 (2017).

46. Litwiniuk, M., Krejner, A., Speyrer, M. S., Gauto, A. R. & Grzela, T. Hyaluronic Acid in Inflammation and Tissue Regeneration. *Wounds* **28,** 78–88 (2016).

47. Noble, P. W. Hyaluronan and its catabolic products in tissue injury and repair. *Matrix Biol.* **21,** 25–29 (2002).

48. Toole, B. P. Hyaluronan: from extracellular glue to pericellular cue. *Nat. Rev. Cancer* **4,** 528–539 (2004).

49. Jiang, D., Liang, J. & Noble, P. W. Hyaluronan in Tissue Injury and Repair. *Annu. Rev. Cell Dev. Biol.* **23,** 435–461 (2007).

50. Chen, W. Y. J. & Abatangelo, G. Functions of hyaluronan in wound repair. *Wound Repair*

*Regen.* **7,** 79–89 (1999).

51. Tous, E. *et al.* Influence of Injectable Hyaluronic Acid Hydrogel Degradation Behavior on Infarction-Induced Ventricular Remodeling. *Biomacromolecules* **12,** 4127–4135 (2011).

52. Bonafe, F. *et al.* Hyaluronan and cardiac regeneration. *J. Biomed. Sci.* **21,** 100 (2014).

53. Ifkovits, J. L. *et al.* Injectable hydrogel properties influence infarct expansion and extent of postinfarction left ventricular remodeling in an ovine model. *Proc. Natl. Acad. Sci.* **107,** 11507–11512 (2010).

54. Yoon, S. J. *et al.* Regeneration of ischemic heart using hyaluronic acid-based injectable hydrogel. *J. Biomed. Mater. Res. Part B Appl. Biomater.* **91B,** 163–171 (2009).

55. Burdick, J. A. & Prestwich, G. D. Hyaluronic Acid Hydrogels for Biomedical Applications. *Adv. Mater.* **23,** H41–H56 (2011).

56. Seif-Naraghi, S. B. *et al.* Safety and Efficacy of an Injectable Extracellular Matrix Hydrogel for Treating Myocardial Infarction. *Sci. Transl. Med.* **5,** 173ra25-173ra25 (2013).

57. Wang, R. M. & Christman, K. L. Decellularized myocardial matrix hydrogels: In basic research and preclinical studies. *Adv. Drug Deliv. Rev.* **96,** 77–82 (2016).

58. Seif-Naraghi, S. B., Salvatore, M. A., Schup-Magoffin, P. J., Hu, D. P. & Christman, K. L. Design and Characterization of an Injectable Pericardial Matrix Gel: A Potentially Autologous Scaffold for Cardiac Tissue Engineering. *Tissue Eng. Part A* **16,** 2017–2027 (2010).

59. Singelyn, J. M. *et al.* Catheter-Deliverable Hydrogel Derived From Decellularized Ventricular Extracellular Matrix Increases Endogenous Cardiomyocytes and Preserves Cardiac Function Post-Myocardial Infarction. *J. Am. Coll. Cardiol.* **59,** 751–763 (2012).

60.   Frey, N. *et al.* Intracoronary Delivery of Injectable Bioabsorbable Scaffold (IK-5001) to Treat Left Ventricular Remodeling After ST-Elevation Myocardial Infarction. *Circ. Cardiovasc. Interv.* **7,** 806–812 (2014).

61.   Rao, S. V. *et al.* Bioabsorbable Intracoronary Matrix for Prevention of Ventricular Remodeling After Myocardial Infarction. *J. Am. Coll. Cardiol.* **68,** 715–723 (2016).

62.   Rao, S. V. *et al.* A randomized, double-blind, placebo-controlled trial to evaluate the safety and effectiveness of intracoronary application of a novel bioabsorbable cardiac matrix for the prevention of ventricular remodeling after large ST-segment elevation myocardial inf. *Am. Heart J.* **170,** 929–937 (2015).

63.   Lee, R. J., Hinson, A., Helgerson, S., Bauernschmitt, R. & Sabbah, H. N. Polymer-Based Restoration of Left Ventricular Mechanics. *Cell Transplant.* **22,** 529–533 (2013).

64.   Lee, L. C. *et al.* Algisyl-LVR$^{TM}$ with coronary artery bypass grafting reduces left ventricular wall stress and improves function in the failing human heart. *Int. J. Cardiol.* **168,** 2022–2028 (2013).

65.   Mann, D. L. *et al.* One-year follow-up results from AUGMENT-HF: a multicentre randomized controlled clinical trial of the efficacy of left ventricular augmentation with Algisyl in the treatment of heart failure. *Eur. J. Heart Fail.* **18,** 314–325 (2016).

66.   Anker, S. D. *et al.* A prospective comparison of alginate-hydrogel with standard medical therapy to determine impact on functional capacity and clinical outcomes in patients with advanced heart failure (AUGMENT-HF trial). *Eur. Heart J.* **36,** 2297–2309 (2015).

67.   Lipinski, M. J. *et al.* Impact of Intracoronary Cell Therapy on Left Ventricular Function in the Setting of Acute Myocardial Infarction. *J. Am. Coll. Cardiol.* **50,** 1761–1767 (2007).

68.   Mathieu, E. *et al.* Intramyocardial Delivery of Mesenchymal Stem Cell-Seeded Hydrogel

Preserves Cardiac Function and Attenuates Ventricular Remodeling after Myocardial Infarction. *PLoS One* **7,** e51991 (2012).

69. Spath, N. B., Mills, N. L. & Cruden, N. L. Novel cardioprotective and regenerative therapies in acute myocardial infarction: a review of recent and ongoing clinical trials. *Future Cardiol.* **12,** 655–672 (2016).

70. Jakob, P. & Landmesser, U. Current Status of Cell-Based Therapy for Heart Failure. *Curr. Heart Fail. Rep.* **10,** 165–176 (2013).

71. Chugh, A. R. *et al.* Administration of Cardiac Stem Cells in Patients With Ischemic Cardiomyopathy: The SCIPIO Trial: Surgical Aspects and Interim Analysis of Myocardial Function and Viability by Magnetic Resonance. *Circulation* **126,** S54–S64 (2012).

72. Rosenzweig, A. Cardiac Cell Therapy — Mixed Results from Mixed Cells. *N. Engl. J. Med.* **355,** 1274–1277 (2006).

73. Nigro, P. *et al.* Cell therapy for heart disease after 15 years: Unmet expectations. *Pharmacol. Res.* **127,** 77–91 (2018).

74. Young, P. P. & Schäfer, R. Cell-based therapies for cardiac disease: a cellular therapist's perspective. *Transfusion* **55,** 441–451 (2015).

75. Chimenti, I. *et al.* Relative Roles of Direct Regeneration Versus Paracrine Effects of Human Cardiosphere-Derived Cells Transplanted Into Infarcted Mice. *Circ. Res.* **106,** 971–980 (2010).

76. Duran, J. M. *et al.* Bone-Derived Stem Cells Repair the Heart After Myocardial Infarction Through Transdifferentiation and Paracrine Signaling Mechanisms. *Circ. Res.* **113,** 539–552 (2013).

77. Luo, L. *et al.* Fabrication of Synthetic Mesenchymal Stem Cells for the Treatment of

Acute Myocardial Infarction in Mice. *Circ. Res.* **120,** 1768–1775 (2017).

78. Tang, J. *et al.* Therapeutic microparticles functionalized with biomimetic cardiac stem cell membranes and secretome. *Nat. Commun.* **8,** 1–9 (2017).

79. Li, T.-S. *et al.* Direct Comparison of Different Stem Cell Types and Subpopulations Reveals Superior Paracrine Potency and Myocardial Repair Efficacy With Cardiosphere-Derived Cells. *J. Am. Coll. Cardiol.* **59,** 942–953 (2012).

80. Mirotsou, M., Jayawardena, T. M., Schmeckpeper, J., Gnecchi, M. & Dzau, V. J. Paracrine mechanisms of stem cell reparative and regenerative actions in the heart. *J. Mol. Cell. Cardiol.* **50,** 280–289 (2011).

81. Gnecchi, M., Zhang, Z., Ni, A. & Dzau, V. J. Paracrine Mechanisms in Adult Stem Cell Signaling and Therapy. *Circ. Res.* **103,** 1204–1219 (2008).

82. Ye, L., Zimmermann, W.-H., Garry, D. J. & Zhang, J. Patching the Heart. *Circ. Res.* **113,** 922–932 (2013).

83. Stoppel, W. L., Hu, D., Domian, I. J., Kaplan, D. L. & Black, L. D. Anisotropic silk biomaterials containing cardiac extracellular matrix for cardiac tissue engineering. *Biomed. Mater.* **10,** 034105 (2015).

84. Li, X., Tamama, K., Xie, X. & Guan, J. Improving Cell Engraftment in Cardiac Stem Cell Therapy. *Stem Cells Int.* **2016,** 1–11 (2016).

85. Curtis, M. W. & Russell, B. Micromechanical regulation in cardiac myocytes and fibroblasts: implications for tissue remodeling. *Pflügers Arch. - Eur. J. Physiol.* **462,** 105–117 (2011).

86. Herum, K., Lunde, I., McCulloch, A. & Christensen, G. The Soft- and Hard-Heartedness of Cardiac Fibroblasts: Mechanotransduction Signaling Pathways in Fibrosis of the Heart.

*J. Clin. Med.* **6,** 53 (2017).

87.   Hinz, B. The myofibroblast: Paradigm for a mechanically active cell. *J. Biomech.* **43,** 146–155 (2010).

88.   Gwak, S.-J. *et al.* The effect of cyclic strain on embryonic stem cell-derived cardiomyocytes. *Biomaterials* **29,** 844–856 (2008).

89.   Fan, D., Takawale, A., Lee, J. & Kassiri, Z. Cardiac fibroblasts, fibrosis and extracellular matrix remodeling in heart disease. *Fibrogenesis Tissue Repair* **5,** 15 (2012).

90.   Boateng, S. Y. *et al.* Inhibition of fibroblast proliferation in cardiac myocyte cultures by surface microtopography. *Am. J. Physiol. Physiol.* **285,** C171–C182 (2003).

91.   Allen, J. *et al.* Tunable Microfibers Suppress Fibrotic Encapsulation via Inhibition of TGFβ Signaling. *Tissue Eng. Part A* **22,** 142–150 (2016).

92.   Ayala, P., Lopez, J. I. & Desai, T. A. Microtopographical Cues in 3D Attenuate Fibrotic Phenotype and Extracellular Matrix Deposition: Implications for Tissue Regeneration. *Tissue Eng. Part A* **16,** 2519–2527 (2010).

93.   Pinney, J. R. *et al.* Discrete microstructural cues for the attenuation of fibrosis following myocardial infarction. *Biomaterials* **35,** 8820–8828 (2014).

94.   Discher, D. E. Tissue Cells Feel and Respond to the Stiffness of Their Substrate. *Science (80-. ).* **310,** 1139–1143 (2005).

95.   Vogel, V. & Sheetz, M. Local force and geometry sensing regulate cell functions. *Nat. Rev. Mol. Cell Biol.* **7,** 265–275 (2006).

96.   Yeung, T. *et al.* Effects of substrate stiffness on cell morphology, cytoskeletal structure, and adhesion. *Cell Motil. Cytoskeleton* **60,** 24–34 (2005).

97.   Ingber, D. E. Cellular mechanotransduction: putting all the pieces together again. *FASEB*

*J.* **20,** 811–827 (2006).

98.     McNamara, L. E. *et al.* The role of microtopography in cellular mechanotransduction. *Biomaterials* **33,** 2835–2847 (2012).

99.     Jaalouk, D. E. & Lammerding, J. Mechanotransduction gone awry. *Nat. Rev. Mol. Cell Biol.* **10,** 63–73 (2009).

100.    Humphrey, J. D., Dufresne, E. R. & Schwartz, M. A. Mechanotransduction and extracellular matrix homeostasis. *Nat. Rev. Mol. Cell Biol.* **15,** 802–812 (2014).

101.    Katsumi, A., Orr, A. W., Tzima, E. & Schwartz, M. A. Integrins in Mechanotransduction. *J. Biol. Chem.* **279,** 12001–12004 (2004).

102.    Orr, A. W., Helmke, B. P., Blackman, B. R. & Schwartz, M. A. Mechanisms of Mechanotransduction. *Dev. Cell* **10,** 11–20 (2006).

103.    Puklin-Faucher, E. & Sheetz, M. P. The mechanical integrin cycle. *J. Cell Sci.* **122,** 179–186 (2009).

104.    Cyphert, J. M., Trempus, C. S. & Garantziotis, S. Size Matters: Molecular Weight Specificity of Hyaluronan Effects in Cell Biology. *Int. J. Cell Biol.* **2015,** 1–8 (2015).

105.    Itano, N. Simple Primary Structure, Complex Turnover Regulation and Multiple Roles of Hyaluronan. *J. Biochem.* **144,** 131–137 (2008).

106.    Petrey, A. C. & de la Motte, C. A. Hyaluronan, a crucial regulator of inflammation. *Front. Immunol.* **5,** 1–13 (2014).

107.    Ruppert, S. M., Hawn, T. R., Arrigoni, A., Wight, T. N. & Bollyky, P. L. Tissue integrity signals communicated by high-molecular weight hyaluronan and the resolution of inflammation. *Immunol. Res.* **58,** 186–192 (2014).

108.    Yang, C. *et al.* The High and Low Molecular Weight Forms of Hyaluronan Have Distinct

Effects on CD44 Clustering. *J. Biol. Chem.* **287,** 43094–43107 (2012).

109. Bencherif, S. A. *et al.* Influence of the degree of methacrylation on hyaluronic acid hydrogels properties. *Biomaterials* **29,** 1739–1749 (2008).

110. Cesaretti, M., Luppi, E., Maccari, F. & Volpi, N. A 96-well assay for uronic acid carbazole reaction. *Carbohydr. Polym.* **54,** 59–61 (2003).

111. Lin, Y.-H., Li, J., Swanson, E. R. & Russell, B. CapZ and actin capping dynamics increase in myocytes after a bout of exercise and abates in hours after stimulation ends. *J. Appl. Physiol.* **114,** 1603–1609 (2013).

112. Motlagh, D., Hartman, T. J., Desai, T. A. & Russell, B. Microfabricated grooves recapitulate neonatal myocyte connexin43 and N-cadherin expression and localization. *J. Biomed. Mater. Res.* **67A,** 148–157 (2003).

113. Deutsch, J., Motlagh, D., Russell, B. & Desai, T. A. Fabrication of microtextured membranes for cardiac myocyte attachment and orientation. *J. Biomed. Mater. Res.* **53,** 267–275 (2000).

114. Norman, J. J., Collins, J. M., Sharma, S., Russell, B. & Desai, T. A. Microstructures in 3D Biological Gels Affect Cell Proliferation. *Tissue Eng. Part A* **14,** 379–390 (2008).

115. Hachet, E., Van Den Berghe, H., Bayma, E., Block, M. R. & Auzély-Velty, R. Design of Biomimetic Cell-Interactive Substrates Using Hyaluronic Acid Hydrogels with Tunable Mechanical Properties. *Biomacromolecules* **13,** 1818–1827 (2012).

116. Oudshoorn, M. H. M., Rissmann, R., Bouwstra, J. A. & Hennink, W. E. Synthesis of methacrylated hyaluronic acid with tailored degree of substitution. *Polymer (Guildf).* **48,** 1915–1920 (2007).

117. Burdick, J. A., Chung, C., Jia, X., Randolph, M. A. & Langer, R. Controlled Degradation

and Mechanical Behavior of Photopolymerized Hyaluronic Acid Networks. *Biomacromolecules* **6,** 386–391 (2005).

118. Tavsanli, B., Can, V. & Okay, O. Mechanically strong triple network hydrogels based on hyaluronan and poly(N,N-dimethylacrylamide). *Soft Matter* **11,** 8517–8524 (2015).

119. Reis, A. V *et al.* Reaction of Glycidyl Methacrylate at the Hydroxyl and Carboxylic Groups of Poly(vinyl alcohol) and Poly(acrylic acid): Is This Reaction Mechanism Still Unclear? *J. Org. Chem.* **74,** 3750–3757 (2009).

120. Khademhosseini, A. *et al.* Micromolding of photocrosslinkable hyaluronic acid for cell encapsulation and entrapment. *J. Biomed. Mater. Res. Part A* **79A,** 522–532 (2006).

121. Chopra, A. *et al.* Augmentation of integrin-mediated mechanotransduction by hyaluronic acid. *Biomaterials* **35,** 71–82 (2014).

122. Chopra, A. *et al.* Reprogramming cardiomyocyte mechanosensing by crosstalk between integrins and hyaluronic acid receptors. *J. Biomech.* **45,** 824–831 (2012).

123. Bhattacharya, D. S. *et al.* Impact of structurally modifying hyaluronic acid on CD44 interaction. *J. Mater. Chem. B* **5,** 8183–8192 (2017).

124. Naghavi, M. *et al.* Global, regional, and national age-sex specific mortality for 264 causes of death, 1980–2016: a systematic analysis for the Global Burden of Disease Study 2016. *Lancet* **390,** 1151–1210 (2017).

125. Konstam, M. A., Kramer, D. G., Patel, A. R., Maron, M. S. & Udelson, J. E. Left Ventricular Remodeling in Heart Failure. *JACC Cardiovasc. Imaging* **4,** 98–108 (2011).

126. Hasan, A. *et al.* Injectable Hydrogels for Cardiac Tissue Repair after Myocardial Infarction. *Adv. Sci.* **2,** 1500122 (2015).

127. Lee, R. J. *et al.* The feasibility and safety of Algisyl-LVR™ as a method of left ventricular

augmentation in patients with dilated cardiomyopathy: Initial first in man clinical results. *Int. J. Cardiol.* **199,** 18–24 (2015).

128. Yu, J. *et al.* Restoration of left ventricular geometry and improvement of left ventricular function in a rodent model of chronic ischemic cardiomyopathy. *J. Thorac. Cardiovasc. Surg.* **137,** 180–187 (2009).

129. Adams, J. C. & Watt, F. M. Regulation of development and differentiation by the extracellular matrix. *Development* **117,** 1183–98 (1993).

130. Frantz, C., Stewart, K. M. & Weaver, V. M. The extracellular matrix at a glance. *J. Cell Sci.* **123,** 4195–4200 (2010).

131. Hynes, R. O. The Extracellular Matrix: Not Just Pretty Fibrils. *Science (80-. ).* **326,** 1216–1219 (2009).

132. Shinde, A. V. & Frangogiannis, N. G. Fibroblasts in myocardial infarction: A role in inflammation and repair. *J. Mol. Cell. Cardiol.* **70,** 74–82 (2014).

133. Porter, K. E. & Turner, N. A. Cardiac fibroblasts: At the heart of myocardial remodeling. *Pharmacol. Ther.* **123,** 255–278 (2009).

134. Weber, K. T., Sun, Y., Bhattacharya, S. K., Ahokas, R. A. & Gerling, I. C. Myofibroblast-mediated mechanisms of pathological remodelling of the heart. *Nat. Rev. Cardiol.* **10,** 15–26 (2013).

135. Broughton, K. M. & Russell, B. Cardiomyocyte subdomain contractility arising from microenvironmental stiffness and topography. *Biomech. Model. Mechanobiol.* **14,** 589–602 (2015).

136. Mihardja, S. S. *et al.* The effect of a peptide-modified thermo-reversible methylcellulose on wound healing and LV function in a chronic myocardial infarction rodent model.

*Biomaterials* **34,** 8869–8877 (2013).

137. Ungerleider, J. L. & Christman, K. L. Concise Review: Injectable Biomaterials for the Treatment of Myocardial Infarction and Peripheral Artery Disease: Translational Challenges and Progress. *Stem Cells Transl. Med.* **3,** 1090–1099 (2014).

138. Huebener, P. *et al.* CD44 Is Critically Involved in Infarct Healing by Regulating the Inflammatory and Fibrotic Response. *J. Immunol.* **180,** 2625–2633 (2008).

139. Gao, F. *et al.* Hyaluronan oligosaccharides promote excisional wound healing through enhanced angiogenesis. *Matrix Biol.* **29,** 107–116 (2010).

140. Pogorilyi, R. P., Melnyk, I. V., Zub, Y. L., Seisenbaeva, G. A. & Kessler, V. G. Immobilization of urease on magnetic nanoparticles coated by polysiloxane layers bearing thiol- or thiol- and alkyl-functions. *J. Mater. Chem. B* **2,** 2694–2702 (2014).

141. Pinney, J. R., Melkus, G., Cerchiari, A., Hawkins, J. & Desai, T. A. Novel Functionalization of Discrete Polymeric Biomaterial Microstructures for Applications in Imaging and Three-Dimensional Manipulation. *ACS Appl. Mater. Interfaces* **6,** 14477–14485 (2014).

142. Li, J., Tanhehco, E. J. & Russell, B. Actin dynamics is rapidly regulated by the PTEN and PIP 2 signaling pathways leading to myocyte hypertrophy. *Am. J. Physiol. Hear. Circ. Physiol.* **307,** H1618–H1625 (2014).

143. Louch, W. E., Sheehan, K. A. & Wolska, B. M. Methods in cardiomyocyte isolation, culture, and gene transfer. *J. Mol. Cell. Cardiol.* **51,** 288–298 (2011).

144. Faleo, G. *et al.* Mitigating Ischemic Injury of Stem Cell-Derived Insulin-Producing Cells after Transplant. *Stem Cell Reports* **9,** 807–819 (2017).

145. Mihardja, S. S., Yu, J. & Lee, R. J. Extracellular matrix-derived peptides and myocardial

repair. *Cell Adh. Migr.* **5,** 111–113 (2011).

146. Mihardja, S. S. *et al.* Targeted In Vivo Extracellular Matrix Formation Promotes Neovascularization in a Rodent Model of Myocardial Infarction. *PLoS One* **5,** e10384 (2010).

147. Doroudian, G. *et al.* Sustained delivery of MGF peptide from microrods attracts stem cells and reduces apoptosis of myocytes. *Biomed. Microdevices* **16,** 705–715 (2014).

148. Sridhar, B. V. *et al.* Development of a Cellularly Degradable PEG Hydrogel to Promote Articular Cartilage Extracellular Matrix Deposition. *Adv. Healthc. Mater.* **4,** 702–713 (2015).

149. van Dijk, M., van Nostrum, C. F., Hennink, W. E., Rijkers, D. T. S. & Liskamp, R. M. J. Synthesis and Characterization of Enzymatically Biodegradable PEG and Peptide-Based Hydrogels Prepared by Click Chemistry. *Biomacromolecules* **11,** 1608–1614 (2010).

150. Yang, J., Jacobsen, M. T., Pan, H. & Kopeček, J. Synthesis and Characterization of Enzymatically Degradable PEG-Based Peptide-Containing Hydrogels. *Macromol. Biosci.* **10,** 445–454 (2010).

151. Yu, J. *et al.* Synthesis and characterization of MMP degradable and maleimide cross-linked PEG hydrogels for tissue engineering scaffolds. *Polym. Degrad. Stab.* **133,** 312–320 (2016).

152. Lutolf, M. P. *et al.* Synthetic matrix metalloproteinase-sensitive hydrogels for the conduction of tissue regeneration: Engineering cell-invasion characteristics. *Proc. Natl. Acad. Sci.* **100,** 5413–5418 (2003).

153. Gartner, Z. J. & Bertozzi, C. R. Programmed assembly of 3-dimensional microtissues with defined cellular connectivity. *Proc. Natl. Acad. Sci.* **106,** 4606–4610 (2009).

154.  Selden, N. S. *et al.* Chemically Programmed Cell Adhesion with Membrane-Anchored Oligonucleotides. *J. Am. Chem. Soc.* **134,** 765–768 (2012).

155.  Weber, R. J., Liang, S. I., Selden, N. S., Desai, T. A. & Gartner, Z. J. Efficient Targeting of Fatty-Acid Modified Oligonucleotides to Live Cell Membranes through Stepwise Assembly. *Biomacromolecules* **15,** 4621–4626 (2014).

156.  Pinney, J. R., Melkus, G., Cerchiari, A., Hawkins, J. & Desai, T. A. (NO) Novel functionalization of discrete polymeric biomaterial microstructures for applications in imaging and three-dimensional manipulation (NO). *ACS Appl. Mater. Interfaces* **6,** 14477–14485 (2014).

157.  Sniadecki, N. J., Lamb, C. M., Liu, Y., Chen, C. S. & Reich, D. H. Magnetic microposts for mechanical stimulation of biological cells: Fabrication, characterization, and analysis. *Rev. Sci. Instrum.* **79,** 044302 (2008).

158.  Bidan, C. M. *et al.* Magneto-active substrates for local mechanical stimulation of living cells. *Sci. Rep.* **8,** 1464 (2018).

159.  Mansour, H., de Tombe, P. P., Samarel, A. M. & Russell, B. Restoration of Resting Sarcomere Length After Uniaxial Static Strain Is Regulated by Protein Kinase Cε and Focal Adhesion Kinase. *Circ. Res.* **94,** 642–649 (2004).

160.  Yu, J.-G. & Russell, B. Cardiomyocyte Remodeling and Sarcomere Addition after Uniaxial Static Strain In Vitro. *J. Histochem. Cytochem.* **53,** 839–844 (2005).

161.  Li, J. & Russell, B. Phosphatidylinositol 4,5-bisphosphate regulates CapZβ1 and actin dynamics in response to mechanical strain. *Am. J. Physiol. Hear. Circ. Physiol.* **305,** H1614–H1623 (2013).

162.  Katz, A. M. Ernest Henry Starling, His Predecessors, and the "Law of the Heart".

*Circulation* **106,** 2986–2992 (2002).

163. de Tombe, P. P. & ter Keurs, H. E. D. J. Cardiac muscle mechanics: Sarcomere length matters. *J. Mol. Cell. Cardiol.* **91,** 148–150 (2016).

164. Khavjou, O., Phelps, D. & Leib, A. *Projections of Cardiovascular Disease Prevalence and Costs: 2015-2035*. *RTI International* (2016).

165. Bui, A. L. & Fonarow, G. C. Home Monitoring for Heart Failure Management. *J. Am. Coll. Cardiol.* **59,** 97–104 (2012).

166. Jencks, S. F., Williams, M. V. & Coleman, E. A. Rehospitalizations among Patients in the Medicare Fee-for-Service Program. *N. Engl. J. Med.* **360,** 1418–1428 (2009).

167. Bergethon, K. E. *et al.* Trends in 30-Day Readmission Rates for Patients Hospitalized With Heart Failure. *Circ. Hear. Fail.* **9,** 1–8 (2016).

168. Ross, J. S. *et al.* Recent National Trends in Readmission Rates After Heart Failure Hospitalization. *Circ. Hear. Fail.* **3,** 97–103 (2010).

169. Krumholz, H. M. Post-Hospital Syndrome — An Acquired, Transient Condition of Generalized Risk. *N. Engl. J. Med.* **368,** 100–102 (2013).

170. Emani, S. Remote Monitoring to Reduce Heart Failure Readmissions. *Curr. Heart Fail. Rep.* **14,** 40–47 (2017).

171. Würtz, P. *et al.* Metabolite Profiling and Cardiovascular Event Risk. *Circulation* **131,** 774–785 (2015).

172. Merchant, F. M., Dec, G. W. & Singh, J. P. Implantable Sensors for Heart Failure. *Circ. Arrhythmia Electrophysiol.* **3,** 657–667 (2010).

173. Braunwald, E. Biomarkers in Heart Failure. *N. Engl. J. Med.* **358,** 2148–2159 (2008).

174. Matsushita, K. *et al.* The Association of Plasma Lactate With Incident Cardiovascular

Outcomes. *Am. J. Epidemiol.* **178,** 401–409 (2013).

175. Nichols, G. A., Gullion, C. M., Koro, C. E., Ephross, S. A. & Brown, J. B. The Incidence of Congestive Heart Failure in Type 2 Diabetes: An update. *Diabetes Care* **27,** 1879–1884 (2004).

176. Kannel, W. B. & McGee, D. L. Diabetes and Glucose Tolerance as Risk Factors for Cardiovascular Disease: The Framingham Study. *Diabetes Care* **2,** 120–126 (1979).

177. Murcia, A. M. *et al.* Impact of Diabetes on Mortality in Patients With Myocardial Infarction and Left Ventricular Dysfunction. *Arch. Intern. Med.* **164,** 2273 (2004).

178. Kannel, W. & McGee, D. Diabetes and Cardiovascular Disease: The Framingham Study. *JAMA* **241,** 2035–2038 (1979).

179. Burge, M. R. Lack of Compliance With Home Blood Glucose Monitoring Predicts Hospitalization in Diabetes. *Diabetes Care* **24,** 1502–1503 (2001).

180. Vincze, G., Barner, J. C. & Lopez, D. Factors Associated With Adherence to Self-Monitoring of Blood Glucose Among Persons With Diabetes. *Diabetes Educ.* **30,** 112–125 (2004).

181. Bindra, D. S. *et al.* Design and in vitro studies of a needle-type glucose sensor for subcutaneous monitoring. *Anal. Chem.* **63,** 1692–1696 (1991).

182. Wang, H.-C. & Lee, A.-R. Recent developments in blood glucose sensors. *J. Food Drug Anal.* **23,** 191–200 (2015).

183. Klonoff, D. C. Continuous Glucose Monitoring: Roadmap for 21st century diabetes therapy. *Diabetes Care* **28,** 1231–1239 (2005).

184. Koschwanez, H. E. & Reichert, W. M. In vitro, in vivo and post explantation testing of glucose-detecting biosensors: Current methods and recommendations. *Biomaterials* **28,**

3687–3703 (2007).

185. Pickup, J. C., Claremont, D. J. & Shaw, G. W. Responses and calibration of amperometric glucose sensors implanted in the subcutaneous tissue of man. *Acta Diabetol.* **30,** 143–148 (1993).

186. Yu, B., Ju, Y., West, L., Moussy, Y. & Moussy, F. An Investigation of Long-Term Performance of Minimally Invasive Glucose Biosensors. *Diabetes Technol. Ther.* **9,** 265–275 (2007).

187. Andrus, L., Unruh, R., Wisniewski, N. & McShane, M. Characterization of Lactate Sensors Based on Lactate Oxidase and Palladium Benzoporphyrin Immobilized in Hydrogels. *Biosensors* **5,** 398–416 (2015).

188. Roberts, J. R., Park, J., Helton, K., Wisniewski, N. & McShane, M. J. Biofouling of Polymer Hydrogel Materials and its Effect on Diffusion and Enzyme-Based Luminescent Glucose Sensor Functional Characteristics. *J. Diabetes Sci. Technol.* **6,** 1267–1275 (2012).

189. Roberts, J. R., Ritter, D. W. & McShane, M. J. A design full of holes: functional nanofilm-coated microdomains in alginate hydrogels. *J. Mater. Chem. B* **1,** 3195 (2013).

190. Kuo, C. K. & Ma, P. X. Ionically crosslinked alginate hydrogels as scaffolds for tissue engineering: Part 1. Structure, gelation rate and mechanical properties. *Biomaterials* **22,** 511–521 (2001).

191. Gaggin, H. K. & Januzzi, J. L. Biomarkers and diagnostics in heart failure. *Biochim. Biophys. Acta* **1832,** 2442–2450 (2013).

192. de Boer, R. A., Daniels, L. B., Maisel, A. S. & Januzzi, J. L. State of the Art: Newer biomarkers in heart failure. *Eur. J. Heart Fail.* **17,** 559–569 (2015).

193. Held, C. *et al.* Glucose Levels Predict Hospitalization for Congestive Heart Failure in

Patients at High Cardiovascular Risk. *Circulation* **115,** 1371–1375 (2007).

194. Munger, M. A. *et al.* Arterial oxygen saturation in chronic congestive heart failure. *Am. J. Cardiol.* **73,** 180–185 (1994).

195. Nielson, C. & Lange, T. Blood Glucose and Heart Failure in Nondiabetic Patients. *Diabetes Care* **28,** 607–611 (2005).

196. Park, C. S. *et al.* Acute Myocardial Infarction Is a Risk Factor for New Onset Diabetes in Patients with Coronary Artery Disease. *PLoS One* **10,** e0136354 (2015).

197. Mozaffarian, D. *et al.* Incidence of new-onset diabetes and impaired fasting glucose in patients with recent myocardial infarction and the effect of clinical and lifestyle risk factors. *Lancet* **370,** 667–675 (2007).

198. Chien, J. S. *et al.* Injectable Phosphorescence-based Oxygen Biosensors Identify Post Ischemic Reactive Hyperoxia. *Sci. Rep.* **7,** 8255 (2017).

199. Wisniewski, N. A. *et al.* Tissue-Integrating Oxygen Sensors: Continuous Tracking of Tissue Hypoxia. in *Advances in Experimental Medicine and Biology* 377–383 (2017). doi:10.1007/978-3-319-55231-6_49

200. Cordes, D. B. *et al.* Optical glucose detection across the visible spectrum using anionic fluorescent dyes and a viologen quencher in a two-component saccharide sensing system. *Org. Biomol. Chem.* **3,** 1708–1713 (2005).

201. Cordes, D. B., Gamsey, S. & Singaram, B. Fluorescent Quantum Dots with Boronic Acid Substituted Viologens To Sense Glucose in Aqueous Solution. *Angew. Chemie Int. Ed.* **45,** 3829–3832 (2006).

202. Cordes, D. B., Miller, A., Gamsey, S. & Singaram, B. Simultaneous use of multiple fluorescent reporter dyes for glucose sensing in aqueous solution. *Anal. Bioanal. Chem.*

**387,** 2767–2773 (2007).

203.  Cordes, D. B. *et al.* The Interaction of Boronic Acid-Substituted Viologens with Pyranine: The Effects of Quencher Charge on Fluorescence Quenching and Glucose Response. *Langmuir* **21,** 6540–6547 (2005).

204.  Gamsey, S., Suri, J. T., Wessling, R. A. & Singaram, B. Continuous Glucose Detection Using Boronic Acid-Substituted Viologens in Fluorescent Hydrogels: Linker Effects and Extension to Fiber Optics. *Langmuir* **22,** 9067–9074 (2006).

205.  Suri, J. T., Cordes, D. B., Cappuccio, F. E., Wessling, R. A. & Singaram, B. Continuous Glucose Sensing with a Fluorescent Thin-Film Hydrogel. *Angew. Chemie Int. Ed.* **42,** 5857–5859 (2003).

206.  Gamsey, S. *et al.* The effect of boronic acid-positioning in an optical glucose-sensing ensemble. *Tetrahedron* **62,** 6321–6331 (2006).

207.  Heller, A. & Feldman, B. Electrochemical Glucose Sensors and Their Applications in Diabetes Management. *Chem. Rev.* **108,** 2482–2505 (2008).

208.  Brown, J. Q., Srivastava, R. & McShane, M. J. Encapsulation of glucose oxidase and an oxygen-quenched fluorophore in polyelectrolyte-coated calcium alginate microspheres as optical glucose sensor systems. *Biosens. Bioelectron.* **21,** 212–216 (2005).

209.  Unruh, R. M. *et al.* Preclinical Evaluation of Poly(HEMA-co-acrylamide) Hydrogels Encapsulating Glucose Oxidase and Palladium Benzoporphyrin as Fully Implantable Glucose Sensors. *J. Diabetes Sci. Technol.* **9,** 985–992 (2015).

210.  Minagawa, H. *et al.* Improving the thermal stability of lactate oxidase by directed evolution. *Cell. Mol. Life Sci.* **64,** 77–81 (2007).

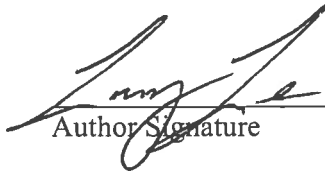211.  Minagawa, H., Nakayama, N., Matsumoto, T. & Ito, N. Development of long life lactate

sensor using thermostable mutant lactate oxidase. *Biosens. Bioelectron.* **13,** 313–318 (1998).

212. Lillis, B., Grogan, C., Berney, H. & Lane, W. . Investigation into immobilisation of lactate oxidase to improve stability. *Sensors Actuators B Chem.* **68,** 109–114 (2000).

213. Savarese, G. & Lund, L. H. Global Public Health Burden of Heart Failure. *Card. Fail. Rev.* **03,** 7 (2017).

**Publishing Agreement**

*It is the policy of the University to encourage the distribution of all theses, dissertations, and manuscripts. Copies of all UCSF theses, dissertations, and manuscripts will be routed to the library via the Graduate Division. The library will make all theses, dissertations, and manuscripts accessible to the public and will preserve these to the best of their abilities, in perpetuity.*

*Please sign the following statement:*

*I hereby grant permission to the Graduate Division of the University of California, San Francisco to release copies of my thesis, dissertation, or manuscript to the Campus Library to provide access and preservation, in whole or in part, in perpetuity.*

_____        12/7/18
Author Signature                                         Date

144